MECHANICS OF REMORA ADHESION

A Dissertation
Presented to
The Academic Faculty

by

Michael Beckert

In Partial Fulfillment
of the Requirements for the Degree
Doctor of Philosophy in the
School of Mechanical Engineering

Georgia Institute of Technology
August 2015

MECHANICS OF REMORA ADHESION

Approved by:

Dr. Naresh Thadhani, Advisor
School of Mechanical Engineering
Georgia Institute of Technology

Dr. David Hu
School of Mechanical Engineering
Georgia Institute of Technology

Dr. Jason Nadler
School of Material Science Engineering
Georgia Institute of Technology

Dr. Alexander Alexeev
School of Mechanical Engineering
Georgia Institute of Technology

Dr. Brooke Flammang
College of Science and Liberal Arts
New Jersey Institute of Technology

Date Approved: April 24, 2015

A modern day warrior
Mean, mean pride
Today's Tom Sawyer
Mean, mean pride

ACKNOWLEDGEMENTS

I would like to thank all those who helped me through the many trials during the preparation of this work.

To my parents Bruce and Elizabeth Beckert, and my sister Caroline, for reminding me of life's true importance

To my advisor Jason Nadler, for his guidance and support

To Brooke Flammang for her encouragement and advice

To my reading committee David Hu, Alex Alexeev, and Naresh Thadhani for their helpful suggestions

To Keri Ledford, for her assistance with live specimens and work in the clean room

To Ryan Bloomquist for his dissections

To Angela Lin, for providing numerous CT scans

To my wife Brooke, for her endless support both inside and outside the lab

TABLE OF CONTENTS

LIST OF TABLES

LIST OF FIGURES

SUMMARY

Remora fishes are capable of rapid, reversible, and robust attachment to a wide variety of marine hosts both natural and artificial with widely varying geometric and material properties. Despite its unique abilities, the mechanisms responsible for remora attachment have received little attention in scientific literature in comparison to the number of works commenting on it. The objective of this work is to identify and quantify the behavior and limitations of the critical mechanisms responsible for remora attachment. Traditional dissection techniques were combined with high-resolution three-dimensional scans to characterize and identify critical structural metrics pertaining to remora morphology. The structural metrics were incorporated into simulations to predict remora behavior during attachment. Finally, experimental methods were performed on artificial tissues to validate model predictions when necessary. The work is of value to both the engineering and biological communities through the creation of design tools, analyses, data sets, and simulations that provide both quantitative design data for bioinspired devices and/or methodologies, but also insight into the behavior of the remora itself.

CHAPTER 1

Introduction

The eight fish species that comprise the Echeneidae family are commonly referred to as remora, suckerfish, diskfish, or sucker-fish, and are known to inhabit tropical and subtropical waters worldwide, except for one species which lives in the western Atlantic Ocean [1]. Remoras are unique in that they possess a specialized dorsal fin or pad that is capable of rapid and reversible adhesion to a wide variety of both natural and artificial marine hosts as seen in Figure 1.1 [2].

Figure 1.1: Remora fish attached to various surfaces

Figure 1.2(a) shows the dorsal pad located on top of the remora's head, and several characteristic features including the (a) fleshy lip (soft tissue around the perimeter of the pad), (a,b) lamellar compartments (periodic, slit-like features along the pad length), and (b,c) the spinules (mineralized tissue protrusions from lamella). These features and others work in concert to maintain adhesion.

In spite of the uniqueness of remora attachment, it has not enjoyed the fame of other attachment systems including geckos, beetles, tree frogs, and abalone [3] to name a few. This is somewhat surprising given that the history of remora in biologically inspired design vastly predates the use of bioinspired nomenclature. Appearances of remora in scientific literature around the mid to late 1800s describe fish catching devices (which might be deemed bioinspired today) employing the remora itself as the device [4, 5]. Many accounts attest to anglers fastening cords to the caudal (tail) fin, and releasing remora into the sea where they were allowed to swim out and attach to a host. Once attached, the angler would reel in the remora and capture the attached host. These early accounts allude to the strength of remora attachment.

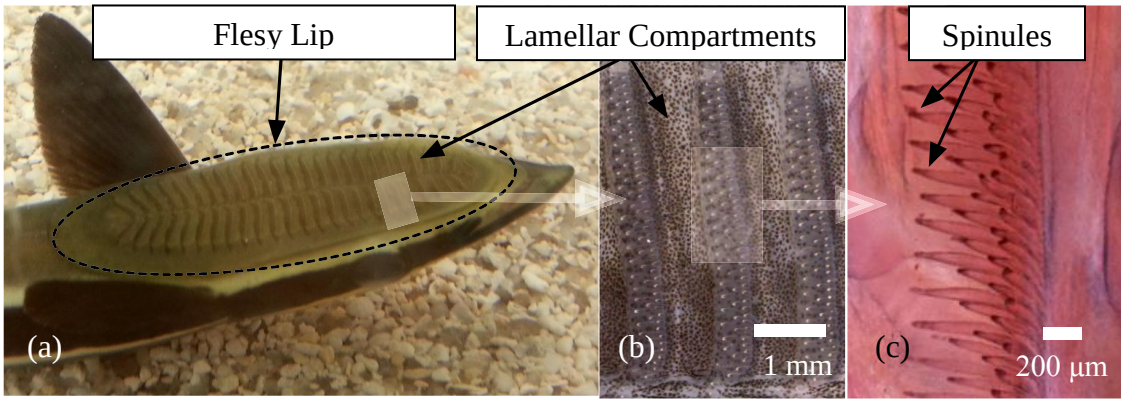

Figure 1.2: (a) Photograph of live remora suction pad (b,c). Photograph of detached "suction pad" with highlighted structural features of interest.

While some work (see Section 1.1.2) has been done in recent years to quantify the strength of remora attachment, very little has been done to characterize the physical mechanisms employed by the remora to create and maintain attachment. As a corollary, the limits and applicability of the remora suction pad are not known. It is the goal of this

work to identify and quantify the physical and structural mechanisms responsible for remora attachment.

1.1 Remora Background

Even though accounts of the remora date back to antiquity, the bulk of scientific knowledge was acquired after the 1950s. Before the 2000s, the remora most commonly appears in biological, observational research with the focus centered on aspects of diet, remora/host behavior, and common hosts. After the 2000s, more efforts are undertaken to apply engineering principles to the study of remora and quantify the strength of remora attachment. The most recent studies apply mechanical theories to remora attachment in an attempt to further understand and predict the limits to remora attachment.

Different species of remora exhibit varying degrees of hitchhiking behavior [6], as typically dictated by their diet. An extensive list of hosts for different species of remora is given in [6], and a somewhat narrower list is given in [7]. The range of marine hosts is quite broad both in terms of surface geometry and surface topology ranging from sharks [8, 9], various pelagic fish [10], rays [10], turtles [11], dolphins [12], buoys [7], ship hulls [7], manatee [10], and concrete blocks [13]. Such diverse list extols the broad applicability of the remora pad for attachment.

Different species of remora fish are known to have different feeding habits, which have been primarily ascertained by examination of the stomach contents obtained during dissection. Several studies [7, 10, 14, 15] indicate remoras are predators of zooplankton and nekton, commensal feeders on the food scraps or fecal/vomit matter of their host, and/or symbionts who consume parasites on the gills or body of the host. The progression from predator to symbiont represents increasing dependence on the host. Additionally,

Strasburg [14] postulated that the morphology of a particular species of remora may be strongly influenced by its role with relationship. One study found that remoras become satiated upon consuming approximately 16-17% their volume in food [13].

Fertl and Landry [2] list the suspected benefits to a remora during its association with a host as transportation, protection from predators, increased courtship/reproduction potential, enhanced gill ventilation and expanded feeding opportunities. As discussed earlier, in some cases there is some benefit to the host since certain species of remora consume parasites. However, many studies have noted that some fish are reluctant to serve as hosts for remora [8, 9, 13, 16] by both actively avoiding attachment attempts and attempting to remove an attached remora. In one particular case the remora had to be removed from the aquarium as the host was incurring injuries while attempting to remove it [17]. Such behavior indicates that most hosts do not benefit from remora attachment.

The effects of remora attachment on a host can vary significantly. For example, in sharks and dolphins, an attached remora is at worst an irritation [8, 9, 15, 16]. Occasionally, a remora may attempt to attach itself to an area that interferes with the habitual behavior of the host or near sensitive areas [15]. In such cases, the host may try to reposition the remora by shaking or "wiggling" its body. The consequences to scaly hosts are usually more severe. Typically, an attached remora will abrade and remove the protective scales from its host in the area of attachment thereby exposing the underlying tissues to the open environment [18]. Prolonged exposure to the open environment often results in the death of the host [19].

1.1.1 Morphology

The size of remoras varies among species but can range from a few centimeters [7] to nearly a meter [11, 16] weighing on the order of 0.1 to 1 kg [12]. Britz and Johnson [20] carried out a detailed ontogenic study with respect to the development of tissue structures in several remora species. A study by Nadler [21] focused more on the merits of remora structures with respect to attachment and found strong similarities in the geometry between different species and sizes of dorsal pads. The study by Nadler further found that remora spinule spacing is very similar to shark dermal denticle spacing, which may help explain why remoras attach more strongly to sharkskin than smoother surfaces.

1.1.2 Mechanics of Remora Attachment

Perhaps the first reported attempt to quantify the strength of remora attachment was performed by Sewell [22] where vertical pull-off forces of 150-160 N were measured. More modern attempts to directly quantify the mechanical attachment strength of a remora suction disks were performed by Fulcher and Motta [23]. The study compared remora attachment strength on different textured surfaces with respect to a posterior directed load. The study found increased attachment strength to sharkskin (17.4 N) as opposed to the much smoother Plexiglas surface (11.4 N).

Several studies have made observations of remora attached to spinner dolphins some of which attempt to calculate the force required to dislodge a remora. One study [15] notes the number of remora attached to a single dolphin can range from 1-3. Hester [24] suggested that the spinning behavior was made in an effort to dislodge remora, but rejected this hypothesis as spins were executed both with and without attached remora. A more rigorous mathematical model proposed by Fish et al. [25] describes the corkscrew

maneuvers executed by spinner dolphins. Fish suggested the motivation for spinning as that of remora removal since they act as "drag parasites." A simple mechanical analysis that followed [12] notes that although the dolphins theoretically spin fast enough to dislodge a remora, it is in fact usually the stunning impact of the dolphin with the water surface that causes detachment. This ability of the remora attachment to withstand these dynamic loads is further testament to the strength of attachment.

Other studies by Culler and Nadler present detailed finite element models of remora pad mechanics based on measured tissue properties and morphology. One details the limits of remora seal behavior with respect to host surface topology [26]. It found that due to the compliant nature of remora soft tissue, the remora lip provides an excellent seal up to the cavitation limits of water. Another study examines the forces acting on the pad vs. deformation of the lamellar structures that occurs during remora attachment [27]. It estimates the restorative force generated by the lamella and the ability of the pad to eliminate fluid volume.

1.2 Biological Adhesion

The following section is a survey of notable biological attachment examples, which illustrate some of the defining concepts in the way organisms bond to surfaces. Adhesion in the natural environment is challenging in part due to obstacles such as surface contamination (weak boundary layers, particulate) and surface irregularity (geometric, chemical). The means with which organisms overcome these challenges are classified into four categories by Barnes including interlocking (claws), friction (micro-interlocking and intermolecular forces), gluing, and bonding with the last category subdivided into wet adhesion, dry adhesion, and suction [28]. With respect to bonding,

several common themes are encountered including an extremely compliant tissue interface that results in intimate contact with the mating surfaces (van der Waals forces, sealing/suction), surface energy effects (wettability, capillary bridging), and viscous effects (sealing/suction).

Extreme compliance is often a result of hierarchical tissue structures that branch into finer and finer elements from the micro to nano scales [29]. This intimate contact allows van der Waals forces to become significant, but also encourages a very tight seal between mating surfaces and may increase friction [30, 31]. Surface energy is also strongly affected by a hierarchical microstructure such is the case in super hydrophobic and hydrophilic surfaces [3]. However, in many organisms secreted mucus alters the surface tension properties of its surrounding medium (usually water) and therefore the ability to form capillary bridges [32, 33]. Furthermore, mucus can also alter the viscosity of water, which has important consequences in sealing/suction applications [34]. Often many of these effects occur simultaneously as is demonstrated by some of the following examples.

Perhaps the most famous biological attachment mechanism is found in the gecko. Gecko adhesion is considered to be a combination of dry adhesion, making use of primarily van der Waals forces [29], but also wet adhesion where humidity and surface conditions also play a role [30]. The gecko pad is composed of a hierarchical structure whereby microscale setae branch into nanoscale spatulae. This structure enables a large real area of contact between the gecko and mating surface [32], which results in relatively large adhesive forces.

In a regime similar to the gecko, tree frog toe pad morphology is a structural hierarchy composed of columnar epithelial cells which group into hexagonal features, creating channels for mucus flow [35]. The hierarchical structure creates an extremely compliant material (Young's Modulus order of 1-10 kPa) allowing the tree frog to make intimate contact with the mating surface [28, 36].

The abalone is an example of a marine animal that exhibits a hierarchical attachment structure. The interface between the abalone and mating surface is maintained by nanofibrils that are approximately 200 nm in diameter which creates a highly conformal contact surface similar to the gecko and tree frog [31]. In contrast to geckos and tree frogs, the highly conformal surface creates a suction seal against rough surfaces rather than liquid capillary bridges [31]. Thus, as external forces act to remove the abalone from the attachment surfaces, suction forces maintain attachment up to the theoretical limits of water (cavitation).

Several species of fish create suction based attachment using modified fin structures. Clingfish (family Gobiesocidae) have modified pelvic fins that possess a hierarchical adhesive surface made from groups of papillae that terminate as fine filaments [37]. The clingfish has been found capable of adhering to surfaces with an average roughness of 269 μm [37], which underscores the utility of surface conformance offered by the microstructure. Lumpsuckers (family Cyclopteridae) also have a modified pelvic adhesive pad [38]. One study has measured the large vertical pressures (~100 kPa) that can be sustained by lumpsuckers and attributed this ability to the mucus it secretes [39], though such large pressures are not likely to be routinely encountered in their natural environment [40]. River loaches (family Balitoridae) have modified ventral fins,

which they use to attach to surfaces in swift moving currents. River loaches are known for using almost their entire body to create suction based adhesion [41].

Octopi are another well-known example of marine adhesion. These animals primarily rely on suction-cup like features, which induce negative pressures through muscle contractions. Octopi have small denticles on their sealing surfaces [42], potentially suggesting a hierarchical structure. Like other cephalopods the mucus secreted by the octopus may enhance attachment strength [33, 42]. Another important factor in cephalopod adhesion, especially at substantial depths, is how the wettability of attachment surfaces affects the cavitation pressure of sea water [43].

In a slight departure from the previous examples, another way marine organisms create attachment is by forming a protein based plaque adhesive (gluing), sometimes called a holdfast, between themselves and the attachment site. Three common and well documented examples are barnacles [44, 45], mussels [45-47] and sea stars [48]. Practically, marine plaque formation is of primary interest because water is typically considered a contaminant in adhesive technology often termed a "weak boundary layer" that chemically attacks or disrupts adhesive layers [47]. The research on these organisms highlights the importance of surface conditions (stiffness, energy, etc.) on attachment. Observations include barnacles altering the chemical composition of their adhesive depending on the condition of the attachment surface [44], and mussels actively seeking higher roughness/energy surfaces when placing their byssal threads. In contrast to barnacles and mussels, sea stars use secretions to form temporary attachment to a surface. Sea stars utilize a duo-glandular system whereby an adhesive material is secreted to form attachment and a release agent is secreted to break attachment [48].

This short list of examples is summarized in Table 1.1, and highlights the importance of tissue stiffness, surface energy, and viscous effects in biological attachment. Though, for all their similarities, each organism ultimately posses a unique attachment strategy based on a long evolutionary history.

Table 1.1: Selected Examples of Biological Adhesion

Organism	Mechanism	Reversible	References
Gecko	Van der Walls Capillary Bridging	Yes	[29, 30, 32, 49, 50]
Tree Frog	Capillary Bridging	Yes	[28, 35, 36]
Abalone	Suction	Yes	[31]
Clingfish	Suction	Yes	[37, 51, 52]
Lumpsucker	Suction	Yes	[38-40]
River Loaches	Suction	Yes	[41]
Octopus	Suction	Yes	[33, 42, 43, 53, 54]
Barnacles	Glue	No	[44, 45]
Mussels	Glue	No	[45-47]
Sea Stars	Glue & Release Agent	Yes	[48]

1.3 Thesis Description

The following sections present an overview of the objectives and approach that will be employed to understand remora attachment. The approach has been adapted from other biomechanics research efforts as described in Section 1.3.3. Before proceeding into the objectives of the work, it is necessary to outline the remora attachment process to provide scope.

1.3.1 Qualitative Description of Remora Attachment

Historically there was debate as to whether remora attachment was suction based. Some believed the dorsal pad was “not a true sucker, but essentially an elaborate device for producing the maximum amount of friction” on a surface by taking advantage of swift

currents that press the fish against its host [55].” Although this was soon proven to be incorrect by attachment experiments on perforated sheets and wire meshes [22], both drag forces and friction play important roles in remora attachment as will be shown in later chapters.

The remora’s suction pad can be viewed as a combination of structural features that contribute to overall attachment. Currently identified pad features include spinules, fleshy lip, lamellar compartments, and mucus; each of which plays an important role in the attachment sequence. The proposed sequence of attachment, seen in Figure 1.3, is based on handling and observation of live remora specimens when viewed in the context of the body of knowledge discussed above.

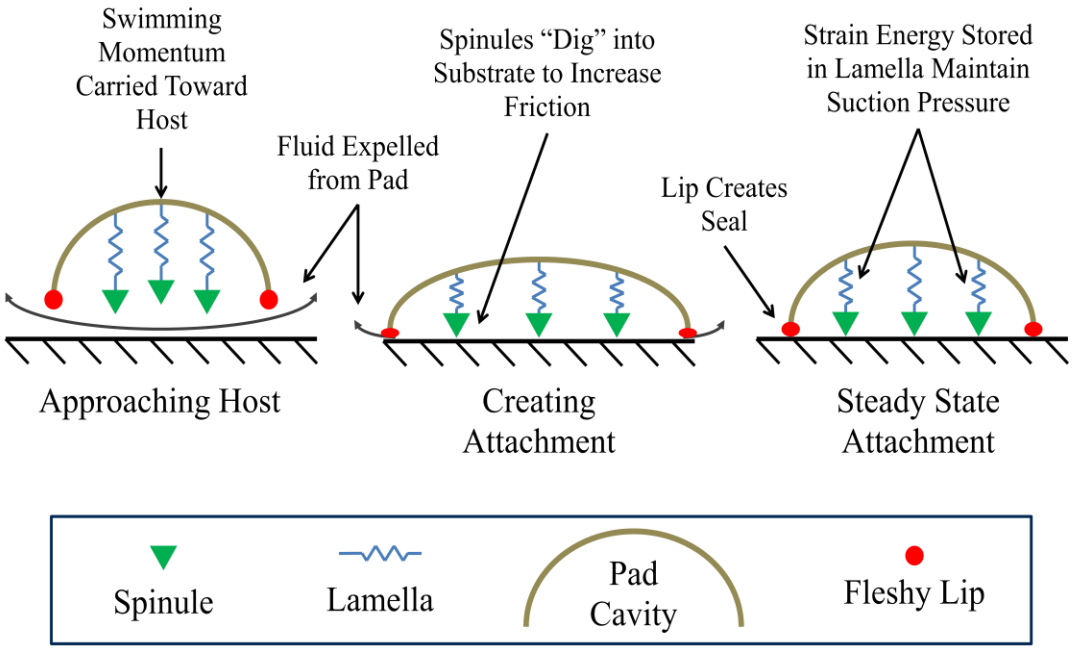

Figure 1.3: Proposed remora attachment sequence

Attachment begins as the remora approaches its host. It uses its momentum to force fluid out of the pad’s cavity by compressing the lamella and lip. The lip acts as a

“fluid diode” or “check valve” only allowing flow out of the suction pad (though in later chapters it will be shown that the lip does in fact leak). Suction pressure is maintained as the lamella attempt to restore their original shape, and by the tight seal made by the fleshy lip. Throughout the entire process, the body and pad of the remora are coated with a layer of mucus, which increases the viscosity of the surrounding fluid. This serves to increase attachment strength and/or provide lubrication for the remora to reposition itself on the host without fully detaching.

Later chapters will show the body shape of a remora can be reasonably approximated as a streamlined, non-lifting body, which contradicts the early notion that adhesion is primarily created by hydrodynamic forces pressing the remora into the host. However, the hydrodynamic drag remains an important consideration in attachment because it must be resisted or else the remora is sheared off its host. To prevent this kind of failure, remoras create high frictional forces using small posterior directed spinules on the dorsal pad. Later chapters will show that spinules act as micro-sized claws that interlock with rough surfaces to create resistance to slippage.

Similar to other accounts of remora attachment, this description is purely qualitative; however, it does frame the remora attachment sequence into discrete intervals and mechanisms that can be studied quantitatively.

1.3.2 Objective

The objective of the current work is to investigate the coordination between remora behavior and the structures in the suction disk that facilitate strong, adaptive attachment to a variety of marine hosts. The primary research question is: How do the functional structures of the remora suction disk work in concert with active remora

behavior to achieve strong, reversible attachment to a variety of host substrates, and what are the limits of remora attachment? Even though an attachment sequence was proposed in section 1.3.1, the effort throughout the rest of the work is focused toward developing quantitative models to describe remora attachment.

1.3.3 Approach

Throughout the current work the "rational" approach to biomechanics is employed, as seen in Figure 1.4, to identify relevant analysis methods required to describe remora attachment [56]. The primary strength of this method is that by starting from basic principles and taking a reductionist approach, incorrect and/or unnecessary hypothesis can be avoided early in the process. The following sections describe the steps in Figure 1.4 in greater detail.

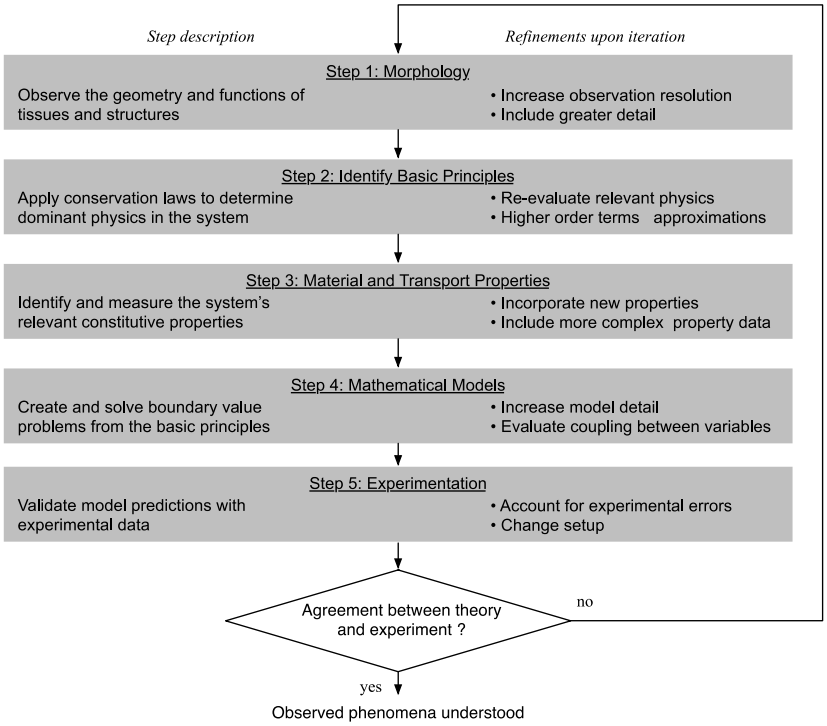

Figure 1.4: Rational approach to biomechanics

1.3.3.1 Morphology

The first step is to observe the morphology of the specimen. This is an important data gathering step that involves both identifying the structures that are important to understanding the biological function of interest, and quantitatively describing the structures such that further analysis can be performed. There are many ways to observe specimen geometry. Different techniques can vary in complexity and richness from manual dissection and measurement to spatially resolved tissue maps gathered from micro-computed tomography (μCT) scans, for example. The goal of this step from Figure 1.4 is to obtain an accurate representation of remora pad geometry and develop suitable simplifications and/or structural descriptors that can be used in engineering analysis to assess its behavior and/or performance.

The traditional means for assessing the anatomy of a specimen has been dissection. Detailed dissections of remora are available [6, 20]; however, these studies have limited predictive value, as the results are largely qualitative descriptions.

A much richer geometric dataset can be obtained from μCT, which is a nondestructive test that results in a series of tomographic, grayscale images where each pixel value is related to the local density of the material. In the case of biological specimens, when μCT is combined with image segmentation analysis, the boundaries between mineralized and soft tissue can be obtained due to large density differences between mineralized and soft tissue. A resulting three-dimensional model of a remora pad can be seen in Figure 1.5 showing soft (a) and mineralized (b) tissue boundaries.

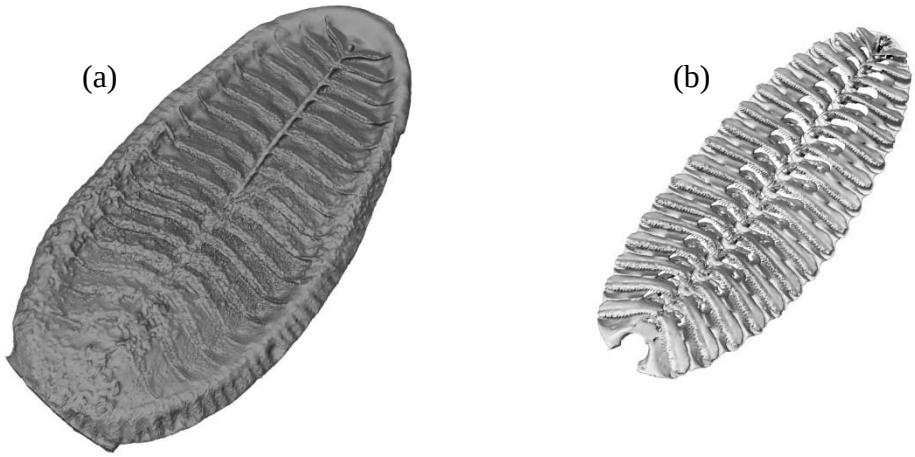

Figure 1.5: Example μCT scans of remora pad showing soft (a) and mineralized (b) tissue boundaries

There are several benefits of μCT imaging compared to traditional dissection. First, the scan is nondestructive so there is little risk of damaging tissue structures by sectioning. Also, μCT results in a digital representation of a structure that is portable and sharable. Such a data set is useful in many contexts as it provides an accurate and objective representation of the specimen. Moreover, the digital nature of the data lends itself to statistical characterization of features that can be quickly identified and quantified by computer algorithms. In some cases when a particular feature appears in great numbers, such as spinules in the case of the remora, it is not feasible to perform manual analysis. Measurement accuracy between features is also improved in the digital environment since the locations of material points are accurately known. In some cases, the scanned geometry can be imported directly into finite element models; however, in practice this can only be accomplished when the complexity of natural structure does not cause an unreasonably high computational burden.

Despite the benefits of μCT, there are still some advantages to performing manual dissection. An important use of dissection is to provide a basis of comparison and

validation of a successful μCT scan. As mentioned previously μCT requires differences in density to determine the boundaries between tissues, and while this is readily accomplished with mineralized and soft tissues, μCT is much less accurate at segregating soft tissues when the densities are similar. Similarly, certain features of soft tissue such as muscle fiber direction and attachment points are much more easily found with manual dissection.

In this work, μCT data is the primary morphological data source of remora and remora pad geometry. Due to the complex nature of the pad geometry, simplifying structural representations and descriptors will be created to facilitate efficient analysis of the structure. Comparisons of μCT data with dissections from the literature are made when possible as a means of validation.

1.3.3.2 Identifying Basic Principles and Material/Transport Properties

The next two steps (Identifying Basic Principles and Material/Transport Properties) in Figure 1.4 are highly interconnected. Once the domain's geometry is captured, the dominant physics responsible for the observed behavior should be identified. It is good to begin with basic conservation laws such as those for mass, energy, and momentum, and then use techniques such as scale analysis to identify the primary driving forces in the system, be they mechanical, chemical, and/or thermal. However, the magnitude of the driving force usually requires some knowledge of the material and transport properties of the system. If no data exists and no estimates can be made, then one must move forward by experimentally gathering data for all relevant phenomena until the dominant physics of the domain are identified.

With respect to the remora, the goal of this step is to characterize the material/transport properties of the suction disk tissues and other relevant materials. The pad itself is a composite of mineralized and soft tissues, which is externally coated in a thin layer of water-soluble mucus. There are several different approaches that can be taken to understand the behavior of these complex materials.

As noted by Fung [57], the basic building blocks of tissue include a limited number of substances such as abductin, actin, resilin, elastin, collagen, keratin, and ground substance, to name a few. One could theoretically proceed in a bottom up fashion by identifying the microstructure of the tissue and applying the mechanical properties of the basic materials to obtain the macroscopic mechanical properties of a tissue. Such an approach is useful in the proper context. However, since the derived properties would ultimately need to be compared to measured macroscopic tissue properties, and because quantifying the fundamental nature and composition of remora tissue is not a goal of the current work, it is sufficient to proceed by directly characterizing the behavior of the materials.

1.3.3.2.1 Soft Tissue

With respect to soft tissue, many authors note its viscoelastic nature and generally focus on linear viscoelastic theories [57-59]. In linear viscoelasticity, the relationship between stress, σ, and strain, ε, can be expressed with the Boltzmann Superposition Integral seen in Equation 1.1, where E is the relaxation modulus.

$$\sigma(t) = \int_0^t E(t-\tau)\frac{d\varepsilon(\tau)}{d\tau}d\tau \qquad 1.1$$

The most notable difference between linear viscoelasticity and linear elasticity is the time dependence of the modulus relating stress to strain, and, in fact, when the relaxation

modulus is independent of time one recovers Hooke's Law. Thermodynamics provides the limits on the relaxation modulus, namely that it must decrease monotonically with time (to satisfy the dissipation inequality) and have a positive initial value (solution uniqueness) [60]. Such constraints admit an infinite number of potential relaxation modulus functions; however, most commonly take the form of rheological models consisting of springs and dashpots such as Maxwell, Kelvin, Voigt, and Wiechert models.

Equation 1.1 is used throughout this work to describe the behavior of remora soft tissue. As a basis for comparison, a rough order-of-magnitude estimate of the relaxation modulus in soft tissue can be found by comparing the results from other studies in soft tissue. Looking at the results of tissue analysis from the human breast and prostate [61], rabbit arteries [62], human livers [63], bovine livers [64], and canine livers [65] it is expected that the relaxation modulus of the soft tissue to be on the order of 1-100 kPa. The extreme compliance of these soft tissues is made even more apparent when compared to soft engineering materials such as natural rubber (E >1000 kPa [66]).

1.3.3.2.2 Mineralized Tissue

Unlike soft tissue, linear elasticity can be used to accurately describe the behavior of mineralized tissue; though in general it must be treated as anisotropic [57]. Several authors have examined the mineralized tissue properties from teleost fish (a class to which remora belong) [67-69], and found similar material properties across many different teleost species. Hence, modeling the bone as incompressible with typical values of the elastic modulus on the order of 6 GPa yields reasonable accuracy.

1.3.3.2.3 Mucus

An important and previously neglected feature of remora attachment in the literature is mucus. Fish mucus or "slime" is composed largely of water and high-molecular-weight, gel-forming macromolecules, which in fish are generally glycoproteins (mucins) [34]. Similar to other pelagic fish, remoras excrete mucus from goblet cells located throughout their body. However, with respect to the epidermis (skin), remoras differ from other fish in that during attachment the pad is isolated from the surrounding environment, which prevents diffusive and convective losses of mucus. In theory, isolation of the pad makes it possible for remoras to generate relatively high mucus concentrations compared to other free-swimming fish. As has been observed, the concentration of mucins can have an effect on the viscosity of the solvent (water) ranging from negligible [70] to significant [71]. Thus, at the very least, remoras may be able to increase the viscosity of fluid within the pad. Additionally, it may be possible that the mucus excreted in the pad at sufficiently high concentrations could act as weak "glue" between the remora and host; however, this is not examined here.

1.3.3.3 Mathematical Models

With the basic principles and system properties identified, the next step from Figure 1.4 is the creation of mathematical models to describe and make predictions about the observed behavior. A model should be designed such that its results can be subjected to experimental validation in the final step. If mathematical predictions match experimental results, then the goal of understanding the observed behavior is achieved. Conversely, if there is disagreement, one must revisit earlier steps in the process to

identify the source of disparity. Through the iterative process, knowledge is gained by refining data and discovering things that may have been overlooked at first glance.

Suffice it to say that many mathematical models are developed throughout this work, and it is not necessary to describe them here as they are sufficiently enumerated in the respective chapters. However, broadly speaking, many problems fall into the realms of structural and fluid mechanics, with some exceptions. Here it is enough to say that although predicting remora behavior is the primary focus of the work, almost all the mathematical approaches used can, in a general sense, be applied to other biomechanical or bioinspired systems. Thus, the tools developed herein are expected to have broader impacts on the biology and engineering communities by helping to refine goals for investigations and increase fidelity of observational and behavioral evolutionary studies.

1.3.3.4 Experimentation

The final step in Figure 1.4 is experimentation. Similar to the previous section, it is not necessary to go into detail about experimental methods since they are adequately addressed in later chapters. In general, the experimental work carried out is focused on validating the physics of an individual model using artificial tissue analogs. Then validated approaches are used to analyze a similar aspect of remora physiology with measured biological parameters. The benefits of this approach are twofold: difficulties often cited when working with live or euthanized tissues can be avoided (dependence on hydration levels, time since death, live specimen movements, etc.), but more importantly, validation with an artificial apparatus provides a direct link to an engineered application. Additionally, model predictions are validated by comparison with experimental observations from biological or engineering literature when available.

1.3.4 Thesis Outline

Each chapter can be read independently of the others. Although this creates some overlap in the methods or descriptions of the remora, these are usually minimal and typically confined to the introductions. Such organization facilitates ease of reading, as the work can be digested in parts without the need to reference other chapters frequently. In the following chapters, different aspects of remora adhesion are considered, and each provides some insight into the primary research question. The following paragraphs are a brief summary of what to expect from each chapter.

In CHAPTER 2, the fluid drag on an attached remora is quantified. Fluid drag is the primary force a remora must overcome, and despite the remora's history in scientific literature, CHAPTER 2 is the first rigorous treatment of its hydrodynamics.

CHAPTER 3 is a quantitative exploration of the mineralized tissue structures within the dorsal pad where select pad features are measured in remora specimens. Considering the repetitive nature of features in the remora pad, like the rows of pectinated lamellae, developing algorithms that identify and quantify salient structural features is useful when formulating valid simplifying assumptions in later chapters.

CHAPTER 4 is an investigation of spinules and their ability to enhance friction on rough surfaces. Based on the structural analysis carried out in the previous chapter, a three-dimensional model of spinule friction is developed. Understanding how remoras create friction against their host is essential, as it is the primary force employed to overcome fluid drag.

CHAPTER 5 treats the remora lamellar compartments. A two-dimensional structural mechanics model based on lamellar geometry and measured remora tissue

properties is used to show how lamella deform with respect to changes in loading at the spinule tip. It is important to understand how the lamellae interact with a host surface because they make up the bulk of the suction pad.

In CHAPTER 6, a model of the leakage rate across the fleshly lip and its interfacial permeability with respect to sub-ambient pressures within the dorsal pad is presented. The model is based on measured host topology, remora soft tissue properties, and the rheological properties of fluids within the pad. It is important to understand how the fleshy lip performs under the influence of suction pressures because it creates the primary seal against the host.

Finally, CHAPTER 7 brings the results of all the previous chapters together to assess the attachment performance of the remora's dorsal pad. A failure analysis of the pad is carried out which assumes that gradual failure of the pad occurs due to fluid leakage across the fleshy lip. As the pad fills with fluid, suction pressures are reduced until friction is no longer sufficient to resist drag forces and the remora is sheared from its host. The final chapter illustrates how all the structural features within the remora pad work together to achieve attachment, and provides some theoretical limits to attachment time.

1.4 Conclusion

The remora fishes are a fascinating example of a biological attachment system, but quantifying the mechanisms responsible for creation of the remora's rapid, reversible, and robust attachment have received little attention in scientific literature despite numerous studies commenting on the behavior. Several key features of the remora pad have been identified as playing critical roles in the attachment process and it is the goal of

this work to understand their behavior and provide quantitative limitations. The insights shared can be considered in their original context, and then explored by future designers in terms of their own environments. The tools and analyses provided herein serve to explain remora behavior, and can be generalized to suggest design metrics for the creation of bioinspired devices.

CHAPTER 2

Fluid Drag on Attached Remora

2.1 Introduction

Remora fishes in the Echeneidae family have adapted a unique dorsal suction pad that allows them to attach to various host organisms and marine vessels, which includes but is not limited to sharks, whales, rays, other pelagic fish, sea turtles, dolphins, divers, buoys, ship hulls, and concrete [6-13, 72]. Proposed benefits to the remora include transportation, protection from predators, increased courtship/reproduction potential, enhanced gill ventilation and expanded feeding opportunities [2]. With respect to the benefits of the host organism, certain remora species have been known to feed on parasites attached to the host [7, 14]; however, there are many documented cases of hosts that are either unwilling to serve [13, 17] or attempt to remove the remora by various means [8, 9, 12, 25]. Despite work that has been done to better understand the attachment strength [23] and physical mechanisms associated with remora attachment [21, 26, 27],very little has been done to quantify the primary force that remoras must overcome in order to maintain attachment, namely fluid drag. While some basic estimates of fluid drag on the remora have been made in relation to remora attachment to spinner dolphins [25], a detailed drag analysis has yet to be performed. The aim of this chapter is to provide a more rigorous estimate of the fluid drag force on the remora in the context of its association with a host. The estimates are based on computerized fluid dynamics

simulations informed by real three-dimensional remora geometry obtained from micro-computed tomography (μCT).

Traditionally, theoretical and experimental drag forces on fish and other marine organisms were associated with rigid physical models [73-77]. For certain simple swimming gaits such a gliding between bouts of active swimming, this technique can deliver reasonable results [77, 78]; however, for more complex swimming gaits the body motions of the host (swimming kinematics) must be included to deliver accurate drag estimations [77, 79, 80]. With respect to the remora, it has been observed that there is a high degree of attachment site fidelity [13], and although it has been noted that remoras may reposition themselves on the host [8, 15], they cease undulatory motion once attachment is created [22]. Therefore, because the remora naturally glides through the water under the power of its host, treating the remora as a rigid body should provide a reasonable estimate of the drag associated with attachment.

In addition to the drag on the remora's body, it may also be important to incorporate the hydrodynamics of the host organism, as this may help explain some aspects of remora/host interaction. For example, a study by Silva-Jr. and Sazima [15] observed the frequency with which remora (*Remora australis*) attached to various locations on spinner dolphins (*Stenella longirostris*). The authors suggested that remoras preferentially attach to certain sites to either minimize interference with the dolphin's habitual behavior or for hydrodynamic reasons [15]. While the first conclusion is almost self-evident, the latter suggests that the remora is taking advantage of reduced drag associated with the host's fluid boundary layer. When a submerged body is subjected to fluid flow, a boundary layer naturally forms owing to the "no-slip" condition on the

surface of the body (fluid in contact with the body remains stationary with respect to the body) [81]. Typically, as one progresses along the length of the body, the boundary layer thickness increases [81]. As the thickness of the boundary layer grows, an attached remora experiences less of the free stream fluid velocity and lower drag forces. Thus, some attachment sites may be preferential to the remora because they offer lower drag forces. Here, this concept is tested by subjecting the remora to different boundary layer thicknesses and free stream velocities (host swimming speeds) to assess whether there is substantial drag reduction.

Once the drag on the remora is estimated, it is possible to investigate other aspects of remora and host interaction such as the power that must be supplied by the host to overcome the remora's drag (parasitic drag power), and whether or not a remora is likely to be removed by elevated host swimming speeds. The remora uses thousands of spinules, small mineralized tissue projections on its dorsal pad lamellae, to enhance friction forces between itself and its host [21, 23, 55]. To assess the potential for removing a remora by host swimming, the drag force must be compared to the frictional force created by the spinules. Later chapters investigating interactions between remora and shark skin will show the geometry of remora spinules results in approximately a 13 times increase (order of magnitude) in the friction coefficient. In the work by Fulcher and Motta [23], the attachment strength of two remora species (*Echeneis naucrates* and *Echeneis neucratoides*) was investigated by inducing remora adhesion to shark skin, and simultaneously measuring the suction pressure in the remora pad and the posterior directed load required for detachment. Using their results as a benchmark, if the

estimated drag force experienced by the remora is greater than the attachment strength due to frictional and suction adhesive forces, the remora will slip off its host.

2.2 Methods and Materials

2.2.1 Specimen Preparation and µCT Scanning

The remora (*Echeneis naucrates*) specimen was cared for and euthanized in accordance with the guidelines and principles of the Georgia Institute of Technology Institutional Animal Care and Use Committee, protocol A11085. The specimen was euthanized by a 0.5 g/L dose of MS-222 (tricaine methanesulphonate). After euthanizing, the specimen was fixed for µCT scanning in a phosphate buffer solution of 10 volume percent formalin for a minimum of 24 hours. After fixing, the specimen was washed twice and stored in 1X phosphate buffer. The specimen was scanned in air using a µCT50 (Scanco Medical, Bruttisellen, Switzerland) with voxel resolution of 200 µm. Tomograms were converted to dicom format, segmented, and surface rendered in OsiriX (v5.5, Geneva, Switzerland) [82].

The resulting three-dimensional surface model was imported into Rhinoceros 3D (Seattle, WA, USA). There the pectoral fins of the remora were manually removed, as during attachment the remora can choose to reduce its drag profile by flattening them against its body. Also, the caudal fin of the remora was reconstructed based on photographs and physical measurements due to size constraints of the µCT scanning chamber.

2.2.2 Feature Scaling

With the aid of a virtual three-dimensional remora model, feature scaling was investigated. Relationships were sought mainly to convert overall fish length to other relevant hydrodynamic features such as the wetted surface area, pad area, and largest transverse diameter. This was useful because it allowed for comparisons between derived quantities solely on the basis of length. Here it was assumed that isometric scaling applied to remora features. Thus, by prescribing different virtual scale factors to the remora model, scaling relationships were inferred between different features. As such, the allometric equation given by 2.1 was used to determine the scaling relationships between different model features, where X (the overall length of the fish here) and Y are the dimensions of the features, and a and b are fitting constants [39].

$$Y = aX^{b} \tag{2.1}$$

All geometric measurements were obtained in Rhinoceros 3D from the three-dimensional model created from μCT scans. Area and volume quantities were acquired from integration of the surfaces, whereas length measurements were obtained either from bounding box and/or projected edge lengths. The wetted surface area was calculated as the total body surface area minus the pad area.

2.2.3 Drag Estimation

Simulation of fluid flow over the remora geometry was accomplished with COMSOL Multiphysics (Version 4.3a Stockholm, Sweden). Under the assumption that remoras are relatively stationary with respect to their hosts and due to the high swimming efficiency of fish [83], the simulated flow was taken as steady, laminar, and

incompressible with standard no-slip boundary conditions on the surface of the remora model. Because many species of remora are known to attach to various shark species [6, 7], the remora model was subjected to free stream fluid velocities typical of sharks. Tagging studies on different shark species provided estimates of average swimming speeds on the order of 0.1 - 1 m/s [84-87], whereas maximum shark speeds may range between 1 and 10 m/s [84, 88, 89]. Therefore, the remora model was exposed to free stream velocities ranging between 5 mm/s and 5 m/s to include both the average and near top speed of many remora hosts.

After solving for the flow conditions around the remora, the drag force, $\vec{F}_D$, was calculated by integrating the pressure, p, and shear, τ, forces acting on the surface of the model in the direction of the flow, $\hat{i}$, using Equation 2.2 where $\hat{n}$ and $\hat{s}$ are the surface unit normal vector and unit tangent vector in the direction of flow [90].

$$\vec{F}_D = -\iint (p\hat{n}) \cdot \hat{i}\, dA + \iint (\tau\hat{s}) \cdot \hat{i}\, dA \qquad 2.2$$

The drag coefficient, C_D, was then calculated using Equation 2.3, where ρ, U, and A are the fluid density, free stream fluid velocity (host swimming speed), and the wetted surface area of the remora.

$$C_D = \frac{\vec{F}_D}{1/2 \rho U^2 A} \qquad 2.3$$

As a means of validation, other studies have used drag coefficients based on non-lifting, streamlined bodies to estimate the drag force on fish and other marine organisms [73, 75-77]. Owing to such an approximation, the drag force on streamlined bodies is mainly due to viscous (skin friction) effects, and less on flow separation and pressure drag, especially when the body is much longer than it is wide [83, 90]. Here, simulation results were compared to the drag coefficient of a streamlined body given by Equations

2.4 and 2.5 where Re_L, d, and L are the Reynolds Number with respect to body length, largest transverse body diameter, and body length, respectively [83, 90]. These relationships were determined from statistical analysis of many experimental studies on streamlined bodies and are useful as long as the body diameter to length ratio is below 0.5 [83, 90].

$$C_D = \frac{1.328}{\sqrt{Re_L}}\left(1+\left(\frac{d}{L}\right)^{2/3}\right)+0.11\left(\frac{d}{L}\right)^2,\ Re_L < 10^5 \tag{2.4}$$

$$C_D = \frac{0.0303}{Re_L^{1/7}}\left(1+1.5\left(\frac{d}{L}\right)^{3/2}+7\left(\frac{d}{L}\right)^3\right),\ Re_L > 10^5 \tag{2.5}$$

Equations 2.4 and 2.5 were created by the addition of both the frictional and pressure components of drag, which depend on the ratio of the body diameter to length. Because isometric scaling of the remora was assumed, the ratio of body diameter to length was fixed. Therefore, Equation 2.6, which is similar in form to Equations 2.4 and 2.5, was fit in a least squares sense to the simulation results, and was used as a relationship between the drag coefficient and the Reynolds number, where c_1, c_2, and c_3, are fitting constants.

$$C_D = \frac{c_1}{Re_L^{c_2}} + c_3 \tag{2.6}$$

In addition to the drag coefficient, the effect of the host boundary layer was investigated by placing the remora model on a virtual flat plate. By increasing the distance of the remora from the leading edge of the plate, it was possible to estimate the drag force experienced by the remora when subjected to increasing boundary layer thicknesses at different host swimming speeds; similar to moving the remora to more posterior attachment sites on a host. Although this procedure does not include pressure drag effects associated with host shape, it is a reasonable approximation when

considering the host itself is likely to be a streamlined body whereby most of the drag is associated with viscous effects [83, 90]. Equations 2.7 and 2.8 provided the boundary layer velocity profile for flow over a flat plate, where x and y are the horizontal and vertical distances from the start of the plate and μ is the fluid viscosity [91, 92].

$$u(x,y) = U\left(2\eta - 2\eta^3 + \eta^4\right), \quad \eta = {}^{y}\!/_{\delta} \tag{2.7}$$

$$\delta = 5.83\sqrt{\frac{\mu x}{\rho U}} = \frac{5.83x}{\sqrt{Re_x}} \tag{2.8}$$

The distance from the edge of the plate was varied between 10 cm and 10 m to be comparable to some of the larger hosts to which remora attach, such as the whale shark. In theory, as the remora is moved farther from the edge of the plate and the boundary layer grows, the remora should be further engulfed by the plate's boundary layer and exposed to lower velocities near the plate's surface. Therefore, posterior attachment sites may benefit the remora in terms of reduced drag.

Although remora are not considered parasites in the sense that they feed off of their host, they are certainly parasites in the sense that extra swimming effort must be supplied by the host to compensate for the hitchhiking remora [1, 15]. To estimate the increased rate of energy expenditure by the host, the parasitic drag power was computed as the product of the drag force and the host swimming speed (equivalent to the free stream velocity with respect to the remora). The parasitic drag power is given in terms of the drag coefficient in Equation 2.9

$$P_D = \bar{F}_D U = {}^{1}\!/_{2} C_D \rho U^3 A \tag{2.9}$$

2.2.4 Pull-Off Strength vs. Drag Force

An estimate of frictional forces developed between a remora and its host came from the results in [23] where it was found that on average a suction pad with an area,

A_{pad}, of approximately 16.95 cm^2 generated a maximum sub-ambient pressure, P_{max}, of 46.6 kPa for a posterior directed pull-off force of 17.4 N on shark skin. In the framework of static friction, these results suggest a coefficient of friction, μ_s, of approximately 0.22. Assuming the coefficient of friction and sub-ambient pressure remains constant with respect to the size of the remora, the drag force experienced by the remora was compared to the pull-off force vs. remora length and swimming speeds by combining Equations 2.1, 2.3, and 2.6 into Equation 2.10 where N is the ratio of the drag force to the friction force, $\vec{F}_F$. Thus, if N is greater than one, then the drag force is greater than the frictional force and the remora will be removed, otherwise the remora will remain attached.

$$N = \frac{\vec{F}_D}{\vec{F}_F} = \frac{\frac{1}{2} C_D \rho U^2 A}{\mu_s P_{max} A_{pad}} \tag{2.10}$$

2.3 Results

2.3.1 Remora Model and Feature Scaling

The three-dimensional remora model used for drag and feature analysis is shown in Figure 2.1 along with photographs displaying similar views of the actual specimen. Because the three-dimensional model was constructed from μCT scans, it is not surprising that the photographs and renderings bear a strong resemblance. However, there are notable exceptions, as discussed earlier, including the lack of pectoral fins and the reconstructed caudal fin.

By applying virtual, isometric scale factors to the remora model, the fitting constants needed for the allometric feature scaling equation (Equation 2.1) were computed and are shown in Table 2.1. As expected, when converting from length to length, surface area, or volume, the fitting exponent, b, was always one, two, or three,

respectively, because of the type of scaling imposed. The results in Table 2.1 are useful for expressing derived quantities from the flow simulation solely in terms of the fish length. For example, the drag coefficient or parasitic power can be expressed in terms of fish length rather than wetted area. The length of the remora model as scanned was 284 mm, which is in agreement with the measured value.

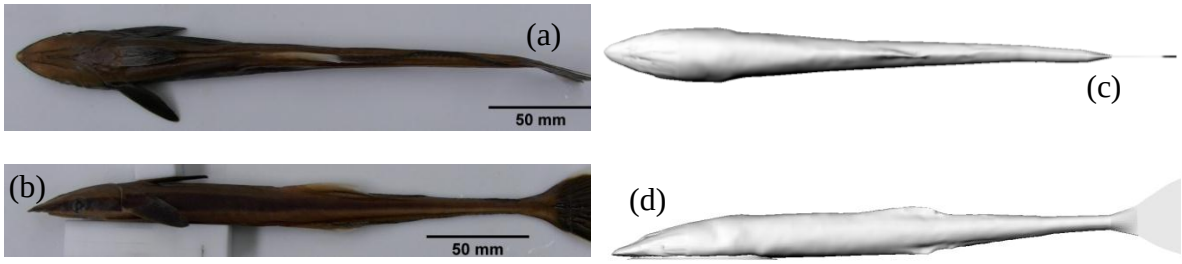

Figure 2.1: Photographs of remora specimen (a,b) and accompanying three-dimensional model based on μCT scan after digital fin removal and reconstruction (c,d). Corresponding top views are shown in (a,c) and side views in (b,d).

Table 2.1: Feature Scaling Fitting Constants (Equation 2.1)

Related Features		Fitting Parameters	
X	*Y*	*A*	*b*
Length (m)	Pad Area (m^2)	0.0141	2
	Wetted Surface Area (m^2)	0.166	2
	Volume (m^3)	2.23	3
	Largest Transverse Diameter (m)	0.0952	1
	Pad Perimeter (m)	0.522	1

2.3.2 Drag Coefficient

The relationship between the drag coefficient, C_D, and Reynolds number ($10^3<Re_L<10^6$) with respect to the remora model is seen in Figure 2.2. The overall trend of the simulation compares favorably with those of a streamlined body using Equations 2.4 and 2.5, and the diameter to length ratio given in Table 2.1. Equation 2.6 and the

constants in Table 2.2 are also seen to provide an excellent fit to the simulation data, and are more accurate at lower Reynolds numbers where the simulation results deviate slightly from the streamlined body approximation.

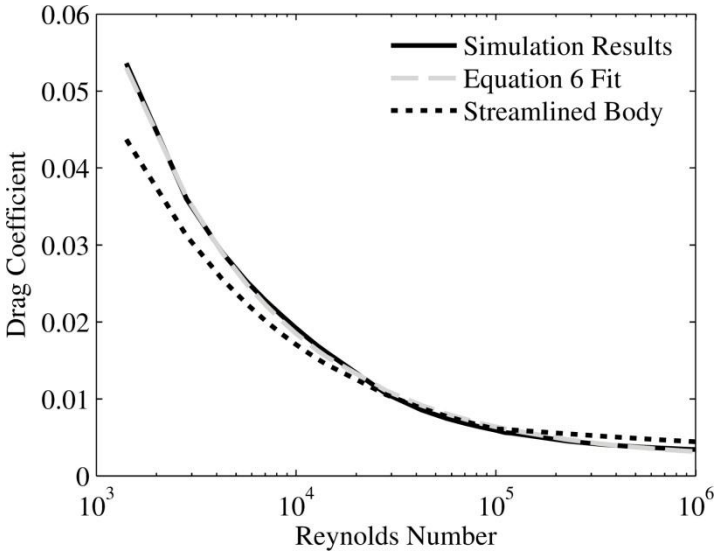

Figure 2.2: Drag coefficient computed for remora model vs. Reynolds number

Figure 2.3 shows the relationship between the Reynolds number based on the remora model's length and the drag force on the remora including the effects of the boundary layer induced by altering the distance from the start of a flat plate. The maximum difference occurs between the drag force experienced nearest the start of the plate (largest) vs. that nearest the end (smallest). Additionally, Figure 2.4 shows examples of the fluid flow field along the remora's sagittal plane when the remora is attached 1 m from the start of the plate with free stream velocities of 5 mm/s and 0.5 m/s, respectively. With respect to the drag force, the boundary layer has the largest impact at lower Reynolds numbers (swimming speeds) when the remora is engulfed by the viscous boundary layer as seen in Figure 2.4(a). At higher Reynolds numbers, the effect of the

boundary layer is negligible as can be seen by the narrowing of the darkened region in Figure 2.3 and the reduced boundary layer thickness compared to the height of the remora in Figure 2.4(b).

Table 2.2: Fitting Constants for Drag Model (Equation 2.6)

Constant	Value
c_1	3.36
c_2	0.577
c_3	0.002

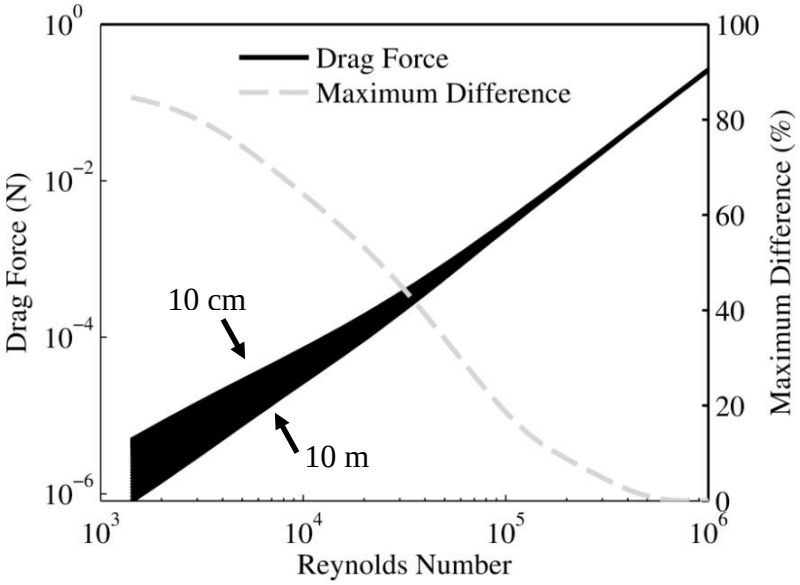

Figure 2.3: Drag force experienced by remora model at different swimming speeds including the boundary layer effects of a flat plate. The distance from the leading edge of the plate is varied from 10 cm to 10 m.

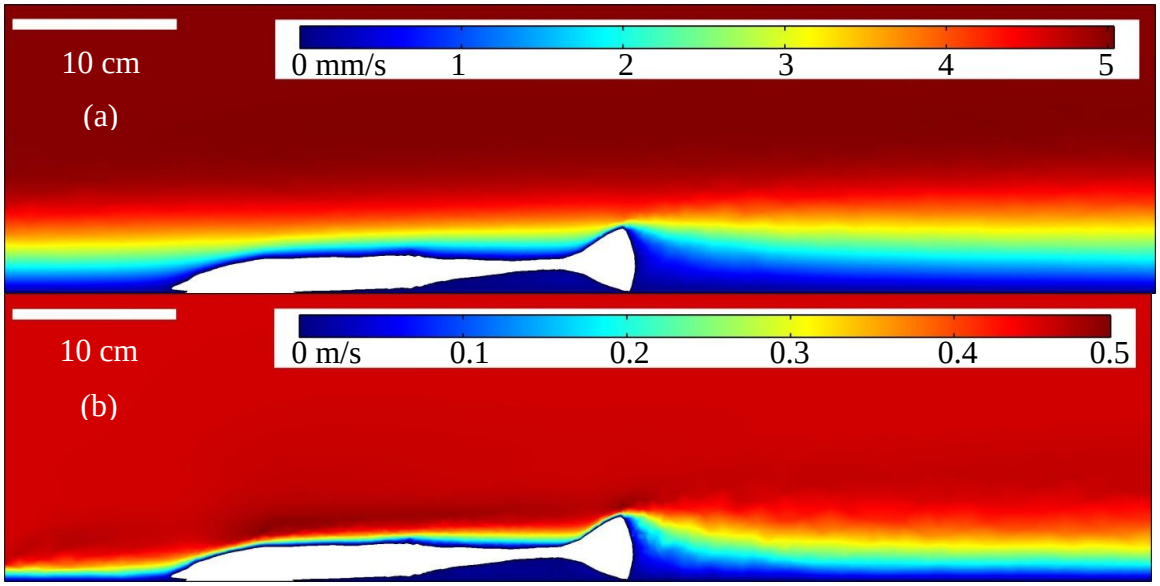

Figure 2.4: Velocity field of the remora at the sagittal plane attached 1 m from the front of a flat plate at a free stream velocity of (a) 5 mm/s and (b) 0.5 m/s

Using Equation 2.9 with the results in Tables 2.1 and 2.2, an estimate of the parasitic drag that must be supplied by the host to overcome remora attachment is seen in Figure 2.5. The parasitic drag is shown as a function of swimming speed for several different remora lengths ranging from 5 to 50 cm. The results show that a relatively long remora (50 cm) may only require a few extra watts of effort on the part of the host, even at relatively brisk swimming speeds (> 2 m/s).

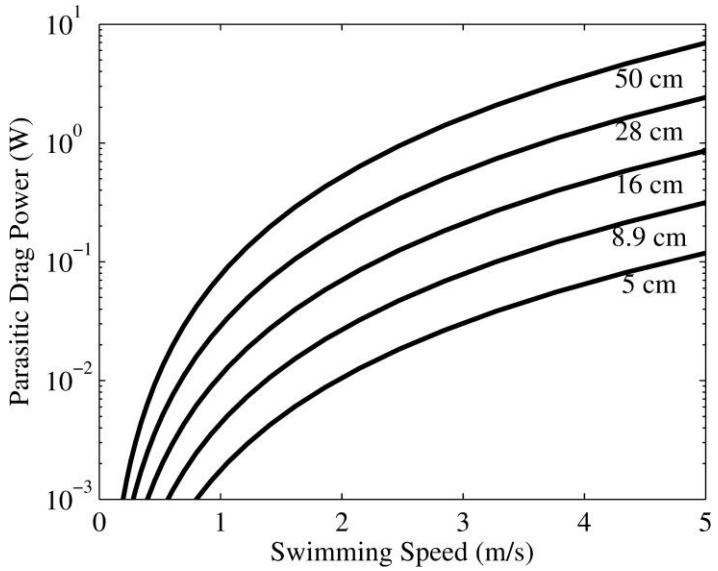

Figure 2.5: Parasitic drag power required by host to overcome attached remora at different swimming speeds. Remora length is varied from 5 to 50 cm.

2.3.3 Pull-Off Strength vs. Drag Force

By combining Equation 2.10 with the results in Tables 2.1 and 2.2, the theoretical drag force can be compared to the pull-off force necessary to overcome friction as seen in Figure 2.6. The figure shows that the drag force is several orders of magnitude below the pull-off force required to dislodge the remora at low swimming speeds (0.05 to 0.5 m/s). At higher swimming speeds (5 m/s) the ratio of the drag force to the pull-off force reaches almost 10% (N=0.1), which is still comfortably below the point of detachment (N=1). The shape of the curve indicates that the ratio decreases slightly with increasing remora length.

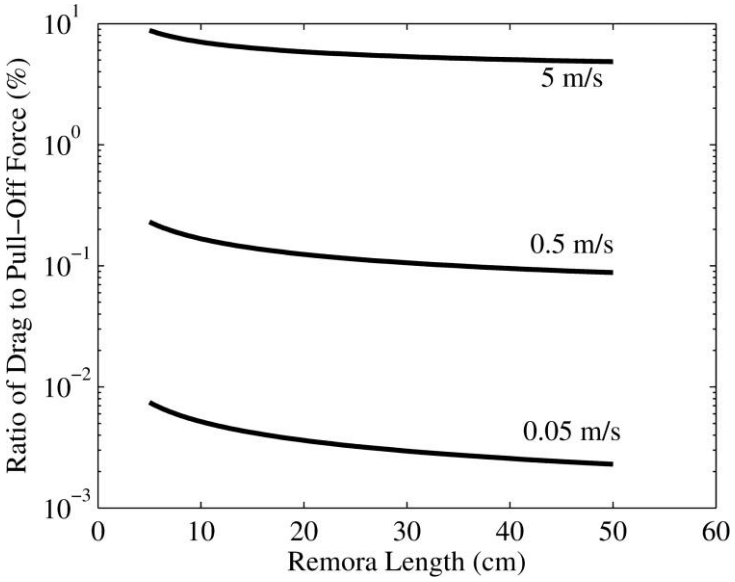

Figure 2.6: Ratio of the drag force to the experimentally measured frictional pull-off force [23] vs. overall remora length for selected host swimming speeds.

2.4 Discussion

The fact that the remora could be reasonably approximated as a streamlined body is not surprising when considering its sleek shape. Having a shape that affords minimal drag is not only advantageous to the remora, given that drag is the primary force it must overcome to maintain attachment, but also to the host as the extra effort required for swimming with an attached remora is reduced. An important metric for determining the drag on a streamlined body is its fineness ratio which is the body's length divided by its largest transverse dimension. The inverse of the fineness ratio is prominently featured in Equations 2.4 and 2.5. From [83] the optimal fineness ratio of a streamlined body exposed to the free stream is approximately 2 whereas the optimal fineness ratio of a fairing is approximately 10. A fairing is a streamlined structure often added to cover bluff projections from a surface thereby reducing drag. The fineness ratio of the remora using its largest transverse diameter from Table 2.1 was 10.5. This provides strong evidence

that the shape of the remora is optimized for hitchhiking rather than free stream swimming.

Another interesting result was that the host boundary layer did not provide the remora with a substantial drag reduction at posterior attachment locations in terms of skin friction. This is likely due to the boundary layer thickness being a stronger function of free stream velocity than position. Comparing Figure 2.4(a) and (b), it can be seen that at the low swimming speed of 5 mm/s a substantial amount of the remora did fall within the viscous boundary layer. However, even at a moderate speed of 0.5 m/s, which is comparable to the migratory speeds of remora hosts [84-87], the viscous boundary layer was already so thin that most of the remora was exposed to the free stream, and therefore little benefit was realized. Although differences between the most anterior and posterior attachment sites investigated were as high as 80 percent, these large relative differences occurred at low host speeds where drag forces are already so low that such differences are likely imperceptible to the remora. As host speed (Reynolds number) increases, the maximum difference between the drag force experienced at posterior and anterior attachment sites tends to zero. This result casts doubt on the hypothesis that remora are discriminating in their attachment location based on hydrodynamic reasons [15], at least with respect to frictional drag.

However, it remains that certain attachment sites are occupied with greater frequency than others at least with respect to dolphins, and therefore there likely exists some benefit or increased comfort level to the remora other than reduced drag. It is known that the local conditions of the attachment site play a role in remora adhesion both from experimental observation [13, 23] and theoretical considerations [26]. Because

remora adhesion is strongly suction based, an important condition for maintaining attachment is the presence of reduced pressure inside the suction pad. In order for such a pressure difference to exist, a robust seal must be maintained by the remora. One explanation for attachment site preference could be based on reduced deformation of the host tissue at the attachment site. For example, because contractions of the underlying muscles may create folds, or at least strain, in the host's skin and thereby break the remora's suction seal, the remora may choose attachment locations on the host where the underlying muscle groups are not primarily responsible for swimming. In fact, with respect to dolphins, most of the curvature (and therefore deformation of the skin) associated with locomotion occurs posterior to the dorsal fin [93], and furthermore, deformation at flank and belly attachment sites, which are preferred by remora, are insulated from the underlying muscles by a stiff subdermal connective tissue sheath and blubber layer [94]. Thus, just as it was suggested that remoras attach to locations that do not interfere with the habitual behaviors their hosts [15], perhaps remora also choose attachment locations that do not interfere with the nature of their own attachment; thereby optimizing the comfort levels of both remora and host.

Considering the parasitic drag power that remoras require of their hosts, it would appear that due to their streamlined shape only a small fraction of the thrust generated by the host goes into overcoming a single attached remora. For example, at swimming speeds of 5 m/s a bottlenose dolphin (*Tursiops truncatus*) outputs approximately 3000 to 4000 W [79, 95]. An attached remora hitchhiking at a similar speed requires less than 10 W (less than one percent of the dolphin's output). At a speed of 1.5 m/s, which is closer to a dolphin's average swimming speed, a dolphin may output approximately 90 to 280

W [79, 95], and an attached remora may require up to 0.23 W. Again, a single attached remora requires less than a percent of the dolphins output. From a metabolic standpoint, this translates into consuming an extra 2.5 to 110 g/day of sardines to move at 1.5 and 5 m/s, respectively (assuming sardines have 8 kJ/g [96]). While this seems low, it is more than a host species without remoras attached would have to consume. Additionally, it often happens that a host may have many attached remoras [10, 11, 72, 97]. In this case, the parasitic drag estimates must be multiplied by the number of attached remora; though, this provides only a lower estimate because by disrupting the flow field, the drag on the combined remora and host body may be greater than the sum of the drag experienced by each of them individually [83, 98]. Although the parasitic drag may be a small fraction of the thrust generated by a host, prolonged attachment, especially by multiple remoras, does have a negative impact on the host.

Another conclusion derived from the simulation results is that the ratio of the drag force to pull-off force (N) decreased with increasing length, suggesting that larger remoras are slightly more likely to remain attached to their host when compared to smaller remoras at the same swimming speed. Though this effect diminished rather quickly as length was increased, it may suggest, for example, that the remora becomes more suited to attachment as it matures and grows in length. In any case, the effect is explained by decreased drag coefficients resulting from larger Reynolds numbers of longer remoras compared to those of shorter remoras at the same swimming speeds.

More importantly, it is clear that regardless of remora size, it seems unlikely a host (at least a shark) will dislodge a remora by increasing its swimming speed when considering a free stream velocity of 5 m/s creates a drag force slightly less than 10

percent of the required pull-off force (N=0.1). This is in line with observations of both captive and wild remora as they are typically removed by impact with the surface of the water or other objects rather than by elevated host swimming speeds, even those proceeding jumps [8, 12, 17]. This is somewhat expected given that remoras depend on their hosts for many important needs including food, protection and transportation. These survival benefits provide strong motivation to create robust attachment.

Although the presented analysis should provide a reasonable estimate of the drag force experienced by a remora during attachment, other refinements in future work could be included. For example, more complex flow considerations such as turbulence, time dependence, flow direction, vorticity, swimming kinematics arising from host locomotion, body shape, body compliance, and multiple attached remoras could be included. Each of these factors can affect the drag experienced by both the remora and host, and most are likely to increase it. Additionally, more work on the frictional interaction between remora and host should be carried out to assess the likelihood of remora removal from other hosts.

2.5 Conclusion

The remora is an attractive platform for biological adhesion due to the strength of its attachment and low drag profile, and to these ends, a detailed estimate of the drag force it experiences while attached was presented. In general, the shape and drag forces experienced by an attached remora compared favorably to those of a streamlined body optimized for hitchhiking. From the estimated drag forces, it was found that a remora is unlikely to be removed by elevated host swimming speeds alone (at least with respect to sharks), and that larger remora are slightly less likely to be detached from their hosts than

smaller remora at the same swimming speed. Also, the lack of substantial drag reduction when the remora was subjected to its host's viscous boundary layer casts doubt as to whether the remora discriminates between attachment sites based on hydrodynamic considerations. A likely alternative explanation is that the remora chooses attachment sites to maximize its own potential for success by choosing areas of the host that are minimally deformed during locomotion.

CHAPTER 3

Measurement of Dorsal Pad Structures

3.1 Introduction

The remora (family Echeneidae) seen in Figure 3.1 has evolved an adhesive dorsal fin [6] resembling a disk-like pad spanning the majority of its dorsal-anterior surface [23]. This highly modified adaptation allows the remora to attach to a wide variety of marine hosts including sharks, sea-turtles, whales, and man-made vessels in order to "hitchhike." It has been suggested that remora adhesion is primarily suction-based, however, it has been found that the force of adhesion is significantly enhanced when attached to sharkskin as compared to a smooth surface [23].

The remora's dorsal disk consists of many developmental modifications to both hard and soft dorsal tissues. The remora's ovoid shaped disk is surrounded by a thick, fleshy lip of connective tissue that completes the external seal to a host [23] as seen in Figure 3.1 (b). This lip encloses the highly modified and intricate dorsal skeletal structure that allows for efficient attachment. The disk is filled with successive rows of pectinated lamellae [99]. Arising from each lamella is an array of iteratively patterned, ectodermally derived organs known as spinules, seen in Figure 3.1(c) and (d) [100]. These spinules are well mineralized and resemble the teeth of phylogenetically basal vertebrates such as teleosts [101] and squamates [102] (Figure 3.1 (d)).

The structural morphology of the remora adhesion system and its characteristic size scales were analyzed in order to understand how it adheres. By imaging the

specimen in the attached and detached states using dyed micro-computed tomography (μCT), optical microscopy, and scanning electron microscopy (SEM), the specimen was digitally reconstructed and characteristic features were able to be measured, such as the dorsal disk aspect ratio, spinule spacing, lamellae length and lamellae angle. The purpose of the measurements was to quantify structural similarities between specimens of significant size difference, and illustrate some applications of the data obtained. All of the measurements were made using the surface model/rendering software Rhinoceros 3D on stereolithography format (STL) files. Statistical analysis of the measurements was made using MATLAB R2009a. An understanding of the fundamental attachment mechanisms was sought with the aim to illuminate a potential alternative adhesive system to other biologically inspired systems.

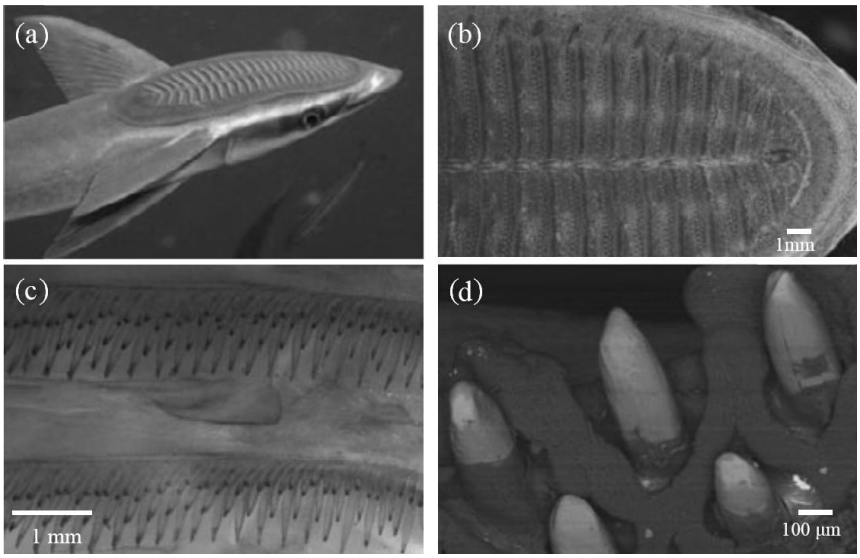

Figure 3.1: Hierarchical morphology of remora adhesive system. (a) Remora (*Echeneis naucrates*, photograph courtesy of Richard Ling). (b,c) Optical micrographs of the (b) Adhesion disk and (c) Pectinated lamellae and spinules. (d) SEM micrograph of tooth-like tips of spinules.

3.2 Materials and Methods

3.2.1 Specimen preparation

All specimens were cared for and euthanized in accordance with the guidelines and principles of the Georgia Institute of Technology Institutional Animal Care and Use Committee, protocol A11085. Remora specimens were euthanized by a 0.5 g/L dose of MS-222 (tricaine methanesulphonate). Following euthanizing and dissecting, specimens were fixed for microscopy or μCT scanning in a phosphate buffer solution of 10 volume percent formalin for a minimum of 24 hours. After fixing, specimens were washed twice and stored in 1X phosphate buffer. For specimens imaged under SEM, samples underwent solvent dehydration via submersion in increasing concentrations of ethanol in deionized water. Drying by room temperature sublimation was carried out by initially submerging in a solution of 50% hexamethyldisilazane (HMDS) in ethanol, followed by two subsequent submersions in pure HMDS. Specimens were then removed from the HMDS and allowed to dry in ambient conditions. Some specimens were then carbon coated for imaging. SEM images were obtained using a Hitachi S-4700 FEG operating at an accelerating voltage of 0.5keV, and in some cases, a Robinson backscatter detector at a working distance of 30mm. To provide contrast enhancement of soft tissues in μCT scanning, an ionic contrasting agent was introduced. This solution contained ioxaglate, Hexabrix 320 (Covidien, Hazelwood, MO), which provides 6 iodine molecules per anion. Remora sections of interest were submerged in 20mL of 40% Hexabrix/60% ion-free PBS solution for 7 days.

3.2.2 Scanning (μCT)

The remora fin was scanned in air using a uCT50 (Scanco Medical, Bruttisellen, Switzerland). X-ray source and scan settings were E = 55kVp, I = 200uA, power = 11W, integration time = 800ms, field of view (FOV) = 50mm, isotropic voxel size = 16um. Raw data reconstruction to two-dimensional greyscale tomograms was performed automatically with a convolution back-projection algorithm (pixel matrix 3092x3092, mu-scaling 2048). Greyscale tomograms were processed with global segmentation parameters to filter noise and background from tissue and used to generate binary three-dimensional renderings. Tomograms were also converted to dicom format for further image processing in OsiriX v5.5 [82]. At this stage, images were analyzed via surface, volume or multi-planar reconstruction (MPR) rendering.

3.2.3 Dermal Denticle Spacing on Shark Skin

Multiple species of remora have been observed to attach to mako shark hosts [6]. To provide a basis of comparison for remora dorsal disk spinule spacing, image analysis was performed on secondary composite SEM micrographs of a sample of mako shark (*Isurus*) dermal denticles, Figure 3.2(a), using ImageJ v1.47 image processing software [103]. An initial Gaussian blur using a sigma value of 3 pixels was followed by the application of an Otsu segmentation algorithm, Figure 3.2(b). The resulting binary images were filtered to remove features not associated with those desired and analyzed using particle counting while recording each particle's centroid coordinates, Figure 3.2(c). Each set of centroid coordinates were in turn analyzed to generate a list of nearest neighbors, from which a probability density function (PDF) was constructed using the Expectation Maximization Algorithm implemented in MATLAB [104].

Figure 3.2: Sequence depicting image processing steps for shark dermal denticle spacing measurements. (a) Original secondary SEM micrograph, (b) binary image following a blur segmentation – filter process and (c) Denticle identification and analysis

3.2.4 Measurements of Dorsal Disk Structures

The dorsal disk aspect ratio is defined as the ratio of the length of the dorsal disk to the width of the disk in the dorsal view. These dimensions are found by applying a bounding box to the surface model and measuring the length and width of the box as seen in Figure 3.3.

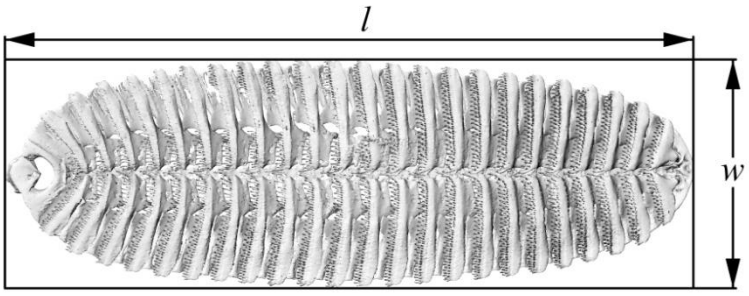

Figure 3.3: Schematic depicting the aspect ratio measurement of the dorsal pad

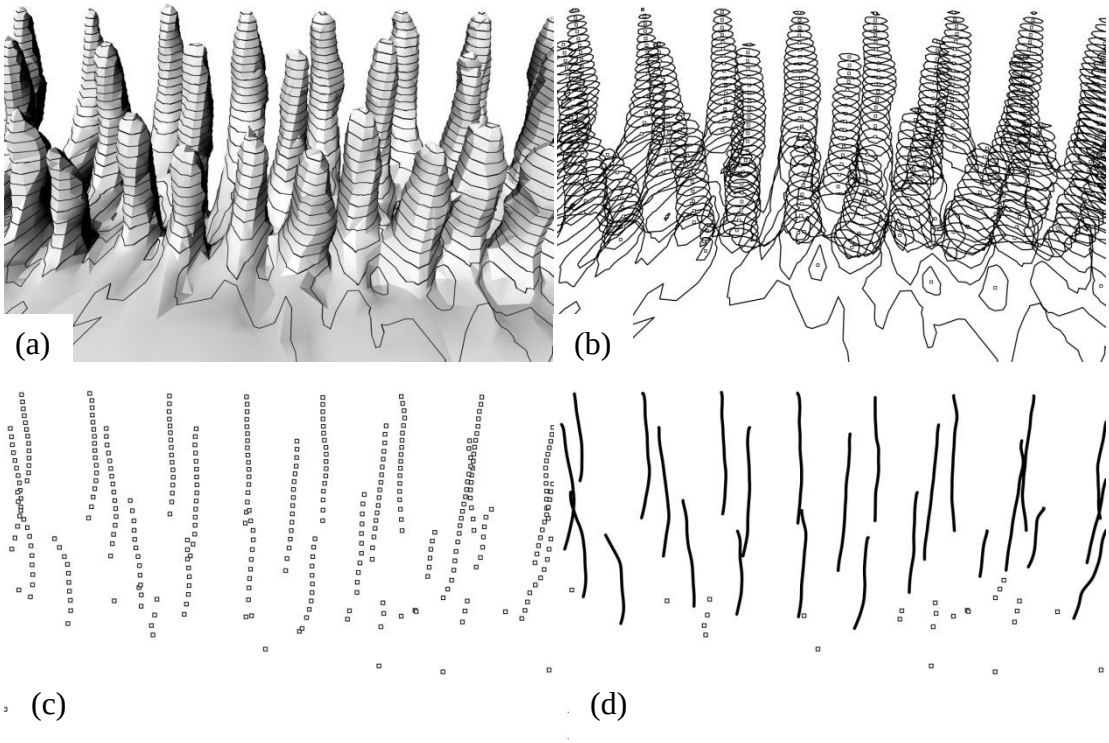

Figure 3.4: Illustration of the intermediate steps in the spinule spacing algorithm: surface sectioning (a), centroid identification (b), centroid locations (c), and grouping (d).

Spinule spacing is defined here as the minimum distance between the tip of a given spinule and the tips of all other spinules from a given set, or equivalently the tip to tip distance between nearest neighboring spinules. This measurement provides comparable distances for analyzing the geometry of a spinule set. The algorithm consists of four steps: surface sectioning, centroid identification, centroid grouping, and distance measurement. An array of closely spaced parallel lines is projected onto the surface model, effectively creating a series of intersections as seen in Figure 3.4(a). Projections that result in an open cross section are omitted. Centroids of the remaining cross sections are found (b) and grouped based on a threshold distance and a minimum group size, ensuring that all the points in a group are associated with an individual spinule (c,d). The endpoint of each group identifies the tip of each spinule. Using the tip locations, the

nearest neighbor of a given spinule is identified by comparing its distance to all the others in the set, producing a list of measurements representing the shortest inter spinule distance. From the set of nearest neighbor distances a probability density function (PDF) is constructed using the Expectation Maximization Algorithm implemented in MATLAB [104].

3.2.5 Lamella angle and length measurements

Lamella length is defined here as the length of a line parallel to an individual lamella extending from the midline of the specimen to the perimeter of the sucking disk; *L* in Figure 3.5. The lamella angle measurement is made between the same parallel line, as described by the lamella length definition, and the specimen midline; θ in Figure 3.5. The required parallel line for both measurements is obtained by performing a least squares regression of the spinule tip locations.

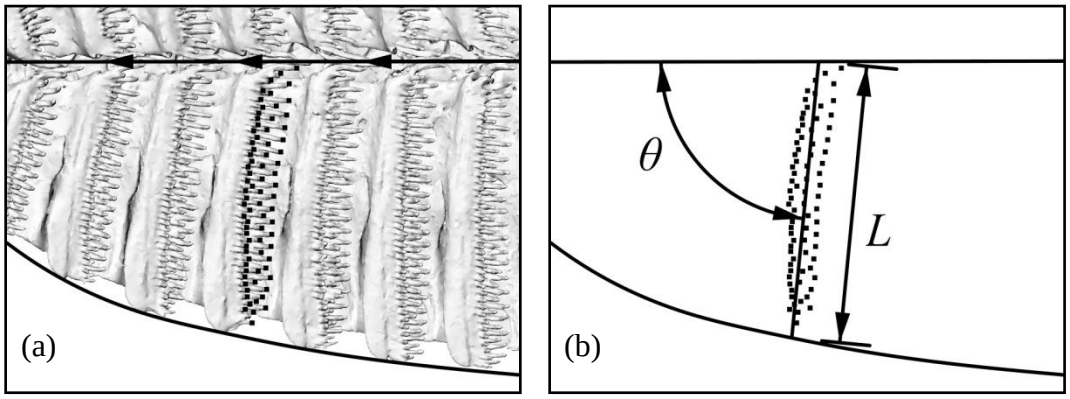

Figure 3.5: (a) Spinule locations, and specimen midline with arrows indicating posterior to anterior direction; and (b) lamella angle (θ) and length measurements (L)

3.3 Results and Discussion

3.3.1 Comparative Dorsal Disk Structural Measurements

μCT-based volume renderings of the dorsal disk's outer soft and mineralized tissues are shown in Figure 3.6. The overall disk dimensions and aspect ratios can be found in Table 3.1. The average aspect ratio of the three specimens is found to be within ±16 percent of that average. This is especially interesting when noting that Remora B is almost 2.5 times the size of both A and C.

Detailed μCT-based surface renderings of the pectinated lamellae are shown in Figure 3.7. The spinule spacing measurements performed on the left half of Remora C, due to the bilateral symmetry of the specimen, can be seen in Figure 3.8. The histogram has 50 bins each 6.6μm in size. Superimposed on the histogram is a bimodal-normal PDF with parameters described in Table 3.2.

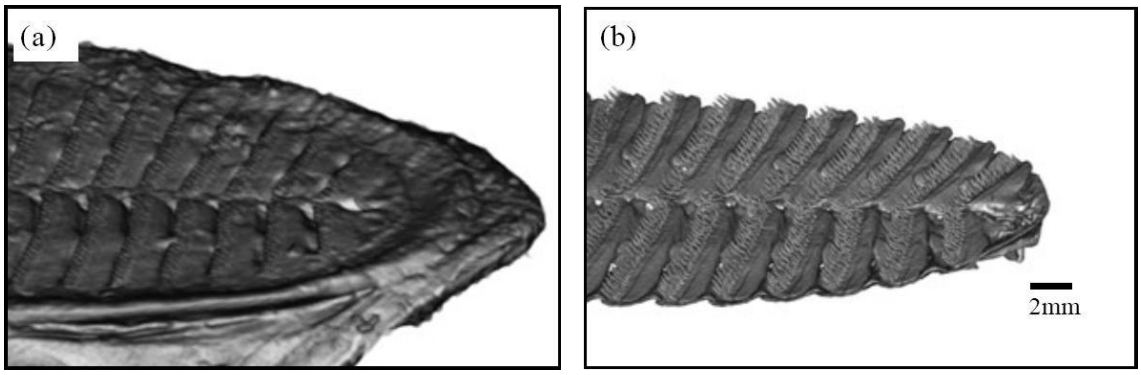

Figure 3.6: μCT images of suction disk section for segmentation values depicting (a) outer soft tissue and (b) mineralized tissue

Table 3.1: Remora Disk Aspect Ratio Measurements

Remora Specimen	Length (mm)	Width (mm)	Aspect Ratio
A	38.2	15.7	2.43
B	92.8	28.9	3.21
C	34.7	11.5	3.01
		Average	2.88

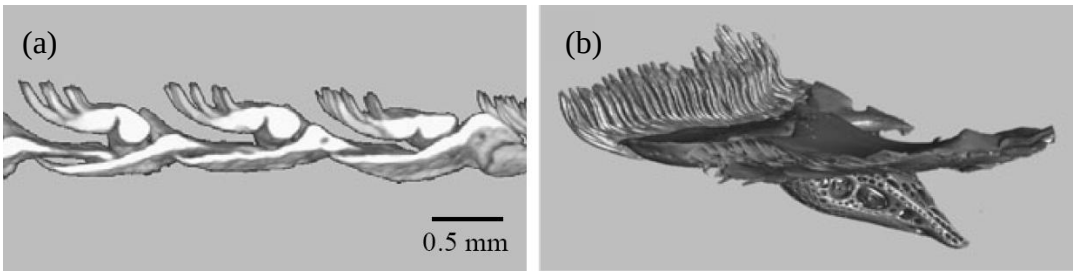

Figure 3.7: μCT rendering of pectinated lamella. (a) 1 mm thick MPR sagittal slice at 16 μCT

Table 3.2: Spinule Probability Density Function Parameters

Parameter	Distribution1	Distribution 2
Type	Gaussian	Gaussian
Mean (μm)	167	116
Standard Deviation (μm)	1.42	0.164
Mixing Coefficient	0.617	0.383
Number of Observations	1821	

The histogram exhibits two distinct peaks, corresponding to a structure that has been observed by other authors [20]. The first peak can be attributed to a row of shorter, more densely spaced spinules whereas the second peak contains another row of longer, less densely spaced spinules. The PDF confirms that the shorter spinules are more regularly spaced and densely packed than the longer spinules based on the relative height and width of the two peaks. A bimodal-distribution was selected because increasing the fit beyond two produces either extremely low mixing coefficients or clustering of the fitting parameters around the two peak values; fitting three normal distributions to the data shown in Figure 3.8, for example, gives mixing coefficients of 0.51, 0.48, and 0.01.

The spinule spacing on the remora may be compared to the scale or denticle spacing on the host. The likely hood of finding spinules spaced within a given range of values is found by integrating the PDF shown in Figure 3.8.

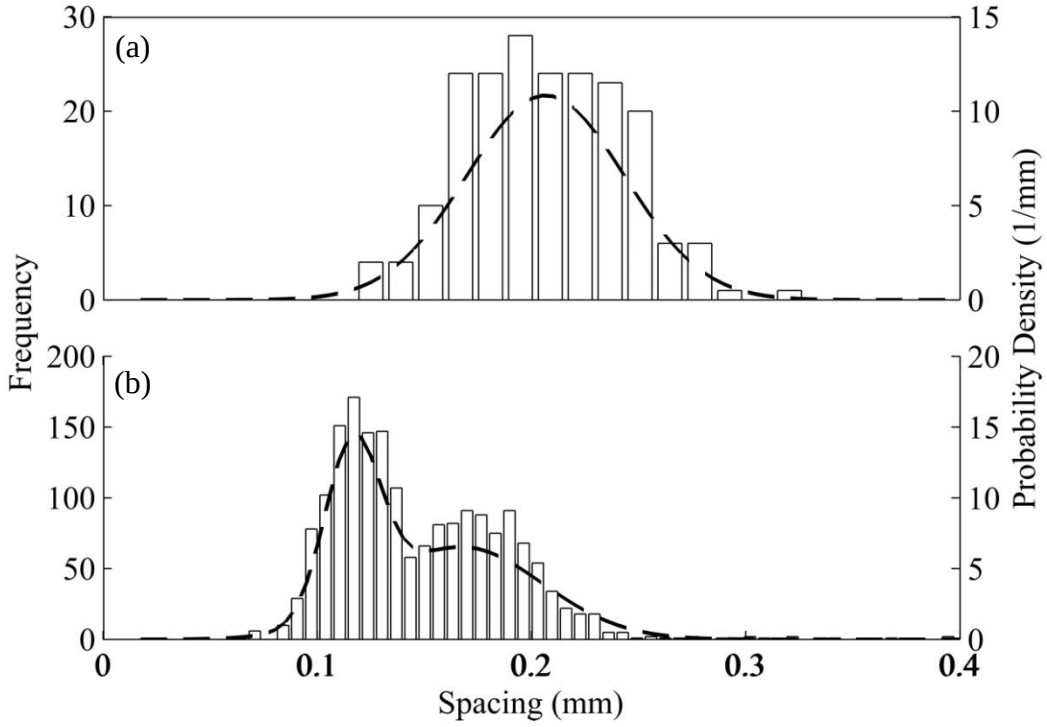

Figure 3.8: Depiction of shark denticle spacing (a) compared to Remora C spinule spacing (b)

Alternatively, the PDF of the host's denticle spacing can be compared directly to that of the remora, as in Figure 3.8. From the figure, it is apparent that the spinule and denticle spacing are very comparable based on the considerable overlap of the two distributions. These similar length scales may contribute to the larger adhesive force that has been observed when remoras are attached to shark skin compared to smoother surfaces [23].

3.3.2 Lamellae Length and Angle Measurements

Dissection has revealed that the pectinated lamellae can be elevated or depressed by a series of elegantly arranged musculature to control attachment or release from a host. Lateral depressor muscles originate from the dorsolateral neurocranial vault and attach to the ventrolateral surface of the medial pterygiophore [23]. By serially raising or depressing the lamellae, it was demonstrated that it is likely that remora have evolved an efficient system for an attached state of muscular depression.

The angle and length measurements of the left lamellae can be seen in Figures 3.9 and 3.10, respectively. The relative lamella position is defined as the ratio of lamella number to the total number of lamella on one side of the sucking disk with zero corresponding to the most anterior lamella and unity to the most posterior lamella. Referring to the position in this way facilitates comparison among the different specimens. The number of pairs of lamellae and the maximum lamella length for each specimen can be found in Table 3.3.

Tables 3.1 and 3.3 indicate that there are significant size differences between the specimens in terms of both the number of lamella pairs but even more strongly in lamella length and size. However, the normalized measurements in Figures 3.9 and 3.10 show strikingly similar inflection points and overall shape across all three specimens in terms of the change in angle and length as one progresses from anterior to posterior.

In addition to demonstrating the similarities in structure across different specimens, the measurements can also be applied to physical models that may lead to phenomenological explanations for the structure. One might hypothesize that the lamella length and angle have been optimized to resist drag force. It has been suggested that the

spinules serve to increase the attachment force between the remora and host [105]; therefore, owing to the swimming direction this suggests that most of the lamella should align themselves near 90 degrees. However, from Figure 3.9, it can be seen that although a significant fraction of the lamella lie within the vicinity of 90 degrees, some of the lamella are rotated as much as 40 degrees from 90. This may suggest that in addition to the drag force, there are likely other moments or forces with lines of action other than the swimming direction that must also be resisted by the Remora. Alternatively, it may suggest that certain lamella play a unique role during the attachment or detachment process. Regardless, the data obtained here can inform such hypotheses, models, or designs whether they are from engineering or biological backgrounds.

Table 3.3: Lamella Reference Measurements

Remora	Lamella Pairs	Maximum Lamella Length (mm)
A	17	7.90
B	21	14.19
C	23	5.92

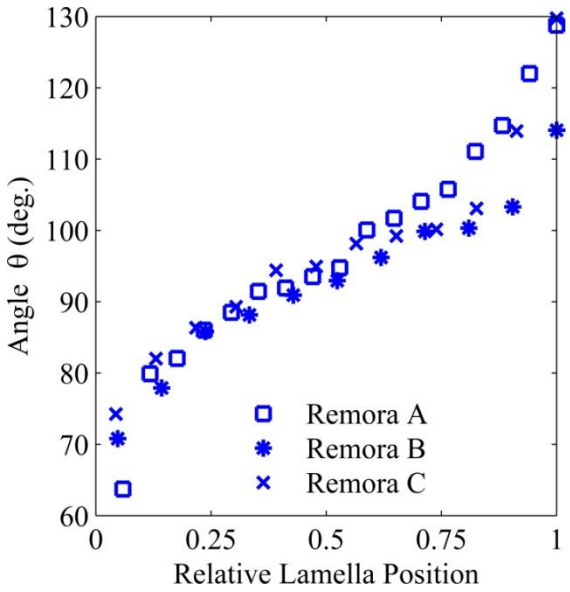

Figure 3.9: Lamella angle measurements from left half of remora specimens

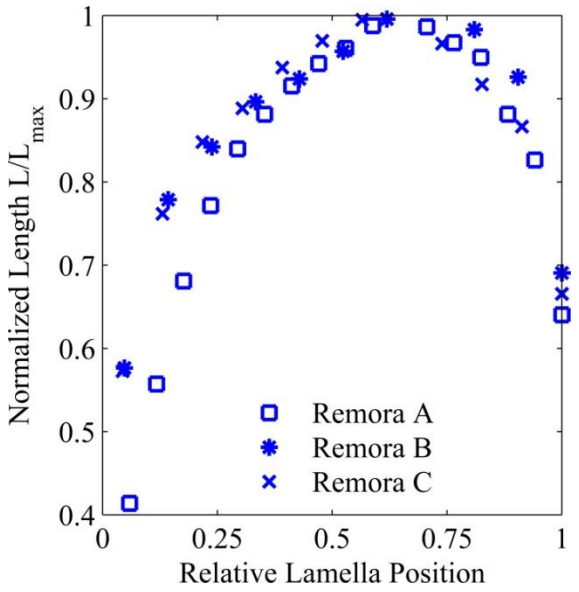

Figure 3.10: Normalized lamella length measurements from left half of remora specimens

3.4 Conclusion

Several measurement techniques were described and results were presented for three different remora dorsal suction discs. Similarities in the suction disk structure with respect to the size and position of the lamellae and spinules were illustrated despite significant overall specimen size differences. Remora spinule and shark denticle spacing were found to be of a similar length scale, which may contribute to an increased attachment force between the remora and its host. Lastly, the measurements reveal that further study is needed to fully understand the roles of the different suction disk structural elements and their interactions to create a successful attachment and detachment system.

CHAPTER 4

Spinule Friction Enhancement

4.1 Introduction

Among known suction-based attachment mechanisms in other fishes [37, 40, 52, 106], the remoras are the only group to have derived their suction apparatus from specialized dorsal fin elements. The dorsal suction pad of remoras is homologous to the dorsal fin common to other bony fish species [20]. It has been suggested that attaching to mobile hosts benefits the remoras by reducing metabolic demands for swimming [107], offering opportunistic feeding [13], or increasing the odds of finding mates [72]. Remoras have been known to strongly attach to a sharks [8, 9], rays [10], other pelagic fish [10], sea turtles [11], dolphins [12], divers [72], buoys [7], ship hulls [7], and concrete [13]. This variety of hosts moves at many different speeds and have body surfaces that span a broad spectrum of geometries and topologies [108]. Despite this remarkable behavior, there has not been experimental confirmation of the underlying mechanisms or any numerical analyses of the physical forces that contribute to this attachment function.

The remora pad has several distinct features that work in concert to achieve reversible attachment: the outer fleshy lip, an array of lamellar compartments, shown in Figure 4.1(a), and spinules that protrude from the individual lamella (Figure 4.1(b)).

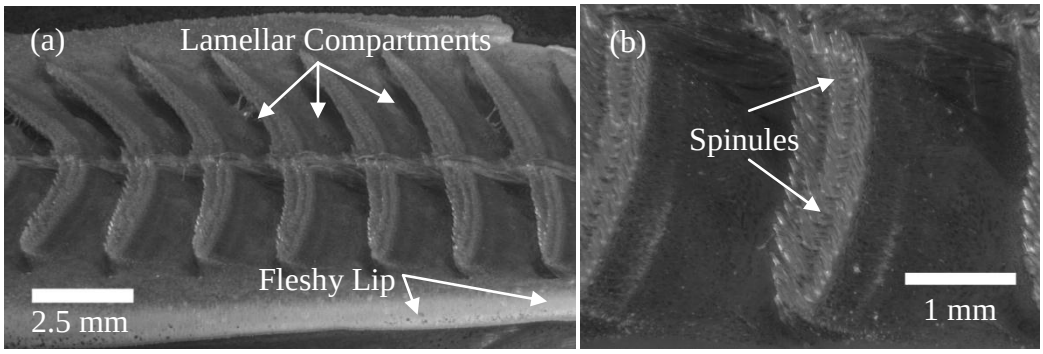

Figure 4.1: The suction disk of the remora (*Echeneis naucrates*); anterior is to the right and posterior is to the left. Optical microscope images show (a) the pad features, and (b) a close-up of the lamellar array.

A remora (*Echeneis naucrates*) has thousands of these spinules on its dorsal pad, spaced several hundred microns apart [21]. They project from the lamella and terminate as cone-like, blunted points as shown by the scanning electron microscope (SEM) image in Figure 4.2 [21]. Whereas the fleshy lip and lamellar compartments are thought to play significant roles in creating a suction seal (bonding [28]) to the host [26, 27], spinules are believed to provide a friction enhancement function. In previous experiments, where attached remoras were dislodged from both smooth Plexiglas and shark skin [23], removal from shark skin required significantly greater posterior-directed loads, despite the higher suction pressures measured on Plexiglas. By pressing their spinules against the host (contact surface), the remora is thus able resist slippage during hitchhiking. An increased friction coefficient between the remora and its host would allow the remora to withstand larger drag forces induced by host locomotion without slipping. Furthermore, because static friction is passive, it would be an efficient means to increase shear resistance without requiring increased effort on the part of the remora. Unfortunately, directly measuring friction between the spinules and a host surface in a living system would be extremely challenging.

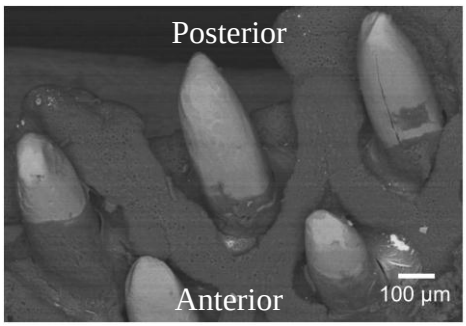

Figure 4.2: SEM image of remora (*Echeneis naucrates*) spinules protruding from lamella [21]

The current work aims to describe the effect of surface roughness on friction at the interface between an attached remora and its host. The contribution of the spinules to attachment is described by applying a friction model to the interaction of spinule tips and the essential features of a host's surface topology. The spinules are treated as individual styli that ratchet over host surface asperities. A three-dimensional model of friction is developed that considers the geometry of remora spinules obtained from micro-computed tomography (μCT), and host surface topology measurements from confocal microscopy. Model results are compared to directly measured friction coefficients of both natural and synthetic spinules on substrates with prescribed roughness. Finally, the effects of friction between remora spinules and shark dermal denticles are analyzed in terms of spinule geometry and lamellar location.

4.2 Modeling

4.2.1 Rough Contact Surface

The contact surface topology was characterized by its radially symmetric power spectrum, $C(\omega)$, which was obtained using two dimensional Fast Fourier Transform

(FFT) techniques [109]. Often, the power spectrums of real surfaces obey a power law relationship with respect to spatial frequency, ω, as seen in Equation 4.1 where α and β are fitting constants.

$$C(\omega) = \alpha\omega^{\beta} \tag{4.1}$$

This characterization allowed the contact surface to be separated into its individual amplitude, A, and frequency (or wavelength, $L=2\pi/\omega$) components [110]. When the two components are combined with Equations 4.2-4.4, the contact surface at a particular spatial wavelength is represented by the periodic surface shown in Figure 4.3(a), where u and v are parameters and X, Y, and Z are spatial coordinates.

$$X = uL \tag{4.2}$$

$$Y = vL \tag{4.3}$$

$$Z = A\left(\cos(2\pi u) + \cos(2\pi v)\right),\ u, v \in [0,1] \tag{4.4}$$

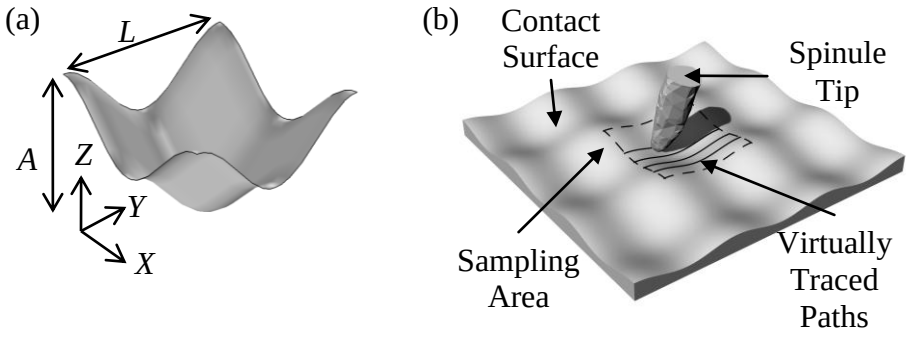

Figure 4.3: A single component (wavelength and amplitude) from the contact surface's spectrum is parameterized by the periodic, repeating surface shown in (a). A three-dimensional contact analysis is performed over all the components in the power spectrum, whereby (b) individual spinules trace (solid lines) a single period (broken lines) of a component to determine the local slope at the interface.

Representing the contact surface in this way had the benefit of reducing computation, but also allowed for the identification of asperity heights and wavelengths that contributed significantly to friction enhancement.

4.2.2 Ratcheting Friction and Spinules

On a global (macroscopic) scale, friction is manifested as the resistance of motion between two contacting surfaces [111]. At the interface between mating materials, local asperities can play a critical role in friction. For example, in systems where fibers slide along a hard surface or when one surface is in contact with much rougher surface of approximately equal hardness, a "ratchet" mechanism exists whereby local asperities move past and climb over one another during sliding [111-114]. In theory, with respect to the remora, when spinules make contact with a rough surface, the local asperities interlock with the spinules resulting in increased friction.

At the local (microscopic) scale, asperities increase shearing force, $\vec{F}_P$, on the spinule required to overcome the friction force, $\vec{F}_F$, by increasing the slope at contact surface, θ, with respect to the applied contact force, $\vec{F}_W$, seen in Figure 4.4(a). By balancing the forces in Figure 4.4(a) and employing the usual definition of friction, Equation 4.5 [111, 112] relates the local, μ_0, and global, μ, friction coefficients. The local friction coefficient represents the true adhesive friction coefficient occurring between a spinule and an asperity, whereas the global friction coefficient represents the observed coefficient aligned with the global vertical and horizontal axis [112]. With respect to the remora, shearing forces may be induced by drag associated with host locomotion, whereas contact forces may be supplied by suction and the elasticity of the remora's soft

tissues. However, Equation 4.5 states that regardless of the origins of the contact ($\vec{F}_W$) and shearing ($\vec{F}_P$) forces, only knowledge of the local friction coefficient (μ_0) and surface slope (θ) are required to estimate the global friction coefficient (μ). This treatment of friction assumes that at the length scale under investigation, the phenomenological causes of friction are taken into account by the local friction coefficient.

$$\mu = \frac{\vec{F}_P}{\vec{F}_W} = \frac{\mu_0 + \tan(\theta)}{1 - \mu_0 \tan(\theta)} \text{ with } \mu_0 = \frac{\vec{F}_F}{\vec{F}_N} \qquad 4.5$$

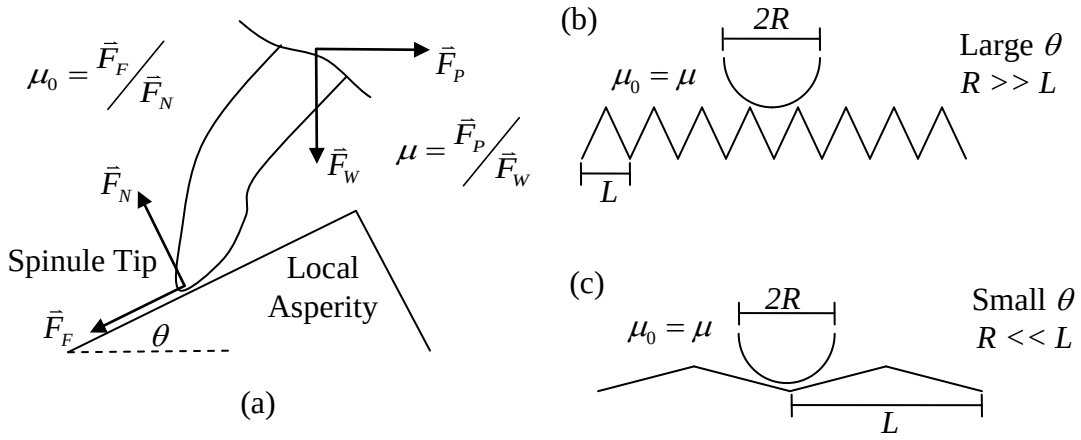

Figure 4.4: Local asperities on a surface play a critical role in friction. (a) Free body diagram of a spinule tip on a local asperity. (b) A spinule tip aliasing closely spaced asperities. (c) Asperities occurring at long wavelengths are effectively flat with respect to the spinule tip.

In addition to the slope, the distance between asperity peaks or spatial wavelength, *L*, also plays an important role in friction, as the spinule tip must be able to enter the valleys between asperities. For example, when the slope (θ) is large and the gap between peaks (*L*) is small with respect to the spinule tip radius, *R*, the spinules alias the asperity peaks and the local and global coefficients of friction converge as the spinule only touches the tips of the peaks, Figure 4.4(b). The converse is also important because a

small slope (θ) and large gap (L) with respect to tip radius (R) renders the asperities effectively flat in which case the local and global coefficients of friction again converge, Figure 4.4(c).

As seen in Figure 4.2, spinules are geometrically complex, and thus are not well suited for a single parameter description; therefore, the full three-dimensional geometry was taken into account here. Working in Rhinoceros (Version 5, Seattle, WA, USA), individual spinules and tip locations were identified using algorithms developed in [21]. An interesting feature observed with respect to the spinules was that for an individual lamella, all of the spinules terminate in approximately the same plane despite differences in respective spinule lengths. This plane provided a natural and objective orientation for the lamella and spinules. The equation of a plane is given by Equation 4.6, where X, Y, Z are the respective spatial coordinates.

$$aX + bY + cZ = d \tag{4.6}$$

The best-fit plane was found in a least squares sense by computing the eigenvectors of the product of matrix C and its transpose ($C^{\mathrm{T}}C$), where C was built from the respective spinule tip locations (X_i, Y_i, Z_i) as seen in Equation 4.7. The plane's normal vector was formed directly from the constants a, b, and c.

$$\begin{bmatrix} X_i & Y_i & Z_i & -1 \end{bmatrix}\begin{bmatrix} a & b & c & d \end{bmatrix}^{\mathrm{T}} = [C]\begin{bmatrix} a & b & c & d \end{bmatrix}^{\mathrm{T}} = 0 \tag{4.7}$$

Using the spinule tip locations, individual tip geometries were isolated as seen in Figure 4.3(b). The isolated spinule tip was used to virtually sample (or trace) the simplified host surface to determine how and where a spinule made contact. Due to the periodicity of the simplified host surface, only one period of the contact surface was sampled (broken lines in Figure 4.3(b)). After sampling the contact surface, the slopes

along the virtual traces were determined. The average global friction coefficient was estimated by plugging the slopes and local friction coefficient into Equation 4.5 and averaging over one period of the contact surface [112].

Once the friction analysis was performed on each individual spinule, a correlation analysis was performed to evaluate whether spinule position on the lamella was associated with friction enhancement. A coordinate system was drawn with the *Y* axis parallel to the swimming direction and the *X* axis normal to the sagittal plane (plane of bilateral symmetry), where both axes lie in the plane of best fit, as seen in Figure 4.5. The analysis compared the global coefficient of friction computed for each spinule to both its respective *X* and *Y* coordinates on the lamella.

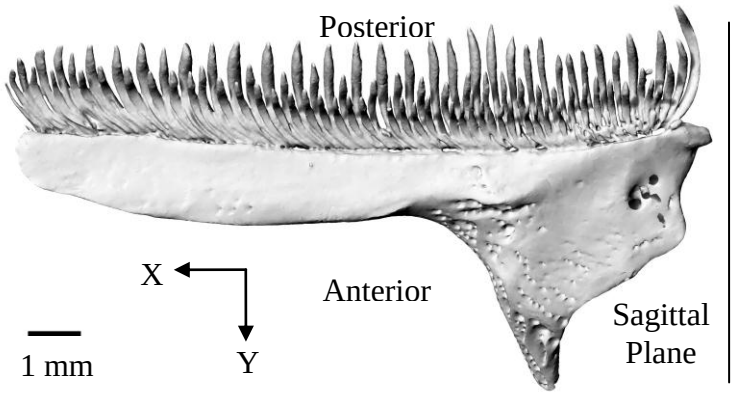

Figure 4.5: A μCT image showing the top view of the remora lamella when seen from above the best-fit plane, and the coordinate system used to locate spinule tip positions.

4.3 Methods and Materials

4.3.1 Contact Surfaces

Borosilicate glass substrates were used to create both rough and smooth contact surfaces for friction tests. Borosilicate glass was chosen because of its high stiffness and negligible plasticity to ensure the spinules operate in the ratcheting friction regime. Glass

was obtained as an optically flat substrate that provided a smooth surface. Rough surfaces were created by grinding glass substrates with 60 grit abrasive paper (Allied High Tech Products, Inc., CA, USA) on a wet polishing wheel (Allied TwinPrep 3). All surfaces were cleaned with acetone and deionized water in a sonicating bath prior to testing.

The resulting topology was measured using an Olympus LEXT 3D Material Confocal Microscope. The FFT and power spectrum of the roughened substrate were computed in MATLAB (R2009a, Natick, MA, USA) using methods outlined in [109]. Equation 4.8 relates the root mean square roughness, R_q, to the computed power spectrum (Equation 4.1), $C(\omega)$, and the measured height data, h, where ω is the spatial frequency, N is the number of data points, and L_0 is the cutoff wavelength. Calculating R_q from both the computed power spectrum and surface height data provides a check of numerical accuracy for the FFT.

$$R_q^{\,2} = 2\pi \int_{2\pi/L_0}^{\infty} C(\omega)\omega d\omega = \frac{1}{N}\sum_i \left(h_i - \bar{h}\right)^2 \tag{4.8}$$

The frequency and amplitude components of shark skin needed to parameterize the contact surface were obtained from confocal microscope data of a Shortfin Mako (*Isurus oxyrinchus*) in [26]. Shortfin Mako was chosen because it was a readily available fresh tissue specimen; preserved specimens generally had significant distortion from the preservation process.

4.3.2 Friction Measurement

Friction coefficients of both natural and artificial spinules on rough and smooth glass substrates with known topology were measured. Using the substrate topology, spinule tip geometries, and friction coefficients measured on smooth surfaces, the global

friction coefficients predicted by the ratcheting friction model were compared to corresponding friction measurements on rough surfaces. Friction measurements from the smooth surface provided values of the local friction coefficient, μ_0, because the local and global friction coefficients are equivalent on smooth surfaces ($\theta = 0$ in Equation 4.5).

Artificial spinules, Figure 4.6, were created from borosilicate glass rods to ensure they were of similar hardness to the substrates. The rods were drawn down to diameters (approximately 650 μm) comparable to natural spinules. The tips were created by grinding the drawn rods to a point using successively finer grit abrasive paper (max 1400 grit) on a wet polishing wheel. Three artificial spinules were mounted to a block in a tripod formation to ensure each would maintain contact with the substrate.

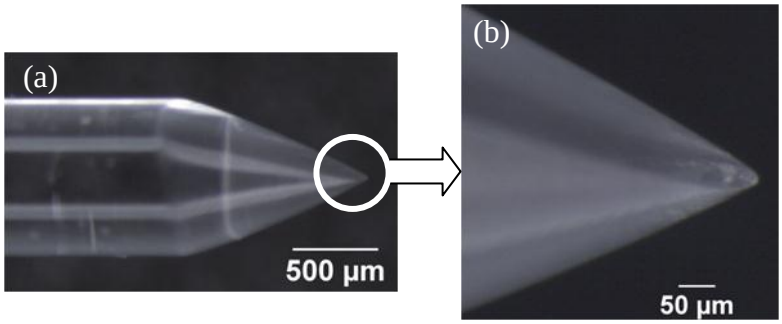

Figure 4.6**:** Optical microscope image of a fabricated artificial spinule (a) and its tip shape (b).

Natural spinules were provided by a fixed remora (*Echeneis naucrates*) specimen [21]. Only the spinules of the specimen made contact with the test substrates as the fixing process rendered them erect and free from soft tissue interference as seen in Figure 4.1. The tip geometries of 92 spinules were obtained from a high resolution μCT scan of an individual lamella seen in Figure 4.5 [26]. For the interface between remora and shark skin, it was not possible to measure the local coefficient of friction between denticles and

spinules directly as altering the natural geometry would have exposed underlying tissues of the denticles with differing local properties than the outer surface. However, the global coefficient of friction for remora and shark skin was computed from measured data in [23] which yielded a value of approximately 0.22±0.07. The local friction coefficient was obtained by iteratively solving the friction model with different local friction coefficient inputs until the desired global friction coefficient was obtained.

Friction coefficients were measured using the apparatus shown in Figure 4.7 conforming to ASTM D1894 [115]. Prior to testing, a film of storage solution from the remora specimen (1X phosphate buffer) was manually applied to the substrate to both simulate the remora's fluid environment and provide consistency between trials. A light weight, flexible, low stretch cord connected the test specimen to a force gauge (Mark-10 M5-20) through a low friction pulley. The force gauge's displacement was controlled by a test frame (Mark-10 ESM301), and in each test, the gauge moved at constant velocity (75 mm/min). Friction coefficients were computed as the force measured by the gauge divided by the combined force of the specimen's weight (37.7g) and any added weights, as in Equation 4.5. The remora's mass changed by less than one percent during testing, and all tests were carried out at 25°C.

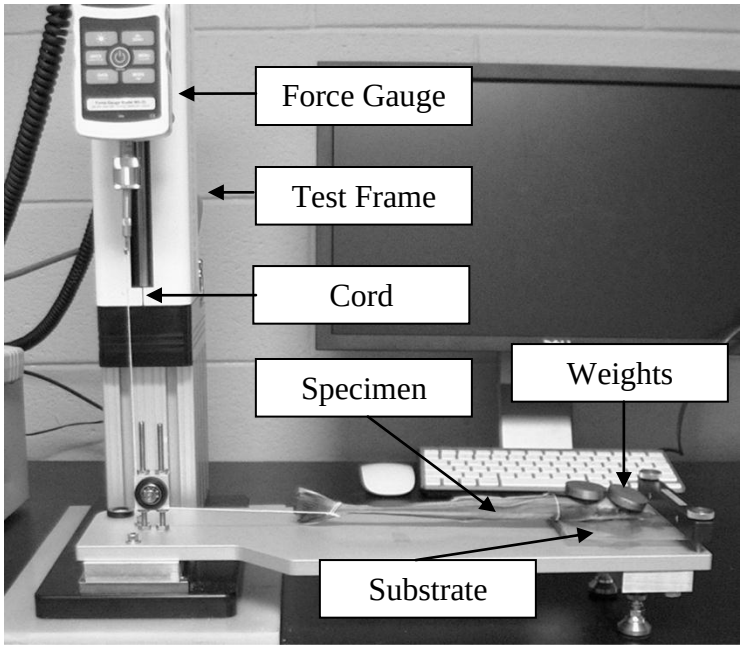

Figure 4.7: Diagram of the displacement-controlled, force-measurement system used to determine friction coefficients (shown operating with a remora specimen).

4.4 Results

4.4.1 Contact Surfaces

The power spectrum, $C(\omega)$, of the roughened glass substrate is seen in Figure 4.8. The corresponding two dimensional FFT is shown in the *inset* and clearly displays circular symmetry. The exponential decay of the power spectrum is also evident as the intensity of the roughness drops linearly with respect to frequency on a log-log scale. Excellent agreement was observed between the directly computed root mean square surface roughness (2.99 μm) and the power law approximation (2.95 μm) with Equation 4.8.

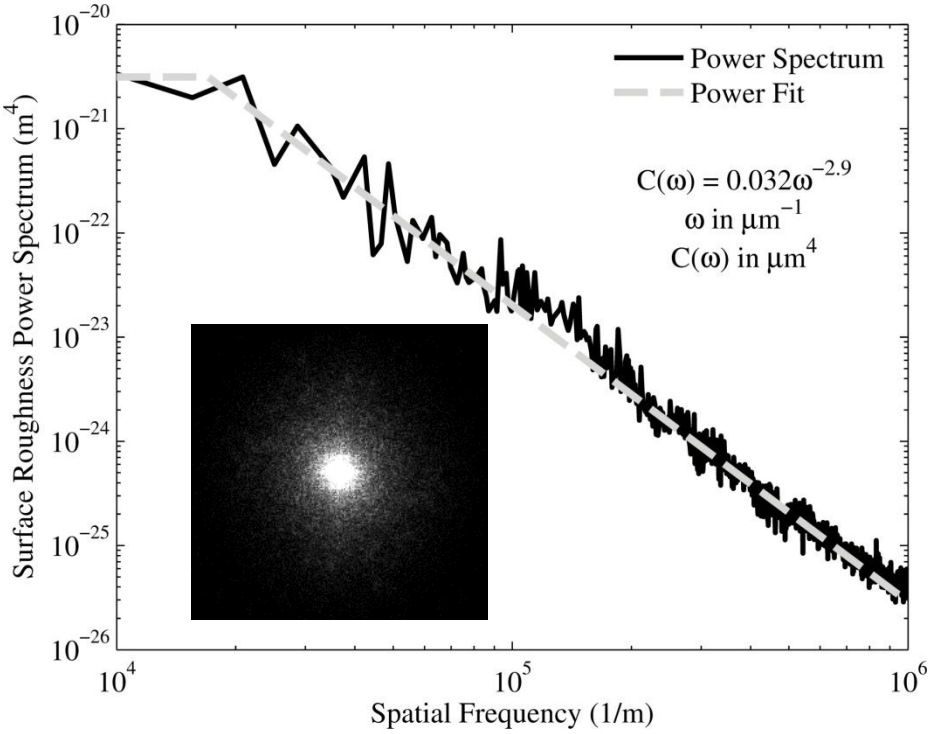

Figure 4.8: Power spectrum of the roughened glass substrate corresponding to the radial average of its two dimensional FFT (inset). The cut off wavelength is approximately 369 μm and the root mean square roughness is 2.99 μm.

The radially averaged power spectrum of a denticle surface from a Shortfin Mako shark is shown in Figure 4.9 [26]. The two dimensional FFT shown in Figure 4.9(b) exhibits similarities between the radially averaged and posterior directed power spectra, with the exception of the frequency components along the horizontal axis (due to the denticle ridges), indicating that the average spectrum is a reasonable approximation of the shark skin in Figure 4.9(a). Excellent agreement was observed between the directly computed root mean square surface roughness (10.50 μm) and the power law approximation (10.48 μm) with Equation 4.8.

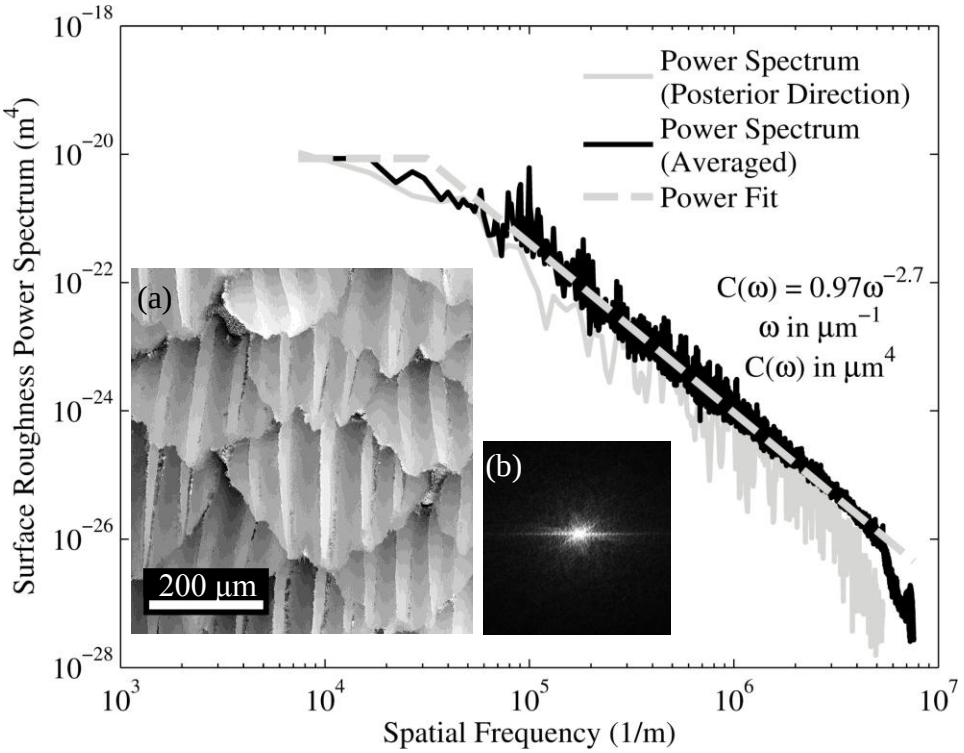

Figure 4.9: Power spectrum of a denticle surface from a Shortfin Mako shark (*Isurus oxyrinchus*). The cut off wavelength is approximately 236 μm and the root mean square roughness is 10.5 μm. The original denticle height map (a) and its two dimensional FFT (b) are also shown.

4.4.2 Friction Measurement

A summary of the friction measurements vs. model results appears in Table 4.1. Measurements using the artificial spinules on the smooth and roughened glass substrates are shown in Figure 4.10 with respect to the displacement of the force gauge. After the initial rise in the friction coefficient preceding slip, the artificial spinules exhibited uniform sliding as evidenced by the nearly constant friction coefficient (0.122±0.006) on the smooth surface. In contrast, on the rough surface, the artificial spinules moved in a "stick-slip" fashion as evidenced by rapid fluctuations in the friction coefficient (0.35±0.04). With a local coefficient of 0.122, the tip geometry from Figure 4.6, and the power spectrum from Figure 4.8, the ratio of the global to local friction coefficient (μ/μ_0) as predicted by the ratcheting friction model for the artificial spinules on the rough

substrate is shown in Figure 4.11. A comparison between the actual tip geometry from Figure 4.6 to a theoretical tip of infinite sharpness is also shown in Figure 4.11. At shorter wavelengths (less than 34 μm), the frictional responses of the theoretical (a) and actual (c) tips diverge markedly. Conversely, at longer wavelengths, it can be seen that the theoretical (b) and actual (d) tips predicted equivalent friction enhancement (μ/μ_0). The peak value of friction enhancement in Figure 4.11 (2.6±0.1) compared favorably with the observed increase in friction from the smooth to roughened substrate in Figure 4.10 (2.9±0.4).

Friction coefficients from actual remora spinules behaved similarly to artificial spinules as shown in Figure 4.12. After the initial rise preceding slip, the euthanized remora slid uniformly along the smooth substrate with a nearly constant coefficient of friction (0.081±0.002). On the rough surface, visual detection of the specimen's stick-slip motion was more difficult compared to the artificial spinules; however, the fluctuations in the friction coefficient (0.24±0.01) are clearly visible. With a local friction coefficient of 0.081, the spinule tip geometries from the μCT data in Figure 4.5, and the power spectrum from Figure 4.8, the ratio of μ/μ_0 as predicted by the ratcheting friction model for remora spinules on the roughened substrate is shown in Figure 4.13. Again, at longer wavelengths, the theoretical infinitely sharp and actual tip geometries predicted equivalent friction enhancement, but diverged sharply at shorter wavelengths. The peak value of friction enhancement in Figure 4.13 (3.3±0.5) occurred at approximately 38 μm, and compared favorably to the observed increase from Figure 4.12 (3.0±0.2).

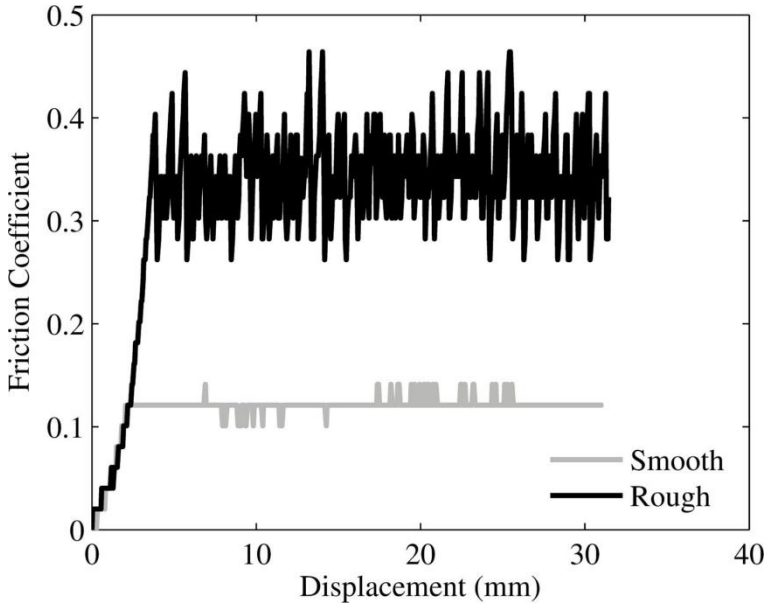

Figure 4.10: Friction coefficients of artificial spinules on rough and smooth glass substrates. During sliding, the average friction coefficients were 0.122 and 0.345 for the smooth and rough substrates.

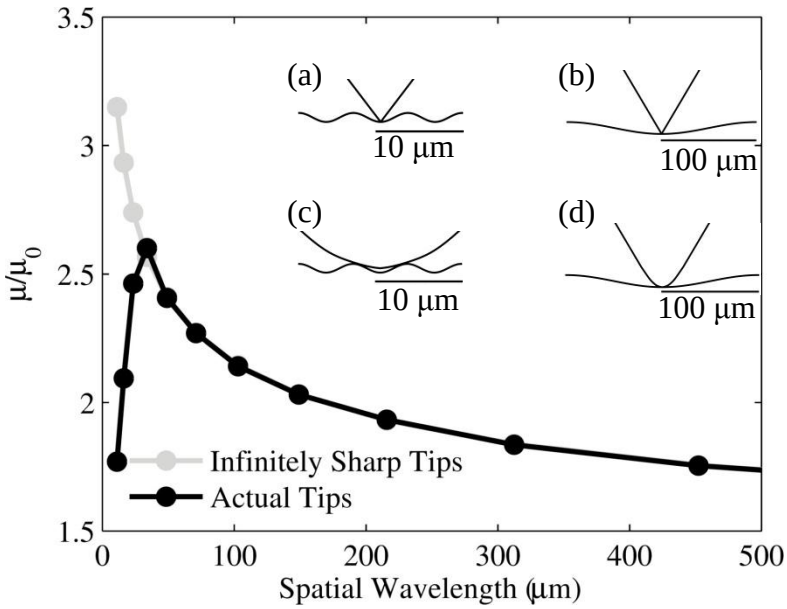

Figure 4.11: Ratio of global to local friction coefficients (μ/μ_0) predicted by the ratcheting friction model using the artificial spinule geometry and roughed glass topology compared to a theoretical, infinitely sharp tip. At short wavelengths, the responses of the two tip geometries diverge as an infinitely sharp tip (a) can move into surface valleys, but the actual tip (c) cannot. At long spatial wavelengths, friction is the same as both the infinitely sharp (b) and actual (d) tips are capable of reaching surface valleys.

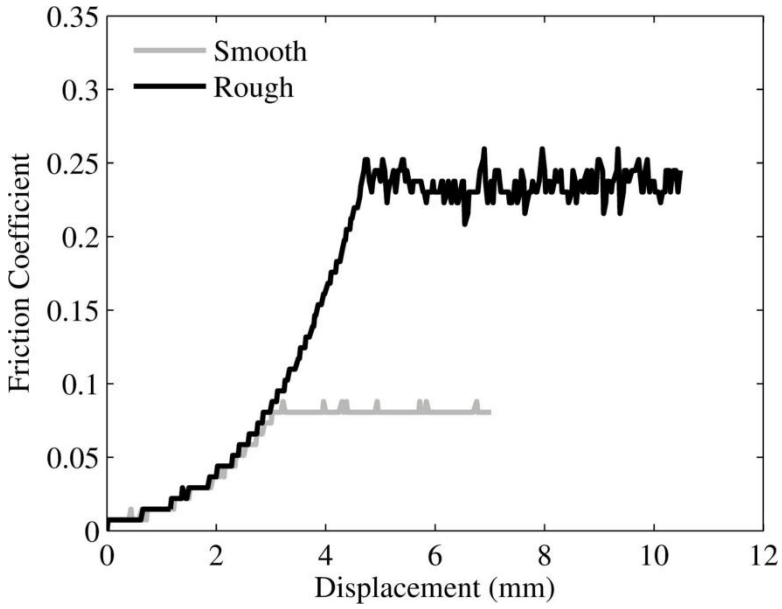

Figure 4.12: Friction coefficients of remora spinules on rough and smooth glass substrates. During sliding, the average friction coefficients were 0.081 and 0.236 for the smooth and rough substrates.

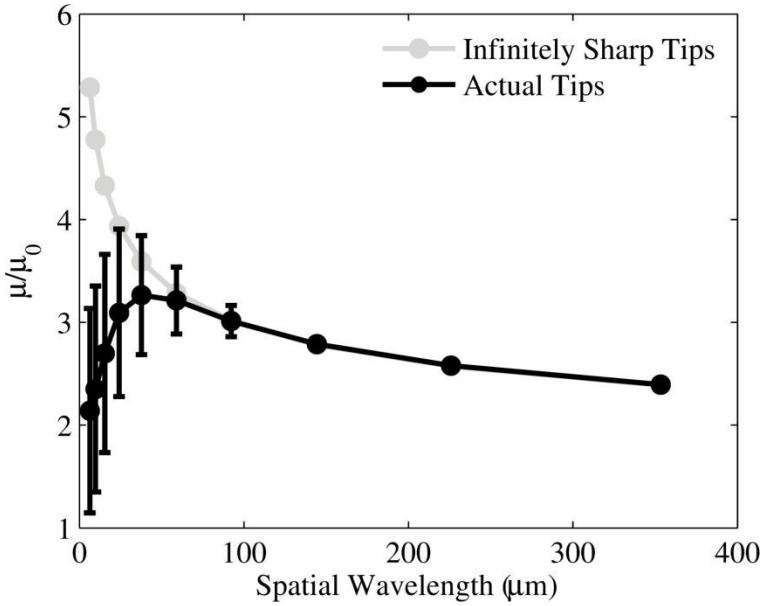

Figure 4.13: Ratio of global to local friction coefficients (μ/μ_0) averaged for all spinules at each wavelength predicted by the ratcheting friction model using remora spinule geometry and roughed glass topology compared to a theoretical, infinitely sharp tip. Error bars represent standard error (n=92) computed at each wavelength.

Figure 4.14 shows the ratio μ/μ_0 as predicted by the ratcheting friction model using the spinule geometry from Figure 4.5, the power spectrum data from Figure 4.9, and a local friction coefficient of 0.017. In contrast to both the previous cases where spinule friction was analyzed on glass substrates, the local friction coefficient was not known beforehand, but was calculated from the global friction coefficient (0.22±0.07) obtained from pull-off tests performed in [23]. The similarities and differences between the actual spinule tips and infinitely sharp tips follow the same trends as observed in previous cases. Namely, they are equivalent at longer wavelengths, and diverge at shorter wavelengths. The peak of friction enhancement (13±3) occurred at approximately 100 μm.

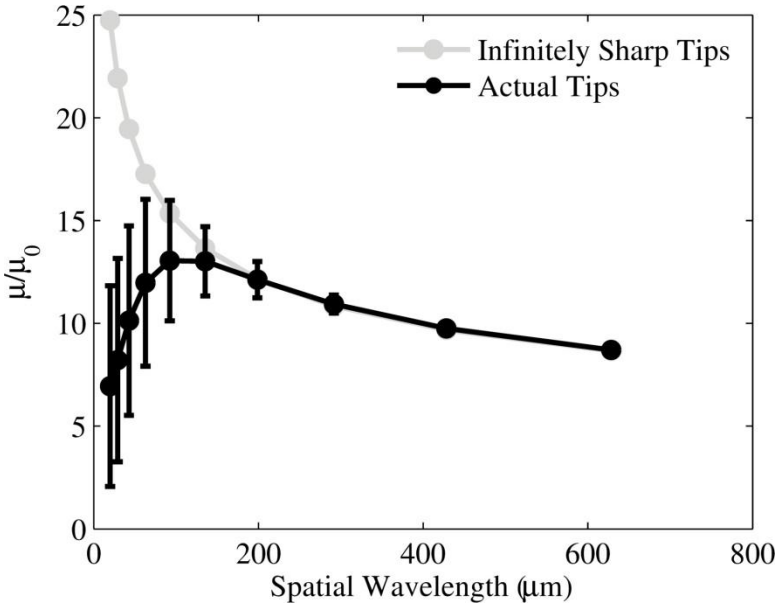

Figure 4.14**:** Ratio of global to local friction coefficients (μ/μ_0) averaged for all spinules at each wavelength predicted by the ratcheting friction model using remora spinule geometry and shark skin topology compared to a theoretical, infinitely sharp tip. Error bars represent standard error (n=92) computed at each wavelength.

Table 4.1: Summary of Friction Measurements and Simulations

Spinule Type	Smooth Substrate, μ_0	Rough Substrate, μ	Ratio (μ/μ_0)	Predicted Ratio (μ/μ_0)
Artificial (glass/glass)	0.122±0.006	0.35±0.04	2.9±0.4	2.6±0.1
Natural (tissue/glass)	0.081±0.002	0.24±0.01	3.0±0.2	3.3±0.5
Natural (from [23])	0.07±0.01 (tissue/Plexiglas)	0.22±0.07 (tissue/Shark Skin)	-	-

The correlation analysis comparing the friction enhancement peak (on shark skin) of each individual spinule within the lamella to position found no association between friction enhancement and lamellar spinule position. There was no significant correlation between the friction coefficient and sagittal *X* axis ($r = 0.103$, $n = 92$, $p = 0.326$) or swimming direction *Y* axis ($r = 0.033$, $n = 92$, $p = 0.754$) tip coordinates.

4.5 Discussion

Although the remora is typically recognized for its strong suction seal, it is important to remember that without friction an attached remora would be easily sheared off its host by drag forces. To guard against this failure, the remora uses its spinules like a bed of needles to increase friction on rough surfaces. The most important geometric property of the spinules (with respect to friction) was shown to be the tip shape because it determines the minimum wavelength that a spinule can access on a surface. This was borne out by the ratcheting friction model results seen in Figures 4.11, 4.13, and 4.14, as in each case maximum friction enhancement occurred at the minimum wavelength accessible by the spinule tips which corresponded to the measured friction enhancement shown in Figures 4.10 and 4.12. This is consistent with observations in [113] based on the fact that shorter wavelengths tend to dominate the slope of surface features for

surfaces having a power spectrum of the form given by Equation 4.1 [109]. This effect is best visualized in Figure 4.11 by comparing the friction developed by the infinitely sharp tip to the actual tip at long and short wavelengths. At long wavelengths (b,d), there is little visible difference between the two tips and both are equally capable of entering surface valleys. However, the slope of surface features is small resulting in minimal friction enhancement (Equation 4.5). Conversely, at shorter wavelengths, the actual tip geometry (c) appears almost flat compared to the contact surface whereas the infinitely sharp tip (a) is still able to fit between surface peaks and take advantage of the increased slope therein. Hence, at shorter wavelengths, sharper tip geometries can develop larger global friction coefficients.

Considering the importance of tip shape, distinct variations in sharpness were observed among the remora spinules investigated, as seen in Figure 4.15. The ratio of global to local friction coefficients (μ/μ_0) from the ratcheting friction model with respect to the 92 spinules (Figures 4.12 and 4.14) depict increased uncertainty at shorter wavelengths. Because shorter wavelengths dominate the contribution to friction, it is reasonable to attribute the increased spread in the friction model data to variance in spinule geometry. Conversely, at longer wavelengths, the spread in the data was reduced, or in other words, spinule geometry was of less importance on smoother surfaces. This is also supported by the lack of fluctuation in the measured friction coefficients on smooth surfaces vs. rough surfaces as seen in Figures 4.10 and 4.12 .

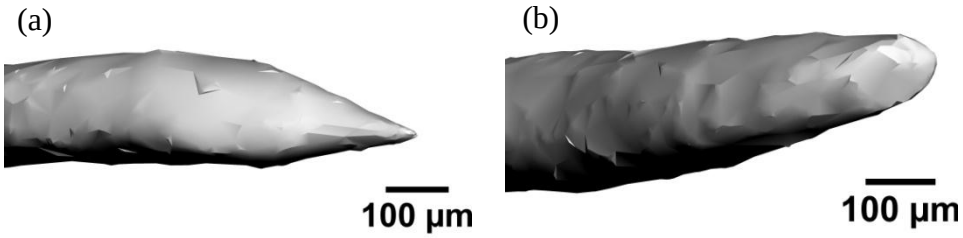

Figure 4.15: Examples of variant spinule tip geometry within same lamella are shown by µCT images of sharp (a) and blunt (b) spinules viewed from above the best-fit plane.

Despite the importance of tip shape, the correlation analysis revealed no connection between friction enhancement and lamellar position among the spinules investigated. Based on previous discussion, it follows that there was little correlation between spinule tip geometry and lamellar location. Thus, although spinule tip geometry does play a key role in friction enhancement, the sharpness or bluntness of a spinule did not appear to be related to its position on the lamella.

An important similarity between the pull-off experiments in [23] and those made here on the euthanized remora was the stick-slip motion of spinules as evidenced by the rapid fluctuations of the friction coefficient with displacement (Figure 4.12). This provides evidence to support that ratcheting friction is occurring (spinules interlocking and sliding over local asperities) in both live and euthanized remora. Additionally, although the local friction coefficient computed for shark skin (0.02) here cannot be directly compared to measurements made on smooth Plexiglas (0.07±0.01) in [23] because of material differences, the values are within the same order of magnitude. Nevertheless, all the measurements show a marked decrease in friction with surface roughness, and when the local friction coefficient can be determined, the ratcheting

friction model presented here did predict the increased friction with reasonable accuracy (Figures 4.10 -4.13).

The most prominent feature of the friction analysis for the remora on shark skin (Figure 4.14) was that the shark skin's roughness and the spinule geometries resulted in approximately an order of magnitude increase (13 times) in the global friction coefficient. This is an important adaptation for the remora because during hitchhiking, the remora must be able to resist drag forces induced by host locomotion, and increasing the contact force or suction pressure is the only mechanism available to the remora to do so. Increasing the friction coefficient by an order of magnitude permits the same friction force, and therefore drag resistance, to be obtained with an order of magnitude less suction pressure. This represents a significant energy savings to the remora, particularly if suction pressure is controlled by muscular activity.

In addition to energy savings, the increase in friction force should also allow the remora to remain attached to its host at increased host swimming speeds and during maneuvers. In fact, several studies have observed Blacktip shark (*Carcharhinus limbatus*) swimming behavior with remoras attached and found that remoras are typically dislodged by impact with either the ocean surface following re-entry after a host jump, with the ocean bottom, or on rocks rather than by swimming accelerations [8, 9]. This is an impressive feat of friction for the remora considering blacktip sharks can reach swimming speeds as high as 3.9 [89] to 6.3 [88] m/s.

A caveat of the analysis presented is that although dermal denticles themselves are quite stiff, the underlying epidermis (Figure 4.16) is compliant which allows some motion of the denticles [116]. Although the spinules were treated individually with

respect to friction, they are affixed to the lamellae, which are appreciably larger (1-10 mm) than individual denticles (100-300 μm). Thus, it seems somewhat unlikely that individual spinules could burrow between denticles. However, if the denticles were forced erect under the influence of the remora's suction, this could have the effect of further increasing the roughness of the surface, which could result in increased friction coefficients based on the analysis presented. This may help explain some of the attachment site fidelity observed in remoras [13].

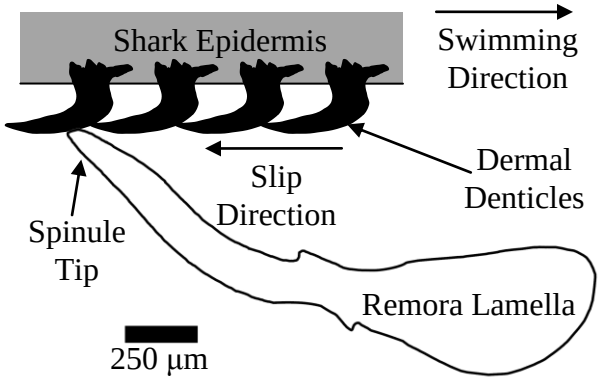

Figure 4.16: A cross section showing a spinule contacting overlapping dermal denticles where anterior is to the right and posterior is to the left.

The ratcheting friction mechanism can have interesting consequences from a design perspective. The most obvious realization is probably the incorporation sharp features into a surface to enhance friction. If the topology of the contact surface is known, then the ratcheting friction model can be used to predict the amount of friction enhancement between materials of similar hardness as was demonstrated by the fabrication of artificial spinules. By controlling the radii (or tip shape) of surface features such as oriented fibers, grit, or needles, a designer could effectively tailor the friction coefficient between two bodies in a particular application by altering geometric

parameters rather than material combinations. This could be done by reducing the features' radii such that shorter wavelengths could be accessed and larger friction coefficients obtained, or vice versa. Additionally, this concept could be reversed and the contact surface could be tailored to interact with surface features of a particular size.

Finally, in engineering applications, the ratcheting friction mechanism often plays an insignificant role [112]. This is likely because such applications generally favor controlled interactions between smooth/flat surfaces. Conversely, in natural systems where organisms frequently engage in highly uncertain interactions with rough terrain using sharp claws or claw-like features, the ratcheting friction mechanism may play a critical role in an organism's survival. This is certainly the case with remora fishes given the benefits they reap from hitchhiking and the increased friction coefficients they create with their spinules, which illustrates a unique difference between conventional and biological design.

4.6 Conclusion

The remora is a fascinating example of a biological system that employs a unique system of suction coupled with a network of articulated micro-claws (spinules) to achieve robust attachment. This work focused on the role of spinules in friction enhancement and presented a model to account for both the geometry of the spinules and host topology. Several conclusions were drawn from the results including:

1) Spinule tip shape controlled the magnitude of friction enhancement by allowing spinules to access shorter spatial wavelengths of the host surface
2) Friction enhancement associated with an individual spinule appeared to be independent of spinule location within the lamella

3) Spinule tip geometry (sharpness vs. bluntness) varied significantly among spinules on the same lamella
4) Friction enhancement previously observed between remoras and shark skin may in large part be explained by micro-scale interference between spinules and denticles

Although the model presented was applied to a remora, the methodology is general enough and was demonstrated, with the fabrication of artificial spinules, to apply to other systems operating in a similar friction regime. Therefore, future work can focus on applying the methodology outlined herein to other natural and artificial systems or in translating natural design principles to artificial systems, as is the goal of biologically inspired design.

CHAPTER 5

Lamella Deformation

5.1 Introduction

Remoras, commonly known as sucker fish, belong to the teleost family Echeneidae, and have a distinct dorsal pad proficient at attaching to an extensive assortment of marine hosts including sharks, sea-turtles, whales, and man-made vessels [2]. Three distinct features of the pad that contribute to attachment are shown in Figure 5.1 and include spinules, a fleshy lip, and lamellar compartments [21]. The lamellae are comprised of both hard and soft tissue. Several important roles played by the lamella include removal of fluid from within the pad followed by application of a restorative force against the host to maintain suction, and also delivery of the spinules to the host surface which serve to increase the "friction" or resistance to drag forces [21, 23].

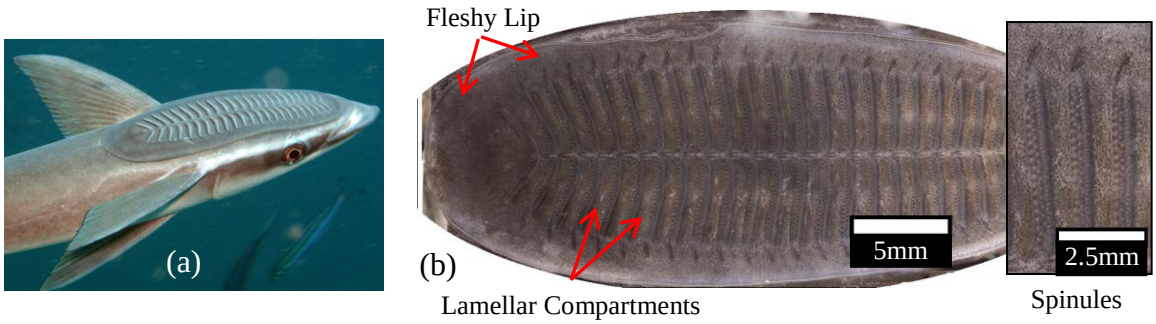

Figure 5.1: (a) Photograph of live remora suction pad. (b) Photograph of detached "suction pad" with highlighted structural features of interest

In this chapter, two finite element models (FEM) will be discussed to estimate and quantify the lamella's ability to eliminate fluid volume in response to contact with a host, and the complex structural stiffness of the lamellar array. These criteria are useful in both biological and engineering contexts as they further understanding of the remora behavior and can be used as design criteria for biologically inspired devices.

5.2 Materials and Methods

The lamellar structure within the remora pad serves to remove or "sweep away" fluid from the interface between the remora and host, and act as a "suspension system" in response to oscillatory loading resulting from host locomotion. The following sections describe computer simulations that quantify these functions by combining measured geometric and material properties of a remora's suction pad. In order to simplify computational requirements, a periodic, two-dimensional treatment of the lamellar structure was carried out to facilitate reasonable estimation of these quantities in a timely fashion.

5.2.1 Geometry

The geometry of the lamellar region was derived from micro-computed tomography (μCT) of a remora specimen [21]. Representative scans of the pad's geometry segmented into the soft and mineralized tissue domains can be seen in Figure 5.2 (a) and (b), respectively.

Figure 5.2 illustrates the complex and intricate nature of the remora's dorsal pad; as such, simplifications of the structure were sought to facilitate modeling efforts. Lamellae have bilateral symmetry, are approximately the same length, and their orientations with respect to the sagittal plane differ by only a few degrees [21]. This

suggests it is reasonable to approximate the structural mechanics of the all the lamellae within the pad by a single lamella with periodic boundires. Furthermore, there is substantial cross sectional regularity when traversing a lamella normal to the sagittal plane, therefore it is also reasonable to seek a two-dimensional representation. The consequences of these simplifications included neglecting end effects and other out of plane behaviors related to the non-prismatic nature of the lamella; however, there were substantial reductions in computational resources.

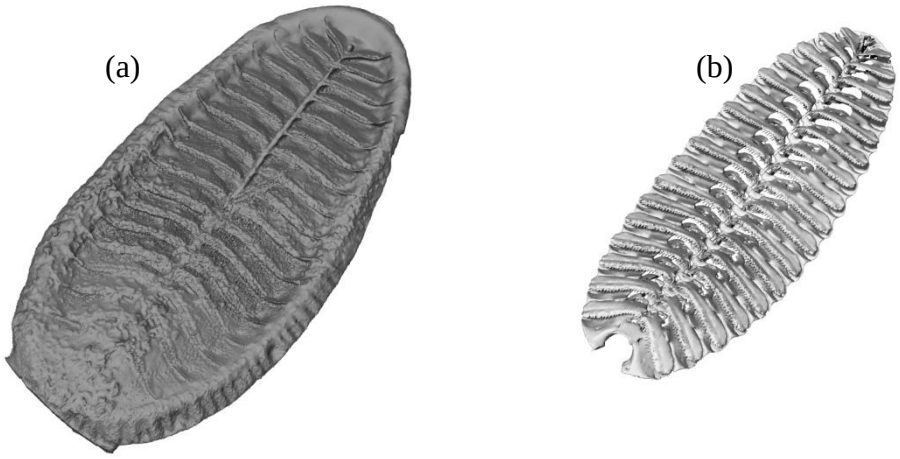

Figure 5.2: μCT scans of remora pad soft (a) and mineralized (b) tissues

To obtain a two-dimensional representation of the lamellae, cross sections of the pad were taken at two levels of resolution to capture both the local detail of an individual lamella and their periodic arrangement within the pad. Figure 5.3 shows the progression from the original μCT cross sections to the segmented mineralized and soft tissues for both the lower resolution scan of the pad and the higher resolution scan of an individual lamella. In the scans, darker pixels represent less dense (soft) tissue and brighter pixels represent more dense (mineralized) tissues. The boundaries of the hard and soft tissues were ascertained using standard segmentation techniques available in [117].

Correspondence between the high and low resolution scans was obtained by overlaying the segmented images. After identifying the boundaries, Bezier curves were fit to the data (in a least squares sense) as shown in Figure 5.4. Note the resulting translational periodicity of boundaries on the sides of the lamella and the similarity in shape to Figure 5.3.

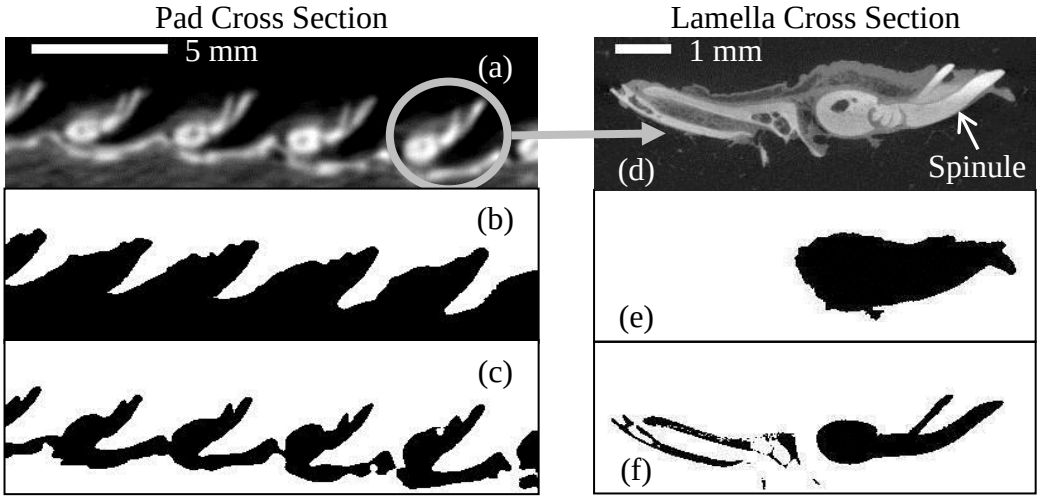

Figure 5.3: Original μCT scans (a, d) show local density increasing from darker to lighter pixels, segmented soft tissue (b, e), and hard tissue (c, f)

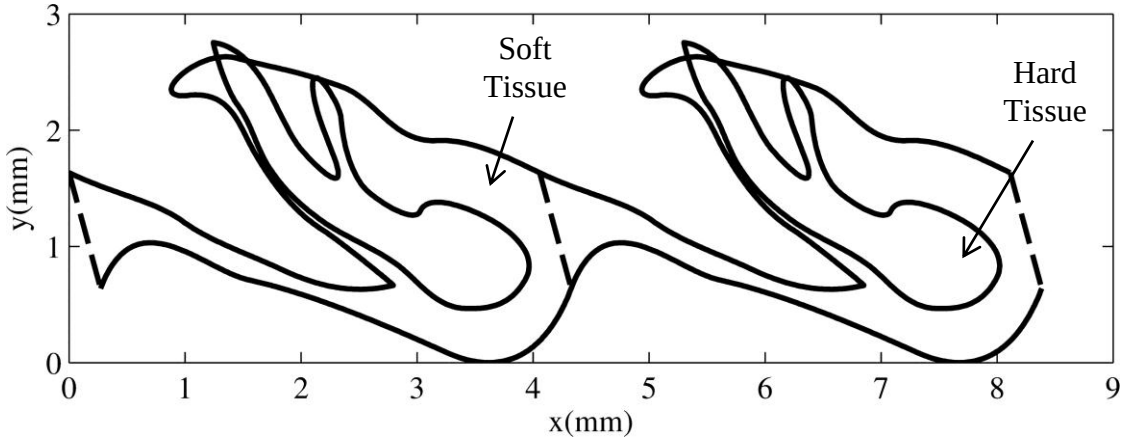

Figure 5.4: Bezier curve fit to hard and soft tissue overlay (periodicity indicated by dashed lines) which corresponds to μCT in Figure 5.3

Bezier curves were attractive for several reasons: 1) they reduced the size of the data set since only the control points of the curves needed to be stored, 2) any level of fitting accuracy could be obtained by simply increasing the number of fitting curves, 3) by limiting the number of fitting curves, a smoothing effect was obtained thereby reducing digital artifacts in the data such as "staircase" like features that show up in areas of high curvature, and 4) Bezier curves were readily imported into FEM software. Here, it was required that the Bezier curves were continuous at endpoints. This was a reasonable assumption for natural structures because it resulted in smooth geometric transitions between adjacent curves;.

5.2.2 Material Properties

To perform a structural simulation of the lamellae, material properties of both the soft and mineralized tissues were needed. The soft tissue was treated as a viscoelastic Maxwell material with relaxation modulus given by Equation 5.1, where t is time and G_0, k_n, and τ_n are material constants [57]. The values of the material constants are given in Table 5.1, which were measured by uniaxial dynamic mechanical analysis in [26].

$$G(t) = G_0 + \sum G_n = G_0 + \sum k_n e^{\frac{-t}{\tau_n}} \qquad 5.1$$

Table 5.1: Maxwell Model Material Parameters

Property	Maxwell Element			Shear Modulus (Pa)	Poisson's Ratio
	1st	2nd	3rd		
k (Pa)	860	2700	700	1330	0.495
τ (s)	0.11	0.016	0.68		

There are several studies on the mechanical properties of teleost fish bone, and here the mineralized tissue was assumed to have a Young's Modulus of 6 GPa and Poisson's ratio of 0.495 [67-69].

5.2.3 Simulations

The goals of the simulations were to estimate the fluid volume fraction reduction during attachment and the complex stiffness of an individual lamella. The domains and boundaries corresponding to the geometry in Figure 5.4 are shown in Figure 5.5.

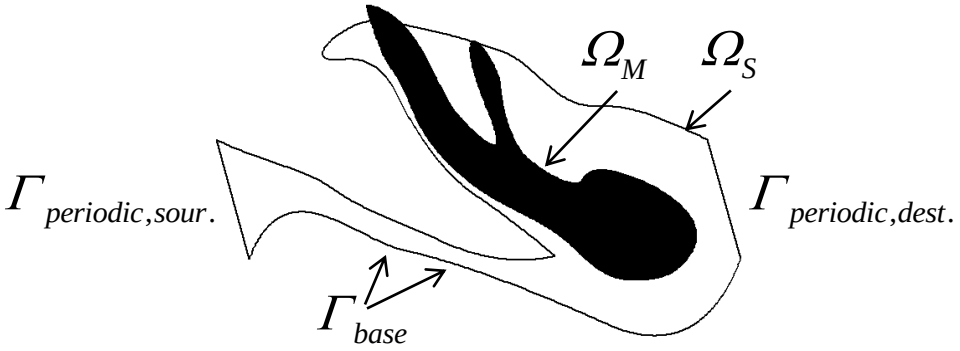

Figure 5.5: Domain and boundary identification in lamella FEM geometry

The governing equations for the soft tissue domain, Ω_s, are given by Equations 5.2, 5.4, and 5.5 which represented the viscoelastic constitutive behavior, strain tensor, and quasi-steady conservation of linear and angular momentum where $\boldsymbol{T}$ is the stress tensor, $\boldsymbol{G}$ is the relaxation modulus, $\boldsymbol{E}$ is the strain tensor, and $\boldsymbol{u}$ is the displacement vector [59]. The mineralized tissue, Ω_m, was treated as an isotropic, linear elastic solid governed by Equations 5.3-5.5, where $\boldsymbol{C}$ is the stiffness tensor.

$$\boldsymbol{T}(x,t) = \int_0^t \boldsymbol{G}(t-s) \cdot \frac{D\boldsymbol{E}}{Ds}(\boldsymbol{x},s)\, ds \text{ in } \Omega_S \qquad 5.2$$

$$\boldsymbol{T} = \boldsymbol{C} : \boldsymbol{E} \text{ in } \Omega_M \tag{5.3}$$

$$\boldsymbol{E} = \tfrac{1}{2}\left(\nabla \boldsymbol{u} + (\nabla \boldsymbol{u})^{\mathrm{T}} + (\nabla \boldsymbol{u})^{\mathrm{T}} (\nabla \boldsymbol{u})\right) \text{ in } \Omega_{M,S} \tag{5.4}$$

$$\nabla \cdot \boldsymbol{T} = 0,\ \boldsymbol{T}^{\mathrm{T}} = \boldsymbol{T} \text{ in } \Omega_{S,M} \tag{5.5}$$

$$\boldsymbol{u} = 0 \text{ on } \Gamma_{base} \tag{5.6}$$

$$\boldsymbol{u}_{sour.} = \boldsymbol{u}_{dest.} \text{ on } \Gamma_{periodic} \tag{5.7}$$

The base of the lamella, which rests on mineralized tissue, was assumed fixed as seen in Equation 5.6. Periodic boundary conditions, seen in Equation 5.7, were enforced on the sides of the lamella such that a single lamella could represent the behavior of the entire array. An important assumption implicit with the periodic boundary conditions was that all the lamellae deform simultaneously.

The above equations formed the basis of the FEM simulations, and can be solved depending of the nature of the forces acting on the lamella. It is again worth noting that the simulations were two-dimensional, and therefore all results are based on a unit length lamella.

5.3 Discussion

Two simulations were performed which estimated the relationship between deformation of the lamella and its ability to eliminate fluid volume, and the stiffness of a single lamellar structure. To simulate a remora's attachment to a host, a vertical boundary load, F_{load}, was applied to the upper, exposed surface of the spinule tip, as seen in the inset of Figure 5.6. It was assumed that the vertical force component was dominant, but in reality, additional force components may be present that also contribute to lamella deformation. Forces due to fluids leaving the pad were neglected. The fluid volume was

calculated as the space between the upper surface of the lamella and a virtual flat surface that moves with the location of the spinule tip as the lamella deforms.

The reduction of fluid volume, V_{red}, as the load, F_{load}, and lamella deformation increase is shown in Figure 5.6. Initially, there was a gradual increase in fluid volume reduction as the lamella deformed (F_{load} < 0.2 N) followed by a region of increased volume reduction with smaller changes in load as the upper portion of the lamella began to collide with the bottom of the lamella (0.2<F_{load}<0.25 N). Finally, when the lamella was almost entirely compressed, relatively large changes in loading only produced small volume reductions. It is evident from the figure that approximately 80 percent of the fluid volume was removed once the lamella was fully compressed. This is a lower bound estimate considering the compliance of the host tissue was not included.

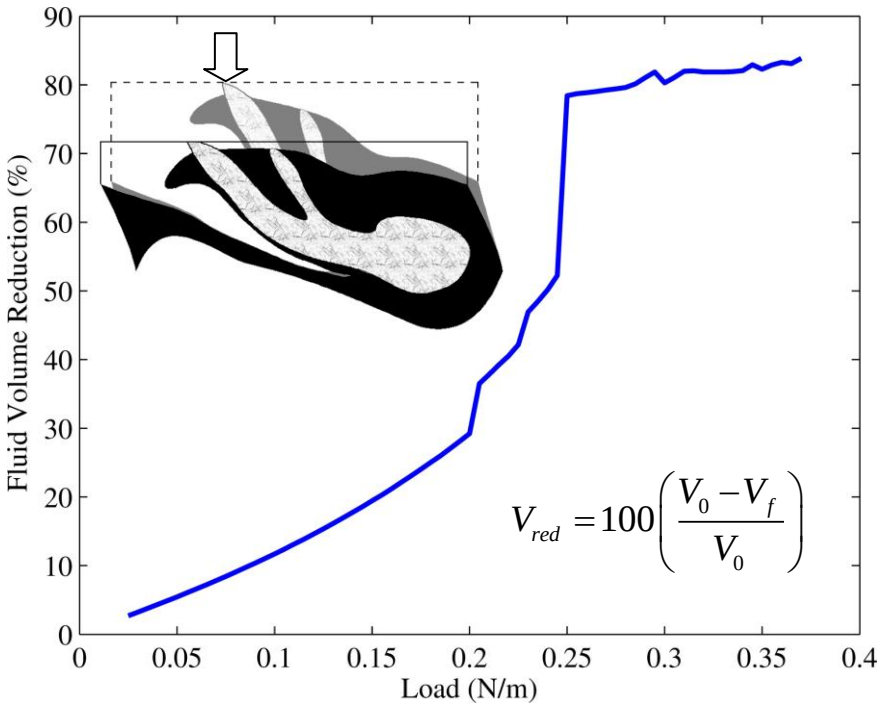

Figure 5.6: Fluid volume reduction, V_{red}, as function of applied load, F_{load}

As well as effectively eliminating fluid volume space, the lamella must also create a restorative force against the host surface to maintain attachment. Without a restorative force, the remora cannot create the required pressure difference between its pad and the ambient environment. One method with which the remora creates a restorative force is through the recoverable energy stored in its deformed lamellae. As can be seen from Figure 5.6, when the lamellae are fully compressed, they can generate a restorative force on the order 0.25-0.30 N per length of lamella. This is an efficient contribution to overall attachment since the remora does not need to exert additional effort after the initial deformation.

In addition to storing the energy necessary to create a restorative force, the lamellae are also able to dissipate vibrational energy. Figure 5.7 shows the complex structural stiffness of a lamella when a small, oscillating force is placed on the spinule tip (similar to Figure 5.6(inset)). Such a force will not create large, nonlinear deformations and elastic waves, which are factors that may be important but are beyond the scope of the present study. The loss factor was taken as the ratio of the imaginary part of the stiffness to the real part. One can see from the figure that there was non-negligible internal damping, which likely helps with both absorbing any impact associated with initial attachment and resistance to oscillatory host locomotion which likely occurs at frequencies below 10 Hz [89]. Thus, in addition to their other functions, the lamellae also act as a "suspension" system during attachment to the host.

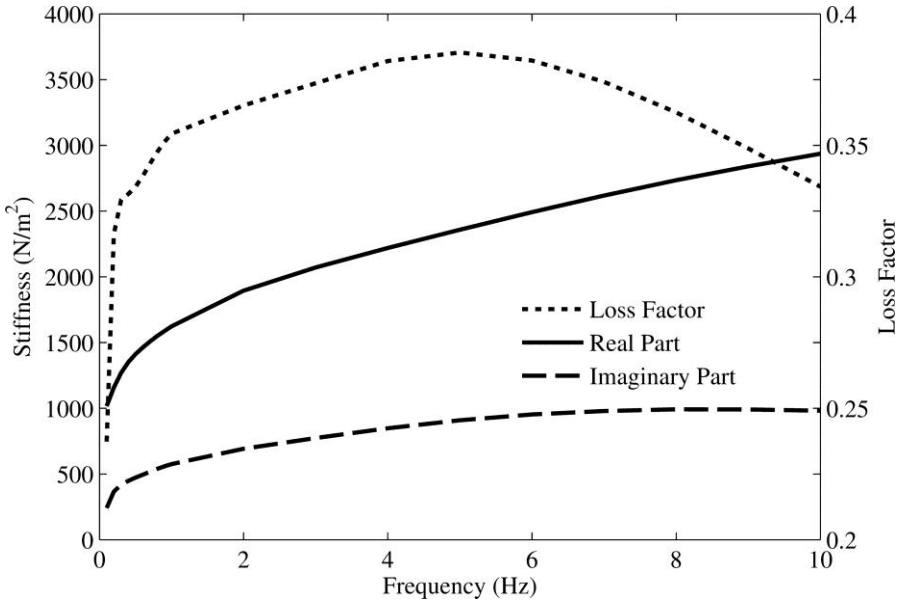

Figure 5.7: Complex stiffness of individual remora lamella based on FEM simulation with measured geometric and material properties

5.4 Conclusions

The ability of the remora pad's lamellar structure to eliminate fluid volume and respond to oscillatory loading was explored using FEM simulations based on measured geometric and material properties. The analysis presented effectively demonstrates that remora lamella are capable of eliminating nearly all of the fluid volume during attachment to a host, while also acting as a "suspension system" providing a balance between energy storage and dissipation during attachment to a moving host. Further refinements of geometric and mechanical properties in future works will likely present new aspects and advantages to remora attachment.

CHAPTER 6

Fleshy Lip Sealing Effectiveness

6.1 Introduction

Controlling fluids with proper seal and joint design has long been a topic of interest in engineering [118], and traditionally creating a proper seal that minimizes leakage requires such considerations as stiff mating members with smooth finished surfaces and adequate compression of the gasket material [119]. In natural marine environments, fluid management by the use seals occurs with the added difficulty that surface topology may be rough and uneven [37, 51]. Despite these considerations, many organisms are capable of forming robust seals against these challenging surfaces using their soft tissues and attachment structures without large compressive loads as part of their reversible attachment strategy. Cephalopods [33, 53], remora (family Echeneidae) [23], lumpsuckers (family Cyclopteridae) [39, 40], river loaches (family Balitoridae) [41] and clingfish (family Gobiesocidae) [37, 51] are examples of organisms that accomplish reversible attachment by sealing off a localized region of sub-ambient pressure between themselves and a surface. The ability of these organisms to create a seal is critical to their attachment strategy because without it, the reduced pressure that facilitates the suction-based attachment force cannot be maintained. In this chapter, a multi-scale model is implemented to predict leakage across a soft seal in contact with a rough mating surface based on the surface topology, the mechanical properties of the soft seal, and the rheological properties of the surrounding fluid.

The primary concern in any sealing application is the elimination of flow channels across the seal where leakage occurs. These channels commonly develop on rough sealing surfaces from local asperities that form gaps at the interface [109, 120]. Consider the suction pad of a remora fish (Figure 6.1(a)). By pressing its suction pad against a host, the remora is able to create a robust suction seal against a multitude of surfaces both natural and artificial including sharks, rays, other pelagic fish, sea turtles, dolphins, divers, buoys, ship hulls, and concrete [7-13, 72]. The perimeter of the suction pad is formed by soft tissue known as the fleshy lip (Figure 6.1(a,b)) which is responsible for the suction seal [21, 26]. Tissue structures in other organisms have similar functions including modified pelvic fins of clingfish [37] and lumpsuckers [39], modified ventral fins of river loaches [41] or sucker arrays in cephalopods [42, 53]. Figure 6.1(c) shows a cross-sectional schematic of the remora fleshy lip in contact with a rough substrate. During attachment as the soft tissue conforms to the attachment site (Figure 6.1(d)), sub-ambient pressure inside the pad causes fluid leakage across the seal [3, 121]. In order to maintain adhesion, leakage into the pad must be minimized as it ultimately eliminates the pressure difference due to the finite volume of the organism's attachment structures (i.e. eventually tissues will be stretched to their limit and unable to create sub-ambient pressure).

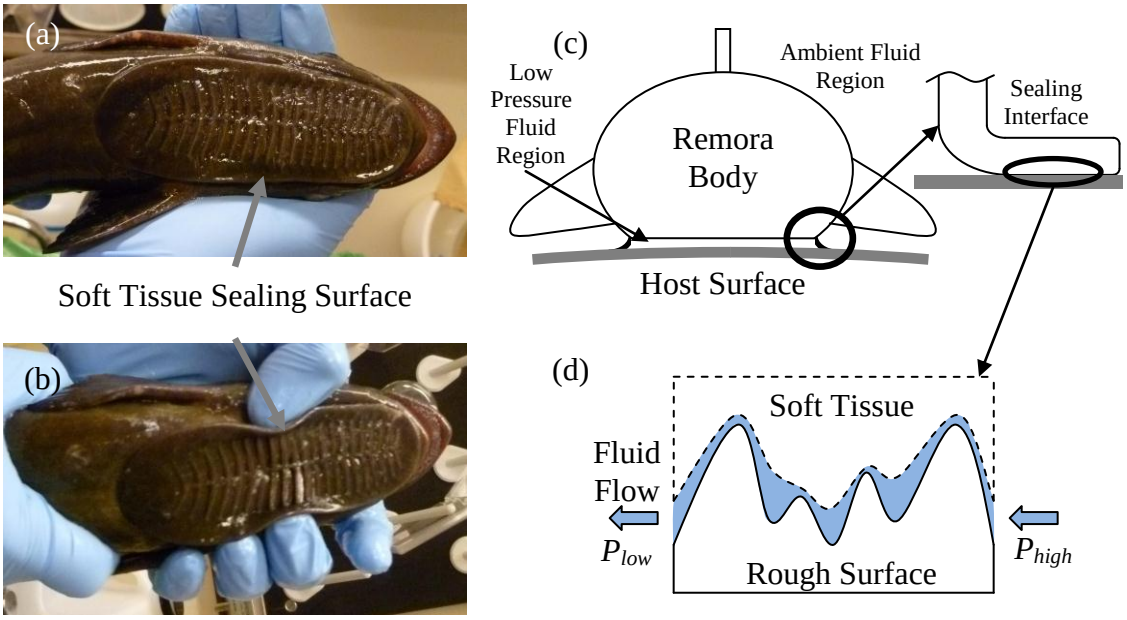

Figure 6.1: (a, b) Remora (*Echeneis naucrates*) dorsal suction pad, (c) macro-scale cross-sectional schematic of soft tissue and sealing interface, (d) micro-scale schematic of fluid flow through gaps between soft tissue and rough surface

Although prolonged attachment is beneficial to the remora [72] and other organisms utilizing suction, previous work has often evaluated attachment structures with respect to the maximum, short-term pull-off force the organism can endure without addressing other aspects of performance such as sealing effectiveness [23, 37, 39]. While the maximum pull-off force provides vital information as to an organisms' ability to withstand large disruptive forces, it does not provide information relevant to other difficult conditions such as long attachment periods to rough surfaces under moderate loads (e.g. potentially arising from fluid drag due to host locomotion or tidal motions), which may be more commonly encountered [40]. In the remora's case, long-term attachment is important for maintaining a reliable food source and locating mates [7, 13, 72], and its attachment strength exceeds the drag forces applied during sustained swimming by an order of magnitude [23]. Detachment of the remora by the host requires

extraordinary effort occasionally observed as erratic body bending or breaching behavior [8, 9, 12]. In such cases where large disruptive forces are seldom encountered and prolonged attachment is desired, the effectiveness of the seal and its ability to prevent leakage should be of primary concern.

In the following analysis, attachment site topology and the mechanical properties relevant to the soft seal are characterized. These two topics are brought together when formulating the multi-scaled model for predicting the flow rate across a soft seal. To demonstrate the model's effectiveness, an experimental apparatus is presented which measures the flow rate across a viscoelastic material in contact with a rough mating surface under the influence of a controllable pressure difference (simulating suction-based attachment conditions). The measured flow rates are compared to model predictions. Furthermore, the sealing effectiveness of a remora's suction pad in contact with sharkskin is investigated using the approach as a specific biological example.

6.2 Modeling

6.2.1 Contact Surface Topology

Given the broad range of topologies to which organisms attach, a simplified representation of the surface topology was sought to capture the most important features with respect to fluid motion across the sealing interface. Therefore, topology of the contact surface was reduced to the two component representation as seen in Figure 6.2(a). The characterizing components of the surface were the root mean square roughness, R_q, and upper cutoff wavelength, l, which when combined with Equations 6.1-6.3 (where X, Y, and Z are spatial coordinates parameterized by u and v) produce a simplified contact surface that preserves the largest peaks and valleys, which form the largest flow channels

across the seal. These two parameters were useful given that they are readily established in surface metrology and they can be obtained directly from surface power spectrum data [109, 110]. Additionally, the periodic nature of the representation (e.g. an arbitrarily large surface can be represented by translating the surface by l in the X and Y directions) facilitated a multi-scaled modeling approach.

$$X = ul \tag{6.1}$$

$$Y = vl \tag{6.2}$$

$$Z = R_q\left(\cos(2\pi u)+\cos(2\pi v)\right),\ u,v\in\left[0,1\right] \tag{6.3}$$

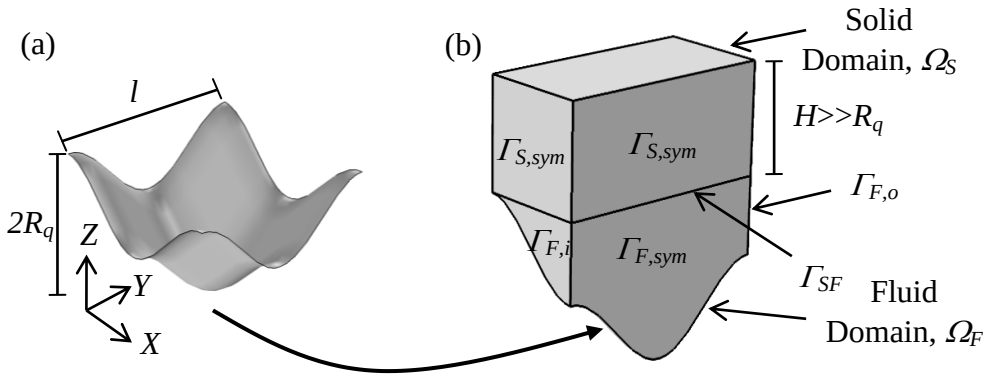

Figure 6.2: (a) Simplified contact surface and (b) cross section of unit cell showing solid and fluid domains

6.2.2 Viscoelastic Seal Properties

Soft materials such as natural tissues or manmade elastomers often exhibit time-dependent mechanical properties owing to their ability to both store and dissipate energy [57]. To account for this behavior viscoelastic constitutive laws are available, which in the linear case can be formed by discrete or continuous networks of rheological elements, or by more complex formulations in the nonlinear case [57, 60]. Here, time-dependent material properties were accounted for with a linear viscoelastic constitutive model

known as a Maxwell Model that is seen in Equation 6.4, where t is time, $G(t)$ is the relaxation modulus, and G_0, k_n, and τ_n are fitting constants. Several studies attest to the suitability of this model to describe natural tissues [26, 61, 64, 65, 122-124]. To implement Equation 6.4 it was necessary to perform mechanical testing and obtain stress/strain data for the fitting constants.

$$G(t) = G_0 + \sum k_n e^{\frac{-t}{\tau_n}} \tag{6.4}$$

6.2.3 Multi-Scale Model Description

As discussed previously, the aim of this chapter is to predict the fluid flow rate across a sealing interface. The underlying idea behind the multiple scale approach was that the microscopic channels, Figure 6.1(d), created by the interface between the local topology and the soft material were small enough (less than an order of magnitude) to be considered infinitesimal when compared to the size of the seal, Figure 6.1(c), but still of finite size such that the local microstructure exits [59, 125]. From this description, there are two length scales to consider, the local or micro-scale defined by the size of the flow channels, l in Equations 6.1 and 6.2, and the global or macro-scale defined by the width of the seal, L. Under the assumption that $L>>l$, the seal was treated as sequentially solved solid mechanics and fluid dynamics unit cell problems that resulted in a relationship between seal permeability and deformation of the soft tissue with respect to local sub-ambient pressure changes [126, 127]. Locally, the sealing interface was discretized into individual unit cells, Figure 6.2(b), with a prescribed local pressure to first determine the deformation of the solid and fluid domains. Then a prescribed local pressure gradient was applied to the deformed geometry to determine its permeability. Knowing the variation of

permeability with respect to pressure, the volumetric flow rate across the seal was obtained with Darcy's Law [127].

The solid domain, Ω_S, was governed by Equations 6.5-6.7 which represented the viscoelastic constitutive properties, strain tensor, and quasi-steady conservation of linear and angular momentum where $\boldsymbol{T}$ is the stress tensor, $\boldsymbol{G}$ is the relaxation modulus (Equation 6.4, but as a tensor here), $\boldsymbol{E}$ is the strain tensor, and $\boldsymbol{u}$ is the displacement vector [59]. The boundary conditions given in Equations 6.8-6.9 represented the symmetry of the unit cell and the applied sub-ambient pressure at the fluid-solid interface, where $\hat{n}$ is the surface unit normal vector and p_{avg} the prescribed pressure. The displacement of the fluid-solid interface was limited by a rigid contact surface based on the host topology, as described in section 6.3.1, using a penalty factor method [128, 129]. Here the need to provide continuity between the unit cells demonstrates the reasoning for a periodic representation of the contact surface. The height, H, of the solid domain was prescribed to be much greater than the surface roughness, R_q, such that no deformation of the top surface of occurred [130].

$$\boldsymbol{T}(x,t) = \int_0^t \boldsymbol{G}(t-s) \cdot \frac{D\boldsymbol{E}}{Ds}(\boldsymbol{x},s)\, ds \tag{6.5}$$

$$\boldsymbol{E} = \tfrac{1}{2}\left(\nabla \boldsymbol{u} + (\nabla \boldsymbol{u})^{\mathrm{T}} + (\nabla \boldsymbol{u})^{\mathrm{T}} (\nabla \boldsymbol{u})\right) \tag{6.6}$$

$$\nabla \cdot \boldsymbol{T} = 0,\ \boldsymbol{T}^{\mathrm{T}} = \boldsymbol{T} \tag{6.7}$$

$$\boldsymbol{u} \cdot \hat{\boldsymbol{n}} = 0 \text{ on } \Gamma_{S,sym} \tag{6.8}$$

$$\boldsymbol{T} \cdot \hat{\boldsymbol{n}} = -p_{avg} \hat{\boldsymbol{n}} \text{ on } \Gamma_{SF} \tag{6.9}$$

The fluid domain, Ω_F, was governed by Equations 6.10-6.11, which represented steady, laminar, incompressible flow with $\boldsymbol{v}$ as the velocity vector, p as pressure, and μ as viscosity. The boundary conditions in Equations 6.12-6.14 represented "no slip" on the fluid-solid interfaces [80], the prescribed pressure difference between the cell inlet and outlet, and symmetry on the remaining surfaces (Figure 6.2(b)).

$$\nabla \cdot \boldsymbol{v} = 0 \tag{6.10}$$

$$\rho(\boldsymbol{v} \cdot \nabla)\boldsymbol{v} = \nabla \cdot \left(-pI + \mu\left(\nabla \boldsymbol{v} + (\nabla \boldsymbol{v})^{\mathrm{T}}\right)\right) \tag{6.11}$$

$$\boldsymbol{v} = 0 \text{ on } \Gamma_{FS} \tag{6.12}$$

$$p_i, p_o = \text{constants on } \Gamma_{F,i}, \Gamma_{F,o} \tag{6.13}$$

$$\boldsymbol{v} \cdot \hat{\boldsymbol{n}} = 0 \text{ on } \Gamma_{F,sym} \tag{6.14}$$

Once the fluid problem was solved, the relationship between the local volumetric flow, q, and the cell's permeability, K, was calculated from Darcy's Law as seen in Equations 6.15 and 6.16.

$$q = \int_{\Gamma_{F,i}} \boldsymbol{v} \cdot \hat{\boldsymbol{n}} dS = \frac{K}{\mu}\left(\frac{p_i - p_o}{l}\right) \tag{6.15}$$

$$K\left(p_{avg}\right) = \mu\left(\frac{l}{p_i - p_o}\right)q \tag{6.16}$$

At the macro-scale (length scale of the seal, Figure 6.1(c), Darcy's Law was again employed to solve for the volumetric flow rate across the entire seal, Q in Equation 6.17, with K now a known function of pressure where L is the width of the seal and L_p is the perimeter of the seal.

$$Q = -\frac{KL_P}{\mu l}\frac{dp}{dx} = \frac{L_P}{\mu L l}\int_{p_i}^{p_o} K dp \qquad 6.17$$

The model as outlined in the above equations can be solved numerically in commercially available finite element software. Here solution of the unit cell problems was carried out in Comsol Multiphysics (Version 4.3a, Stockholm, Sweden) with post-processing in MATLAB (R2009a, Natick, MA, USA).

6.3 Materials and Methods

6.3.1 Contact Surface Topology

The contact surfaces studied were water-proof, 240 grit silicon carbide grinding paper (Allied High Tech Products, Rancho Dominguez, CA, USA) and the denticle surface of a Short Fin Mako Shark (*Isurus oxyrinchus*). The roughness, R_q, and wavelength, l, components of the contact surfaces were obtained from their power spectrums as computed by the Fast Fourier Transform techniques in [109] using surface height data obtained from an Olympus LEXT 3D Material Confocal Microscope (Center Valley, PA, USA).

6.3.2 Viscoelastic Seal Characterization

For validation, although the multi-scale model was conceived with biological applications in mind, a commercially available urethane elastomer (ReoFlex 30, Smooth-On Inc. Easton, PA, USA) rather than natural tissues was employed. This afforded several benefits with respect to reducing the uncertainty in material properties including guaranteed homogeneity, reduced dependence on hydration levels, and no confounding due to lack of homeostasis which are frequently cited as difficulties in working with

biological tissues [26, 57, 59, 61, 64, 65, 122-124]. Furthermore, idealized geometries were also easily formed using an engineered material. Both relaxation test specimens and seals used in the permeability experiments on grinding paper were constructed by hand-mixing the two part urethane compound and casting the mixture into molds. The castings were allowed 48 hours to harden such that their full mechanical properties were obtained. Stress relaxation tests were carried out at room temperature (20°C) in accordance with ASTM D6048 [131] on three independently prepared 15 x 3.25 x 130 mm specimens using an ESM301 test frame equipped with an M5-20 force gauge (Mark-10, Copiague, NY, USA). Equation 6.4 was then fit to the data in a least squared sense.

Characterization of remora fleshy lip tissue was carried out with uniaxial dynamic mechanical analysis (DMA) where periodic compression was applied at different frequencies with fixed strain amplitude [26]. DMA was performed on 7 mm^3 sections of tissue from the posterior region on the fleshy lip of an *Echeneis naucrates* specimen. Testing was carried out within 1 hour of specimen euthanization. Euthanization was accomplished with 0.5 g/L dose of MS-222 (tricaine methanesulphonate). Equation 6.4 was fit to the data in a least squared sense, and the tissue was assumed to be nearly incompressible [57]. With respect to the host surface, shark dermal denticles are in part made up of a hard enamel-like materials whose mechanical properties are similar to shark teeth [132]. Because the stiffness of the dermal denticles [133, 134] is several orders of magnitude higher than that of remora soft tissue, the dermal denticles are considered rigid.

Concerning the differences in testing methods, broadly speaking, relaxation tests are more suitable for observing material behavior at long time scales ($>10^1$ s) whereas

DMA is more convenient for shorter time scales (10^{-10} to 10^{5} s) [60], though there is an appreciable region of overlap between the two.

6.3.3 Model Validation and Simulations

Validation of the interfacial permeability model was carried out using the experimental setup in Figure 6.3. The apparatus was designed to measure both the flow rate and sub-ambient pressure difference across the seal in contact with a rough surface to be comparable with model predictions. At the base of the device (Figure 6.3), a custom annular viscoelastic seal (ReoFlex 30 urethane rubber) with a 5x5 mm square cross section (L) and diameter of 45 mm (L_p ~14.1 cm) was bonded to a rigid member using epoxy. The member was adjusted via a threaded connection and electrical conductivity measurements such that the base of the seal was precisely flush with the base of the center tubing. This was to ensure that deformation of the seal was only due to movement of the fluid (water) across the interface and not due to compression of the seal by the reduced pressure under the member. Once aligned, the base of the center tube and seal were brought into contact with the rough substrate (240 grit grinding paper) and the vacuum source was activated along with a peristaltic pump that maintained a constant fluid height (pressure head) above the substrate. After steady state was achieved, the pressure difference across the seal was measured with an electronic pressure transducer (Cole-Parmer Instrument Company Model 68075, Vernon Hills, IL, USA) and the flow rate was calculated using a graduated cylinder and stopwatch. The flow rate at several sub-ambient pressure differences spanning 0 to 20 kPa were obtained by manually adjusting the vacuum source with a pressure regulator. For comparison, the interfacial permeability model was solved over a sub-ambient pressure range of 1 Pa to 100 kPa

using the properties of water at room temperature (20°C) in addition to the measured material properties of the viscoelastic seal and the topology of the rough substrate.

With respect to the remora on shark skin, the interfacial permeability model was solved over a sub-ambient pressure range of 1 to 300 Pa using the properties of water at room temperature (20°C). The perimeter of the remora pad was assumed to be 100 mm with a seal thickness of 3 mm. These values correspond to a remora approximately 19 cm in length as was observed when attached to a glass slide [26]. Additionally, the model was used to predict the flow rate into the remora pad over a range of surface roughness values from 1 to 100 μm and over a range of pressures from 1 to 10^5 Pa.

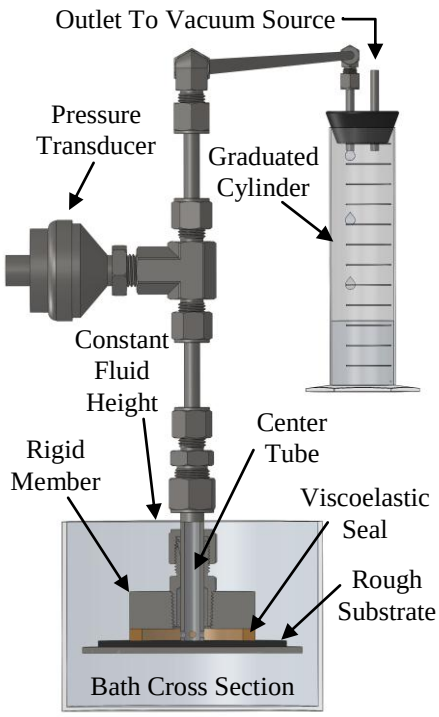

Figure 6.3: Interfacial permeability measurement system

6.4 Results

6.4.1 Contact Surface Topology

The power spectrum of the rough substrate (240 grit grinding paper) is seen in Figure 6.4. The root mean square roughness, R_q, and cutoff wavelength, l, needed to characterize the surface in the multi-scaled model were 34.8 and 318 μm, respectively. The appropriateness of the contact surface simplification is reinforced by the exponential decay of the power spectrum, as from [109] it is known that the roughness of such surfaces is dominated by the cutoff wavelength as others fall off rapidly. Also, the ratio of the length of the seal, L (5 mm), to the cutoff wavelength, l, was approximately 16, meaning that the size of the unit cell was an order of magnitude smaller than the size of the seal, making the multi-scaled approach possible.

The power spectrum of the Short Fin Mako Shark denticle surface can be seen in Figure 6.5. The root mean square roughness was 10.5 μm, and the cutoff wavelength, computed at the intersection of the power and horizontal fits, was 200 μm. The cutoff wavelength correlated closely to denticle dimensions and spacing found in [21, 116]. The ratio of seal length (3 mm) to unit cell length (200 μm) was approximately 15, rendering the multi-scaled model approach applicable.

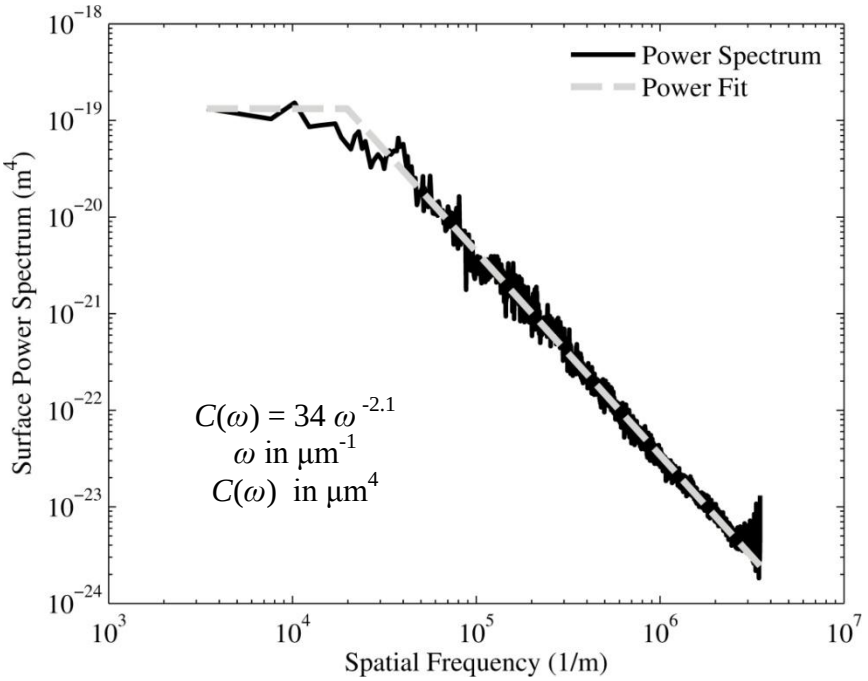

Figure 6.4: Power spectrum of rough surface (240 grit grinding paper) used in experimental permeability apparatus shown with linear fit. R_q and cutoff wavelength were 34.8 and 318 μm

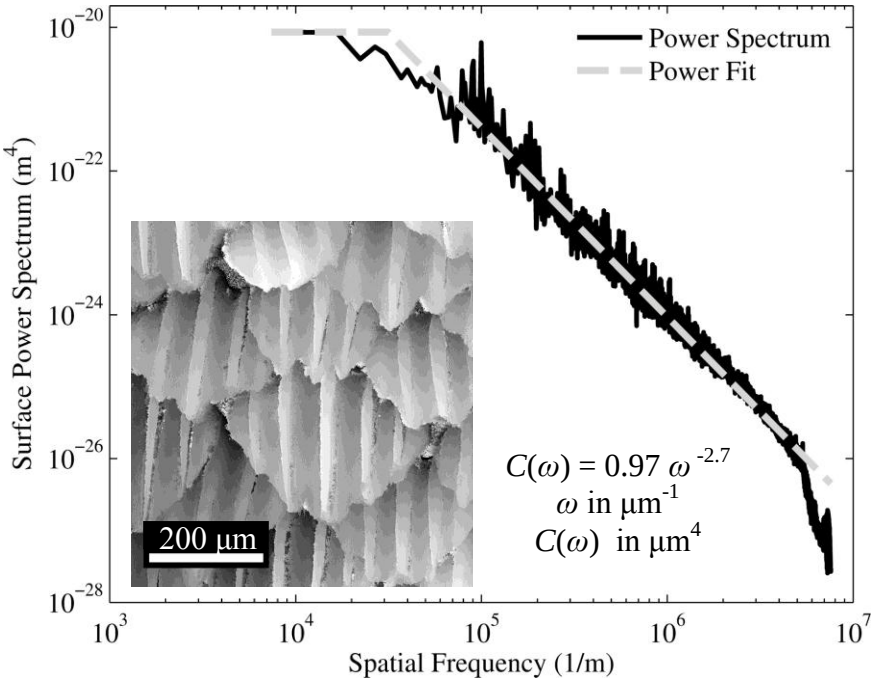

Figure 6.5: Short Fin Mako denticle 16 bit height map (inset) and resulting power spectrum with linear fitting parameters. R_q and cutoff wavelength were 10.5 and 200 μm

6.4.2 Seal Viscoelastic Properties

The relaxation moduli and resulting Maxwell Material Model parameters are shown in Table 6.1. Figure 6.6 shows relaxation tests performed on the urethane rubber seal. As expected, the modulus monotonically decreased with increasing time [60]. The leading order term (Young's Modulus) of the Maxwell Model was slightly lower than that expected for a rubber with a 30A Shore durometer (~1 MPa [135]); however, the results were consistent among independently prepared samples as there was negligible deviation (<5%) from the values in Table 6.1.

Table 6.1: Average Maxwell Model fitting parameters for urethane rubber (ReoFlex 30) and remora fleshy lip tissue

Material	Property	Maxwell Element			Young's Modulus (kPa)	Poisson's Ratio
		1st	2nd	3rd		
Urethane Rubber (ReoFlex 30)	k (kPa)	49.00	57.05	46.14	277.4	0.495
	τ (s)	197.8	2.175	20.25		
Remora Tissue	k (Pa)	0.860	2.70	0.700	3.980	0.495
	τ (s)	0.11	0.016	0.68		

The measured storage and loss moduli from DMA tests on remora soft tissue can be seen in Figure 6.7. The viscoelastic properties indicate that the remora's fleshy lip is very compliant, and capable of dissipating energy since the loss modulus is of similar magnitude to the storage modulus.

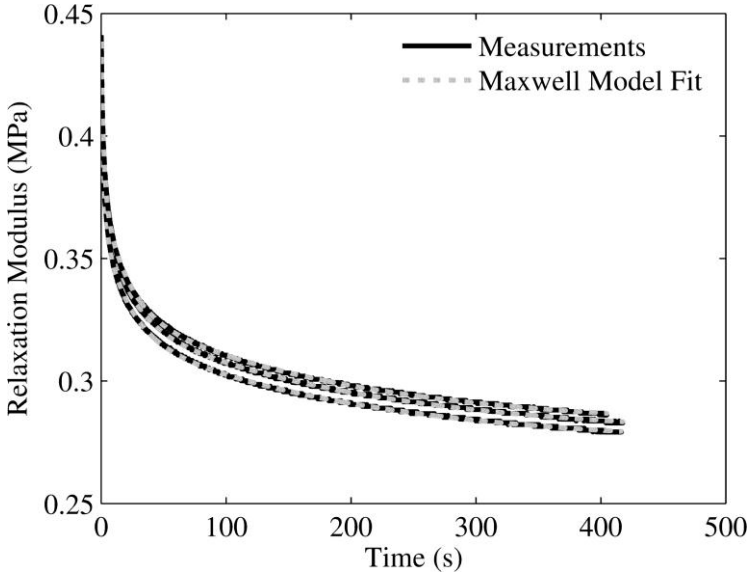

Figure 6.6: Relaxation tests on urethane rubber used in experimental permeability apparatus with accompanying Maxwell Material Model

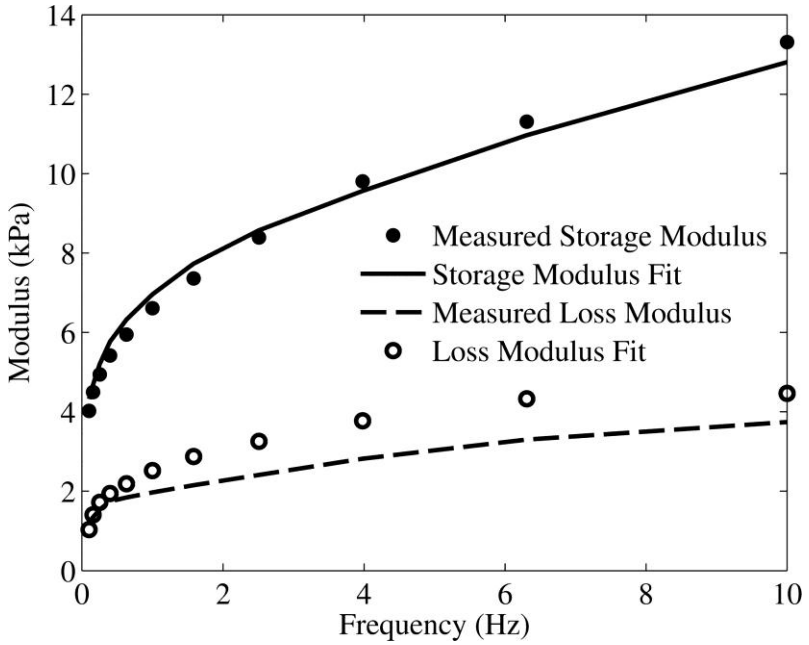

Figure 6.7: DMA test on remora soft tissue showing storage and loss moduli, and fitted Maxwell model parameters

6.4.3 Model Results and Validation

Regarding urethane rubber on grinding paper, the displacement field magnitude resulting from solution of the solid mechanics unit cell problem at 10 kPa sub-ambient

pressure is shown in Figure 6.8(a). Looking at the deformed configuration, it is possible to see how the soft rubber was displaced into the rough contact surface, and also how the deformed fluid domain was obtained from the space between. Figure 6.8(b) shows the velocity field magnitude corresponding to solution of the fluid mechanics unit cell problem at 10 kPa sub-ambient pressure with a prescribed pressure difference of 10 Pa across the unit cell (equal to a pressure gradient of 3.2×10^{-2} kPa/mm). Using the velocity field and Equations 6.15 and 6.16, the permeability of the deformed cell was calculated at different pressure gradients (Figure 6.8). It can be seen that the permeability of the deformed cell was constant below approximately 10 kPa/mm.

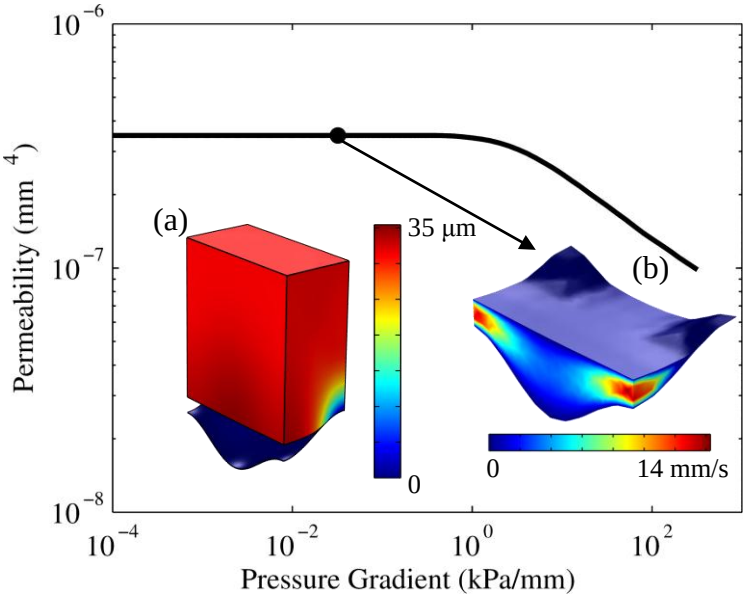

Figure 6.8: Cell permeability at 10 kPa sub-ambient pressure vs. pressure gradient; and corresponding (a) solid domain displacement magnitude and (b**)** fluid domain velocity magnitude

Repeated solution of the cell problems over a sub-ambient pressure range spanning 1 Pa to 100 kPa in the urethane rubber case and 1 to 300 Pa in the case of the

remora on shark skin resulted in their respective pressure dependent interfacial permeabilities, K (Figure 6.9). In both cases, at low sub-ambient pressures the permeability achieved its largest value and remained nearly constant, but as the sub-ambient pressure gradually increased, the permeability began to fall rapidly after approximately 1 kPa for the urethane rubber on grinding paper and 30 Pa for the remora tissue on shark skin. Integration of the permeabilities using Equation 6.17 yielded estimates of the expected flow rates across the seals. The expected flow rate of the urethane seal against grinding paper for sub-ambient pressure differentials ranging between 0 and 20 kPa is shown in Figure 6.10 along with flow rate measurements made on the permeability test apparatus. Similarly, the expected flow rate into the remora's dorsal pad during attachment to shark skin at sub-ambient pressure differentials from 0 to 300 Pa is shown in Figure 6.11. In both cases flow rates increased at a decreasing rate with respect to increasing sub-ambient pressure differences. Furthermore, in the case of the urethane seal, reasonable agreement was obtained between the predicted and measured values.

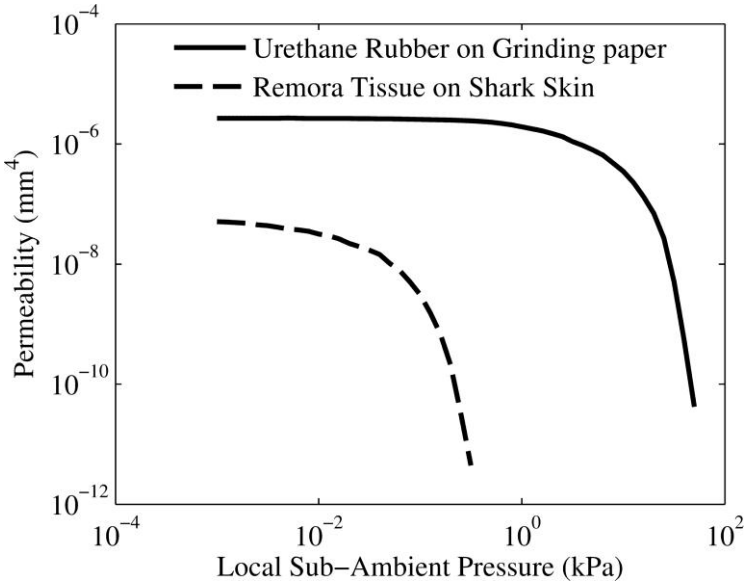

Figure 6.9: Permeability of the urethane seal on grinding paper and remora tissue on shark skin with respect to local sub-ambient pressure

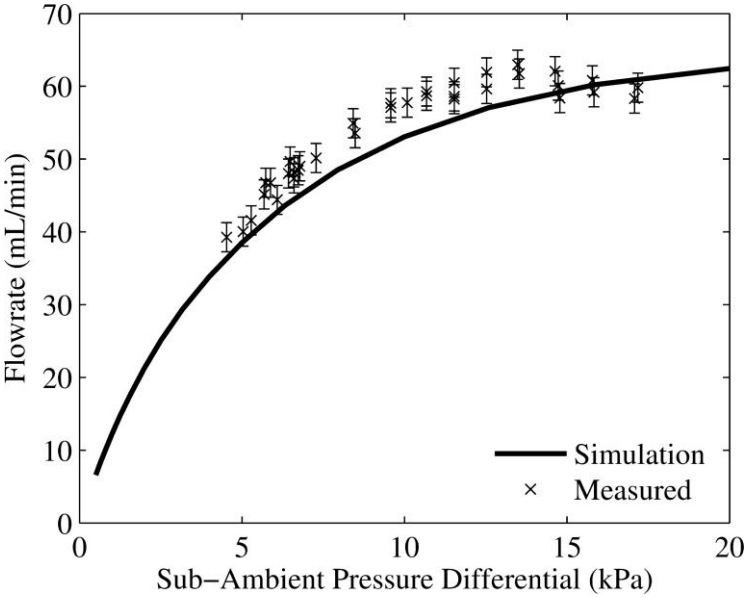

Figure 6.10: Model simulation results and flow rate tests using experimental permeability apparatus

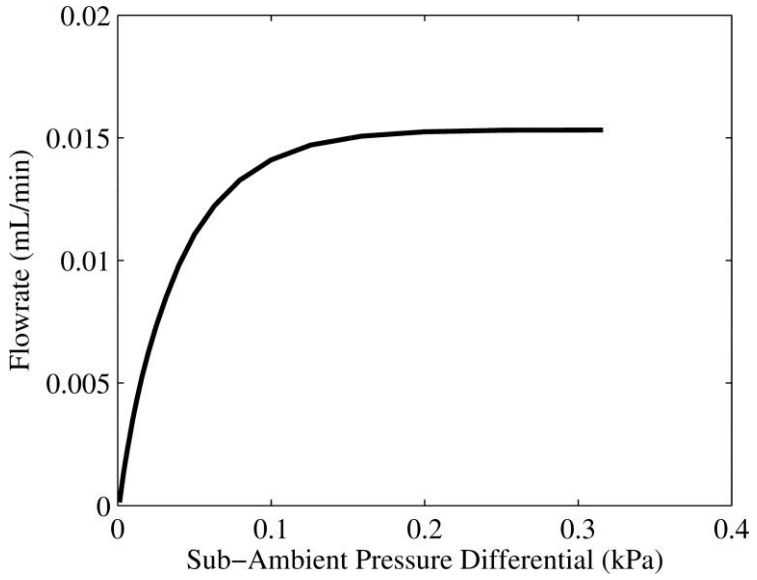

Figure 6.11: Model simulation results for flow rate of water into remora pad with respect to the sub-ambient pressure differential

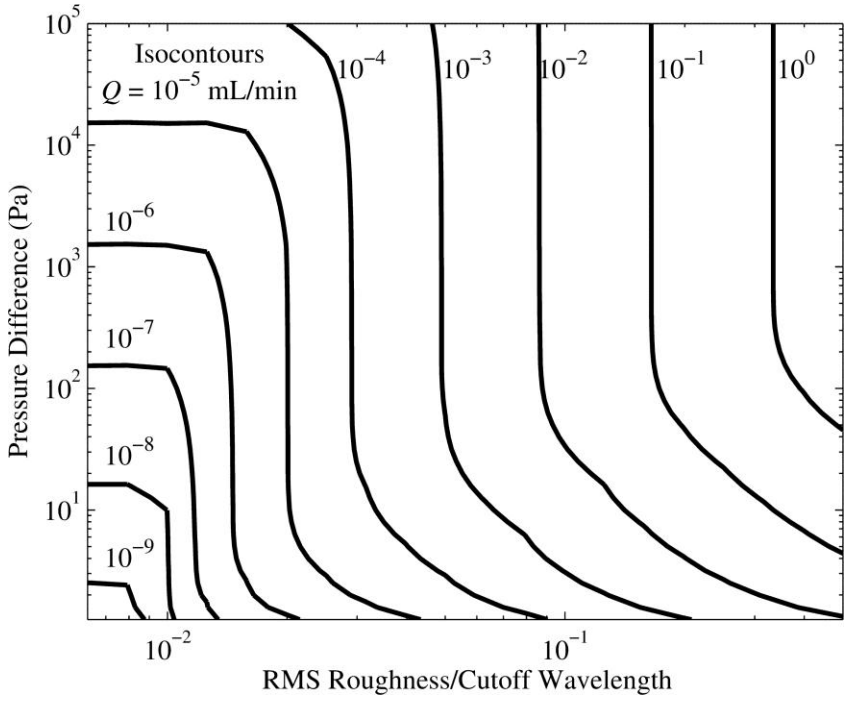

Figure 6.12: Contour plot of volumetric flow rate, Q (mL/min), vs. seal pressure difference and normalized surface roughness

Figure 6.12 expands on the results shown in Figure 6.11 showing flow rate into the remora pad over an increased range of pressure differences and host topologies (unit cell dimensions). The figure shows that either increasing the root mean square roughness of the host surface or decreasing the cutoff wavelength has the effect of increasing the flow rate into the pad.

6.5 Discussion

One use for the model described is to predict flow rates under difficult measurement conditions. Looking specifically at the flow rates developed in the remora (Figure 6.11), they are seen to be quite small (approximately 10^{-3} mL/min) even at the higher end sub-ambient pressures investigated, which is a testament to the effectiveness of the remora's seal and certainly important for prolonged attachment. However, low flow rates require increased observation time to obtain high-resolution data. When working with live animals, complications may arise from seal movement either from the natural respiration of the animal [39] or due to the animal's desire to change position [40]. In such cases, the model presented enables quantification of low flow rates from pressure measurements (in addition to known material and topological properties), which are commonly made [23, 37, 39, 40] and do not require extended observation times.

More generally, there are several important biological implications that can be drawn from the model. First, the model presented provides some explanation as to how a cutaneous mucus layer could significantly improve an organism's sealing effectiveness, and, therefore, provide an important contribution to a suction-based attachment strategy. Many marine animals, including remoras [22], are known to secrete mucus with unique properties [33, 34]. Looking at Equation 6.17 one can see the advantage of a mucus that

increases the viscosity of the surrounding fluid environment, as this reduces fluid flow across the seal. Measurement of mucus secretions from salmonids (teleost fish, as are remora) has shown significant increases in viscosity by as much as 5 to 10 times that of clean water [136]. Such increases in fluid viscosity should have a strong impact on sealing effectiveness.

In addition to viscous effects, Equation 6.17 shows several geometric parameters of the seal that can linearly alter the flow rate including widening the seal and reducing its perimeter. Both of these parameters relate to the overall attachment structure of the organism and may be more or less fixed at a particular stage of development. In that case, such parameters could have important ramifications for the organisms' growth; for instance, they could play an important role in predicting the stage of maturity when attachment structures become active or effective. Alternatively, if the organism can exert some control over these parameters, they may provide a means to actively resist detachment.

Figure 6.12 shows that even if the viscous effects of remora mucus are not considered, very low flow rates into the pad result. This demonstrates that the remora lip provides an excellent seal against surfaces with roughness comparable to that of shark skin, even when the applied pressure difference is ~1 atm. This behavior is expected as remoras are known to attach to sharks as hosts. Furthermore, such a low flow rate supports the authors claims in [23], that detachment of the remora from sharkskin resulting from large externally applied posterior loading is caused by cavitation of the water in the pad, and not due to leakage across the seal. However, the effects of increasing surface roughness can be quite severe, as a single order of magnitude increase

in surface roughness results in approximately three orders of magnitude increase in flow rate. This is because the deformation of the lip is finite and therefore at elevated surface roughness the fluid channels that form across the lip are too large to support attachment.

To the extent that material properties play a role in improving the seal, the model demonstrates the advantage of having softer more conformal tissues at the sealing interface. Figure 6.9 shows a dramatic drop in the permeability of the interface at increasing sub-ambient pressures beyond approximately 1 kPa for the urethane rubber on grinding paper and 30 Pa for the remora tissue on shark skin. This is a result of the sealing material being drawn into the rough substrate and restricting flow as seen in Figure 6.8(a). Since deformation of the seal is directly proportional to its stiffness from Equation 6.5, it follows that the onset of the drop in permeability, and therefore reduced flow rates over an increased pressure range, will occur at lower sub-ambient pressures for softer vs. harder sealing materials. From a biological perspective, this translates into reduced leakage, which is important for prolonged suction-based attachment.

Regarding topology, although the simplified contact surface given by the parameterization in Equations 6.1-6.3 was implemented, other surfaces that possess the translational periodicity required for the multi-scaled approach could be employed. The simplified contact surface is convenient as it can be informed by power spectrum data that decays exponentially (Figure 6.4). However, other surfaces including fracture surfaces, surfaces prepared by bombardment with small particles (sediment), or surfaces resulting from repeating units like scales or denticles are also valid [26]. In such cases where a description of the local topology is desired that goes beyond the simplified representation, the unit cell can be expanded to capture the periodic features of the

topology, as long as it remains much smaller than the size of the seal ($l<<L$ section 6.2.3). Thus, although the nature of the topology under scrutiny should be considered carefully as it plays an important role in the applicability of the model, periodicity (or at least the approximation of periodicity) is a manageable requirement.

From a solid mechanics perspective, the multi-scaled approach offers flexibility in terms of constitutive properties and seal geometry. For example, the choice of constitutive behavior is not limited to the Maxwell Model employed in Equation 6.4. Indeed, any constitutive model, including the even more simplified linear elastic model, compatible with the boundary conditions and implementable in a finite element formulation could be imposed. Furthermore, although seal homogeneity was assumed, more complex local material structures (such as layers or inclusions) could be incorporated to provide a more accurate representation of the sealing interface, as long as the structures possess the requisite periodicity needed for continuity of the unit cell. In light of previous discussion, a layered approach to forming a seal with decreasing stiffness as the interface is approached could be an interesting and attractive means for improving sealing effectiveness while also maintaining strength. Such a structure could be achieved by continuously changing the composition of the sealing material or by bonding layers of decreasing stiffness. However, as constitutive models or structures become more complex often the devices needed to obtain material data similarly become more complex [57, 60] or simulation time increases dramatically. Furthermore, in the case of living tissues, it could be argued that the variance between specimens and in some cases within the same specimen is too great to be considered useful or homogeneous. In

such cases, at the very least, the model could provide a first-order estimate of seal behavior.

From a fluid mechanics perspective, one limitation of the approach is that Darcy's Law breaks down at large flow rates across the seal (i.e. when the Reynolds Number > 1 [126]). This occurs, for example, when the pressure gradient across the cell becomes large as seen in Figure 6.8 when the permeability is no longer a constant. Fortunately, in applications with small length scales where minimizing the flow rate is desirable, such as the present case, one is not interested in large flow rates. For example, the suction pressure differentials measured in remora attached to shark skin are reported as 0.5 kPa on a host at rest [23] which falls well within the range of the model presented here [26]. Of more concern is that Darcy's Law is not valid when significant non-Newtonian fluid behavior is induced, and thus care must be taken when applying the Newtonian assumption to a particular system.

With respect to solution time, although simplicity was sought to minimize computation, the model may still require a significant amount of time to complete because the cell problems must be solved at each prescribed local pressure. Though this difficulty is incumbent upon the multi-scaled formulation, it is tempered by the ability to separate the solid and fluid mechanics problems, which is advantageous when considering the challenges associated with solving fully coupled fluid-structure interaction problems.

Lastly, concerning broader estimates of suction-based attachment such as time to failure, although the importance of the seal has been demonstrated in the context of the length scales presented, as in Figure 6.1(c) and (d), it is also important to consider the

configuration and material properties of the attachment structure itself, as in Figure 6.1(a) and (b), because it is at the length scale of these structures that the sub-ambient pressure is created. Thus, to characterize attachment failure due to seal leakage, in addition to information about the seal as presented here, knowledge of the suction cavity volume change with respect to pressure is also required, which is unique to the species under consideration.

6.6 Conclusion

When considering the bottom-up, multi-scaled approach taken here, one can see how the model presented is not limited to a particular species in terms of its application. Rather, the basic geometric, material, fluid, and topological properties of the materials and structures involved drive the analysis. In turn, this approach could be applied to a variety of organismal systems by introducing biological values for a particular organism to predict the sealing effectiveness of an organism without large amounts of ad-hoc empirical data. Similarly, the model can be used as a quantitative tool to guide design efforts in translating biological sealing performance to engineered devices, as was demonstrated with the validation apparatus.

The reversible adhesion observed in many marine organisms both has and will continue to serve as inspiration for many useful suction-based grasping devices. Quantifying not only the maximum strength of attachment but also an organisms' ability to create an effective seal is important not only from a biological perspective toward understanding and quantifying suction-based adhesion behavior, but also for engineers in translating such behavior into useful devices. The theoretical framework developed in this work demonstrates how the material properties of the sealing structures and fluids

combined with the topology of the attachment site are crucial parameters in determining long-term attachment performance. Although the framework was demonstrated using an artificial apparatus, the methods used are appropriate for biological applications as was illustrated in the case of the remora fish. Therefore, future work may be aimed at both evaluating organism and/or device performance based on the outlined techniques.

CHAPTER 7

Time Scale and Operational Limits of Remora Adhesion

7.1 Introduction

Remora fishes (family Echeneidae) are known for their ability to create reversible suction-based attachment to a wide variety of both naturally occurring and manmade marine surfaces [7-13, 72]. This ability allows remoras to "hitchhike" on their hosts and provides several benefits including reduced metabolic demands [107], increased access to food [13], protection from predators [2], and increased courtship potential [72]. While some hosts may benefit from remora hitchhiking in the form of parasite removal [7], all hosts must expend extra energy during locomotion to compensate for the parasitic drag incurred perhaps by multiple remoras. In both cases the benefits or costs of remora attachment are realized over prolonged periods (weeks) [72]. Despite the realization that prolonged adhesion is beneficial to the remora, there have been no investigations seeking quantitative predictions as to the length of time a remora can remain attached to its host. Here a bottom-up approach that considers the many facets of remora adhesion is presented to provide such an estimate.

Remoras create adhesion with a modified dorsal pad shown in Figure 7.1. The key structural features of the pad include (a) the fleshy lip surrounding the pad's perimeter, (b) an array of pectinated lamella, and (c) thousands of small spinules that project from the lamella. Several investigations as to the purpose and operations of each feature have been performed and are discussed below.

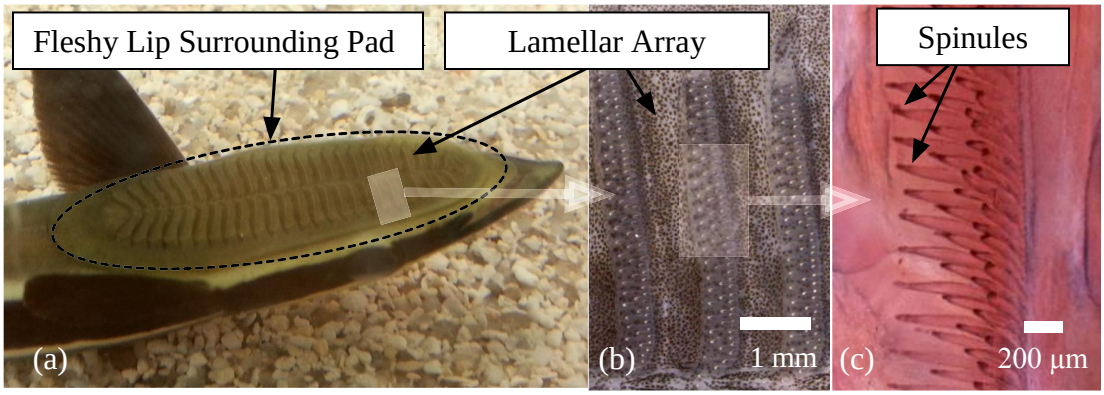

Figure 7.1: The suction disk of the remora (*Echeneis naucrates*). (a) Dorsal view of the remora. (b) Close-up view of lamellar array in disk. (c) Optical microscope image of projecting lamella.

In general, the key requirement for any suction based attachment strategy is the ability to maintain a sub-ambient pressure difference with respect to the surrounding environment [3]. By necessity this requires a robust seal that divides the two regions, and in remoras, this is primarily accomplished by a fleshy lip that is made of soft tissue [21, 22, 26]. Creating a water tight seal in a natural environment is challenging for many reasons including surface contamination from particulate/bio-fouling and surface topology (roughness/waviness) [51]. Furthermore, once a seal is achieved, it is known from theoretical considerations and experiments that if the fleshy lip is breached or if surface topology is too rough to prevent leakage, then attachment will be compromised [22, 26, 137].

In addition to sealing, another key requirement for remora attachment is the ability to resist drag forces caused by host locomotion that would otherwise sweep the remora from its attachment site. A remora resists drag forces by creating friction against its host using an array of pectinated lamellae and spinules found throughout the dorsal

pad. The lamellae are formed by both mineralized and soft tissues [20]. They are capable of removing nearly all the fluid from the pad, and responsible for delivering thousands of spinules to the host surface [21, 27]. Spinules are small posterior-directed, mineralized tissue that project from the lamellae [20]. Both theory and experiments show that spinules dramatically enhance friction between the remora and its host thereby preventing slippage [21, 23, 55].

Often work investigating biological adhesion is focused on the maximum force an organism or an organism's attachment structure can endure before adhesion is lost [23, 37, 39]. While this does provide crucial information necessary for understanding the limits of attachment with respect to large, disruptive forces, it is not indicative of the attachment conditions that are present during more routine, less extreme conditions [40]. Concerning the remora, Figure 7.2 shows several rapid adhesive failure mechanisms that can occur including (a) an external breach of the fleshy lip seal, (b) large shearing forces greater than the friction force the remora can create, and (c) cavitation of fluid inside the pad (formation of gas phase due to reduced fluid pressure) [23, 137]. Observation of both captive and wild remora show that hosts are rarely successful at dislodging remora unless extraordinary measures are employed, usually involving extreme body bending or collision of the remora with ocean's floor or surface which could be viewed as a combination of the aforementioned mechanisms [8, 9, 12, 17]. Such measures are required in part due to the remora's streamlined shape, as drag estimates have shown that it is unlikely to be removed by elevated host swimming speeds alone. In contrast to previous work, here attachment failure under more moderate conditions is investigated.

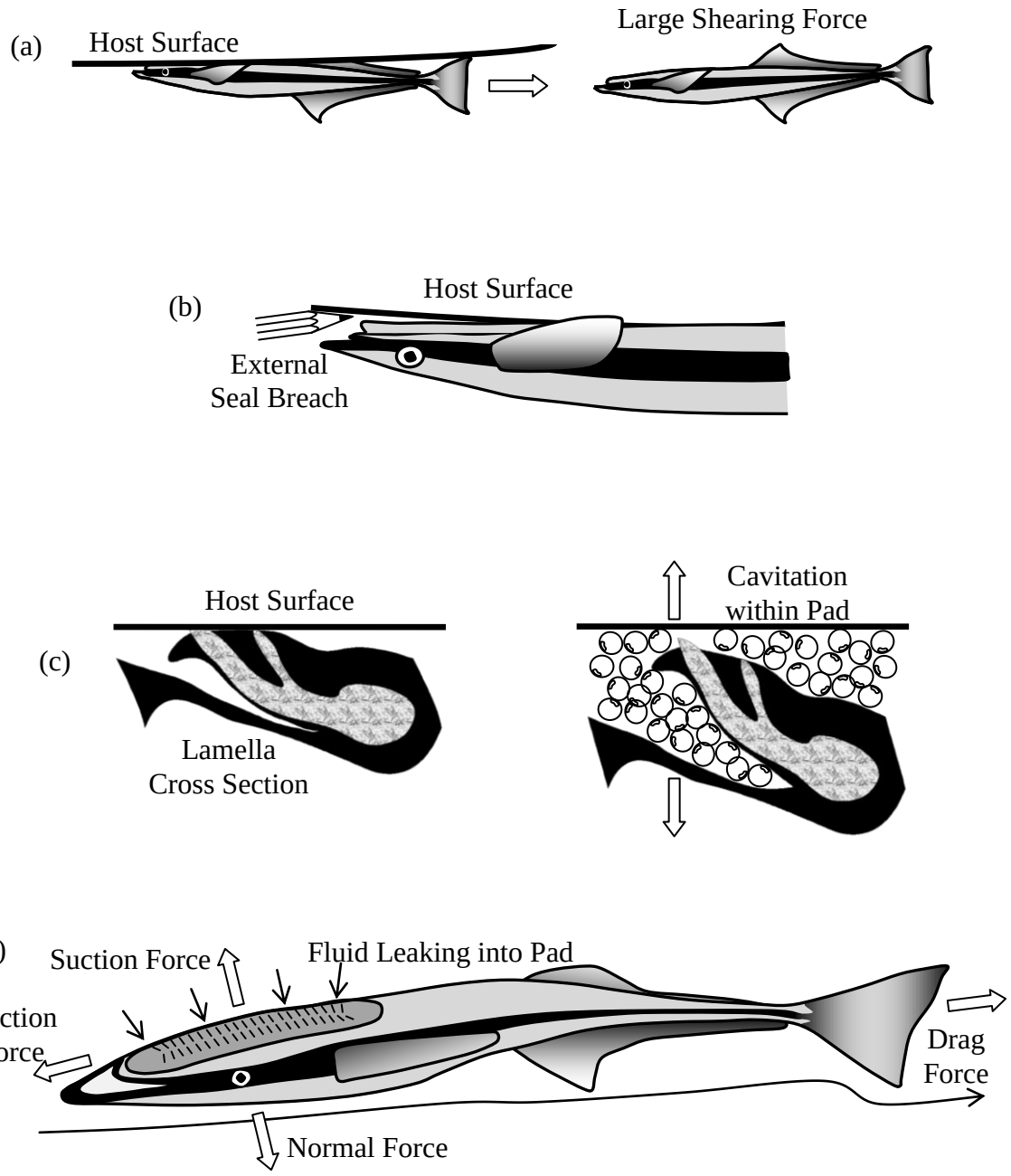

Figure 7.2: Rapid remora attachment failure mechanisms: (a) large shearing force, (b) external seal breach, and (c) fluid cavitation within pad; (d) gradual attachment failure by seal leakage and loss of friction.

Expanding on Figure 7.2(d), the forces acting on an attached remora can be expressed as a free body diagram as seen in Figure 7.3 where the drag, $\vec{F}_D$, and friction, $\vec{F}_F$, forces act along the *x*-axis and the normal, $\vec{F}_N$, and suction, $\vec{F}_S$, forces act along the *y*-axis. The magnitude of the forces are governed by the drag coefficient (C_D), density of the surrounding fluid (ρ), remora's wetted area (A), host speed (U), sub-ambient pressure inside the pad with respect to the environment (P), pad area (A_{pad}), and friction coefficient (μ_s) between the remora and host.

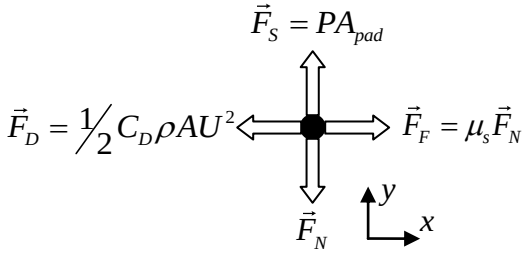

Figure 7.3: Free body diagram of remora on host swimming in positive *x*-axis direction

The free body diagram illustrates two related hazards to remora attachment: loss of suction and/or loss of friction. In the case of perfect sealing and large suction forces, low friction causes a remora to be swept away by drag forces, and in the case of infinite friction and no suction, the remora will float off its host. The following section treats remora adhesive failure as occurring gradually through a combination of both imperfect sealing and friction. The treatment assumes a remora can tolerate a finite fluid volume in its pad that occurs due to leakage across the fleshy lip seal. As fluid from the surroundings fills the pad, the pressure inside the pad begins to equalize with its surroundings. Eventually, a critical pressure is reached such that friction is no longer

sufficient to resist the drag forces imposed by host locomotion, and the remora losses traction on its host (attachment failure). The analysis considers all previously discussed aspects of a remora's dorsal pad (fleshy lip, lamellae, spinules), the drag forces imposed on the remora by host locomotion, and the topology of the attachment site.

7.2 Materials and Methods

In this chapter, gradual fluid leakage into a remora's (*Echeneis naucrates*) dorsal pad and loss of friction are investigated as the cause of attachment failure. For reference, the parameter values used throughout the analysis are shown in Table 7.1, and are based on scaling relationships and measurements from previous chapters.

Table 7.1: Remora Failure Analysis Parameters

Name	Variable	Value	Units
Length	L	39.5	cm
Area of Pad	A_{pad}	22	cm^2
Wetted Area	A	260	cm^2
Pad Perimeter	L_p	21	cm
Seal Width	W	3	mm
Lamellar Pairs	N	21	-
Average Lamellar Length	L_l	12.3	mm
Drag Coefficient	C_D	0.0045	-
Water Density	ρ	1000	kg/m^3
Water Viscosity	μ_w	0.001	Pa-s
Mucus Viscosity	μ_m	0.005	Pa-s
Host Speed	U	0.65	m/s
Friction Coefficient	μ_s	0.22	-

From conservation of mass, the volumetric fluid flow into the pad, Q, is balanced by an increase in the fluid volume, V, stored in the pad when the fluid is incompressible. This is shown in Equation 7.1 where the chain-rule has been employed to include the sub-ambient pressure inside of the dorsal pad with respect to the environment.

$$Qdt = dV = \frac{dV}{dP} dP \tag{7.1}$$

Under quasi-static conditions (i.e. occurring gradually over time, t), Equation 7.1 can be rearranged and integrated from the initial, P_0, to the failure pressure, P_f, to find the attachment time, t_f, as in Equation 7.2.

$$t_f = \int_{P_0}^{P_f} \frac{1}{Q} \frac{dV}{dP} dP \tag{7.2}$$

Equation 7.2 is an important relationship that clearly outlines the quantities needed to estimate the attachment time, namely the dependence of fluid flow into the pad with respect to pressure, the change in volume of the attachment structure with respect to pressure, and the pressure limits for integration.

The investigation begins by evaluating the failure pressure, P_f, at which attachment is compromised. While it may be tempting take this as zero (gauge pressure), which would represent pressure equilibrium with the surrounding environment, in its natural environment remoras must resist slippage caused by drag forces to maintain adhesion to a moving host. The creation of frictional forces implies that P_f is greater than zero such that a normal force exists between the remora and its host. On rough surfaces such as shark skin, remoras use their spinules to create friction [21, 23, 55]. Hence, to determine the failure pressure that occurs at the onset of slippage, Equation 7.3 was derived by balancing the forces in Figure 7.3.

$$P_f = \frac{1/2 C_D \rho U^2 A}{\mu_s A_{pad}} \tag{7.3}$$

The values used for Equation 7.3 are shown in Table 7.1, and are representative of attachment to a shark moving at migratory speeds. Plugging in values from the table provided a failure pressure of approximately 51 Pa.

Next, fluid flow into the pad, *Q*, is considered. The primary suction seal of the remora is created by a perimeter of soft tissue known as the fleshy lip [21]. A model for the sealing effectiveness of suction based seals in marine organisms was presented in CHAPTER 6. The model estimates the flow rate across suction seals by considering the local topology of the attachment surface, the geometric properties of the seal, and the viscoelastic properties of the tissues forming the seal. Solutions of the model specifically pertaining to remora attachment on different surface configurations are presented in [26]. Here a surrogate model, Equation 7.4, was fit to simulation results specifically relevant to the denticle surface of a Mako shark (*Isurus oxyrinchus*). The parameters α and β were fit to numerical results in a least squared sense with μ_m as the viscosity of the fluid at the sealing interface, W as the width of the suction seal, and L_p as the perimeter of the dorsal pad. Equation 7.4 provided the first term in the integral of Equation 7.2.

$$Q(P) = \frac{\alpha L_p}{\mu_m W}\left(1 - \exp\left(-\beta P\right)\right) \tag{7.4}$$

From [22] it is known that remora secrete copious amounts of mucus onto their attachment surface, and therefore the viscosity of the interface was estimated as five times that of the surrounding environment based on measurements from other teleost fish mucus [136]. The width of the suction seal was estimated by pressing a euthanized specimen against a glass slide and measuring it directly [26].

Moving to the second term in the integral of Equation 7.2, the structural response of the dorsal pad (change in volume) with respect to changes in pressure is considered.

The majority of the dorsal pad structure is formed by an array of pectinated lamella which the remora can articulate by means of muscle contractions [20, 21]. An estimate of the lamellar response to loading using actual remora geometry obtained from μCT and the material properties of euthanized remora tissue was obtained from [27]. The study provided the change in fluid volume within a lamellar compartment with respect to load, but here the data was converted to pressure using the number of lamella, N, average lamellar length, L_l, and the pad area shown in Table 7.1. The results from that study were represented by the piecewise continuous function given by Equation 7.5 and Table 7.2 (Figure 7.4) where volume is given in mm^3 and pressure in Pa. Differentiation of Equation 7.5 provided the second term for the integral in Equation 7.2. Furthermore, by plugging in the pad pressure at failure, the fluid volume at failure, V_f, was computed as 31.9 mm^3.

Table 7.2: Coefficients for Equation 7.5

Variable	Value	Units
c_1	51.62	mm3
c_2	-0.213	mm^3/Pa
c_3	8.056×10^{-3}	1/Pa
c_4	-7.646×10^{-5}	mm^3
c_5	0.2072	1/Pa
c_6	9.168×10^{-2}	mm^3/Pa
c_7	179	Pa

$$V(P)=\begin{cases} c_1+c_2P\exp(c_3P)+c_4\exp(c_5P), & 0\le P<60.2 \\ c_6(c_7-P), & 60.2\le P<179 \\ 0, & 179\le P \end{cases} \qquad 7.5$$

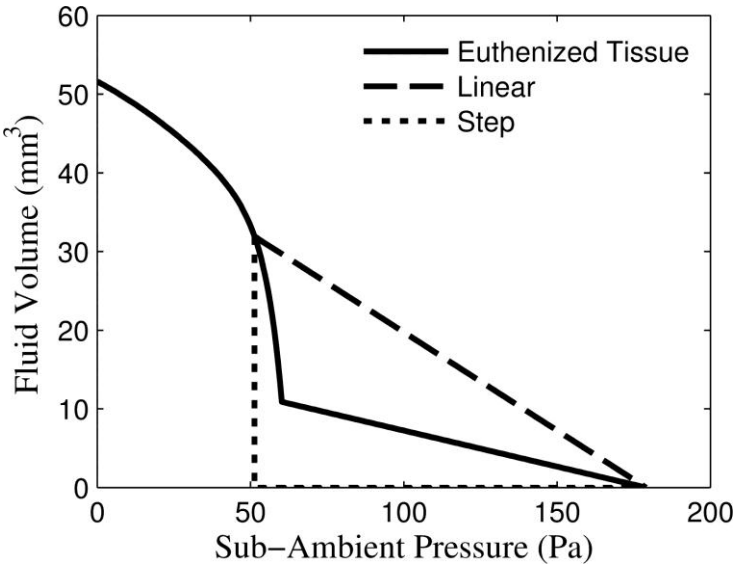

Figure 7.4: Change in fluid volume of the lamellar compartments with respect to pressure

Two additional cases of lamellar deformation were considered to provide a basis for comparison including the linear and step responses seen in Figure 7.4. The linear relationship between pressure (Pa) and volume (mm^3) that was employed is given by Equation 7.6, which was constructed such that its ends coincided with the end points of the actual lamellar response at full compression and the failure pressure as seen in Figure 7.4. The slope of the fit was used in the second term of the integral in Equation 7.2.

$$V(P)=\begin{cases}0.250(179-P), 51<P\le 179\\ 0, 179<P\end{cases} \qquad 7.6$$

The step response appears in Figure 7.4 as a horizontal line along the pressure axis that rapidly jumps to V_f at the failure pressure, as was determined by Equation 7.7 where H is the unit step function. In similar fashion to the previous cases, 7.7 was differentiated and plugged into Equation 7.2; however, more details are included as the step function yields a particularly simple result.

$$V(P) = V_f\left(1 - H(P - P_f)\right) \tag{7.7}$$

Differentiating Equation 7.7 with respect to pressure gives Equation 7.8, where δ is the delta function.

$$\frac{dV}{dP}(P) = -V_f \delta(P - P_f) \tag{7.8}$$

Plugging 7.8 into 7.2 and using the fundamental property of the delta function to perform the integration gives Equation 7.9, which provided the attachment time of the step response, t_{fstep}. From this equation, it is seen that no details of the lamellar response were needed, and in fact, only the volume, pressure, and flow rate at failure were required.

$$t_{fstep} = \frac{V_f}{Q(P_f)} \tag{7.9}$$

Additionally, if the failure pressure is large, then the constant term dominates the flow rate model in Equation 7.4, an additional simplification occurs as seen in 7.10.

$$t_{fstep} = \frac{V_f \mu_m W}{\alpha L_p}, \text{ for large } P_f \tag{7.10}$$

At this point, everything needed to perform the integration in Equation 7.2 has been described, and the attachment time can be computed. In all cases, except for the step response, numerical integration was carried out in MATLAB (R2009a, Natick, MA, USA).

7.3 Results and Discussion

The fitting parameters α and β for the surrogate model of flow rate into the pad (Equation 7.4) were found to be 7.659×10^{-9} mL-Pa and 0.02562 1/Pa. These values contain information about both the attachment surface (shark skin) topology and the

material properties of remora tissue. Using the values in Table 7.1, the model provided an excellent fit to the numerical simulation as seen in Figure 7.5. From [26], two competing factors determine the shape of the curve. Low pressures correspond to low flow rates because the driving force (pressure) for fluid motion is low; whereas, at high sub-ambient pressures, compression of the soft fleshy lip against the host surfaces creates a flow restriction that results in diminishing flow rates for higher sub-ambient pressure differentials. It is evident due to the low flow rates that the fleshy lip creates an excellent seal against rough surfaces such as shark skin, which has been attributed to highly compliant tissues at the sealing interface [26]. In the future, it would be useful to empirically relate the coefficients α and β directly to the topological and material properties of the host surface and seal tissue to facilitate efficient calculation of leakage rates and attachment times.

By implementing the flow rate model into Equation 7.2 and performing the integration, attachment time estimates were computed. The results of the three different lamellar responses including the euthanized remora tissue, linear, and step cases are seen in Table 7.3.

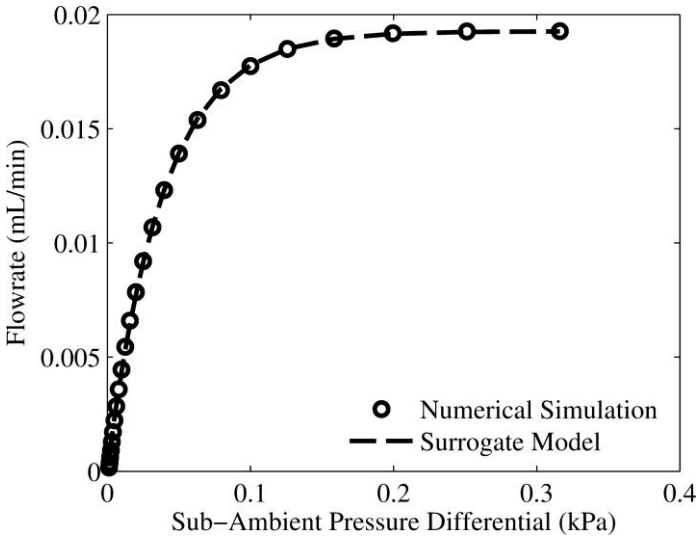

Figure 7.5: Surrogate model and simulation results for the flow rate across the remora's fleshy lip vs. sub-ambient pressure when attached to Mako Shark skin

Table 7.3: Attachment Times with Different Lamellar Responses

Lamellar Response	Attachment Time (min)
Euthanized Remora Tissue	5.62
Linear	5.52
Step	6.90
Step (Large P_f)	5.05

As a basis of comparison, attachment times of remoras (*Echeneis naucrates*) to captive bull sharks (*Carcharhinus leucas*) have been observed in [16]. In the study, attachment times varied from 0.4 to 20.2 minutes with an average on the order of 4 minutes. The remoras in the study were larger (70-80 cm) than the one analyzed here (~40 cm) and attached to a different shark species; however, the average host speed (0.62-0.69 m/s) was similar to that investigated here (0.65 m/s). Despite the differences in remora size and host species, the attachment times estimated in Table 7.3 are certainly comparable to those observed in [16].

The differing attachment times in Table 7.3 illustrate the role lamellae can play in attachment. Among the cases considered, the linear response failed the fastest because it had the largest area under the volume vs. pressure curve in Figure 7.4. Physically, this means the linear case has the lowest "stiffness," or that its resistance to increases in volume with respect to pressure was low. This trend of increasing stiffness and longer attachment times was further borne out by the euthanized remora tissue and step response at low pressure. The step response was the stiffest among the cases, and in fact represented the stiffest possible lamellar response, as there was no volume change until the failure pressure was reached. Therefore, the step response not only resulted in the longest attachment time, but also represented the upper bound for a given failure pressure. Comparing the euthanized remora tissue response to the step response, one could surmise that a live remora may be able to actively extend its attachment time (by 20 percent) by stiffening its lamellae, perhaps by means of muscle contractions, to resist volume changes. It might also be concluded that because prolonged attachment is favorable to remora, those with a naturally stiffer lamellar response have an adhesive advantage.

The attachment times indicate that prolonged remora adhesion on the order of minutes seems likely to occur, but in the wild remora association with a host has been observed to last for weeks [72]. Resolving these two issues suggests that some active maintenance of the suction bond must be carried out either by active pumping or removal of fluid from the pad, which has been suggested by [137, 138], or by periodically reestablishing attachment entirely. This need to provide maintenance may help explain movements of an attached remora over the host's body as observed in [16, 72].

Broadly speaking, the analysis presented here illustrates several important concepts of remora attachment. In light of a historical debate as to whether remora adhesion is primarily suction or friction based [22, 55], the answer is both. Determination of the failure pressure from the drag and frictional forces clearly shows that reduced drag and increased friction results in a lower failure pressure within the dorsal pad from Equation 7.3. In turn, the reduced failure pressure results in an increased volume at failure from Figure 7.4 and reduced flow rates from Figure 7.5. When combined, these yield increased attachment times from Equations 7.9 and 7.10. The same argument can be used to explain why remora readily detach when an anterior directed force is applied [21], as the friction coefficient in the anterior direction is much lower than that in the posterior direction [55]. Similarly, it is important for an attached remora to be aligned with the oncoming flow as this minimizes their drag profile. Thus, although drag and friction are not directly related to the creation of suction itself, they are important factors that contribute to the remora's overall attachment strategy.

The geometry of the pad and its deformation with respect to pressure were also shown to be key factors in remora adhesion. The importance of the lamellar response has already been discussed, but it is also import to consider the total amount of fluid that the dorsal pad can tolerate. Equations 7.9 and 7.10 both show that increasing the fluid volume at failure has a strong impact on the computed attachment time. One challenge to the approach presented is measuring the fluid volume within the pad, especially in the context of the lamellar response, as it can be difficult to acquire due to either its small size, the equipment involved (such as μCT), or the complexity of the lamellar structure itself [27]. One advantage of assuming a lamellar step response is that the details of

deformation are not needed, and only the volume at failure is required. Although this results in an upper bound estimate, it may still be reasonable as seen in Table 7.3. Additionally, two other important geometric properties of the dorsal pad that linearly affected attachment time were the width of the seal, W, and the perimeter of the pad, L_p. Equation 7.10 shows that an increased seal width to perimeter ratio is beneficial for prolonged attachment. However, because measurement of these parameters was carried out on a euthanized specimen, the degree of control a remora can exert over them and the degree to which they are dependent on the remora's size is unknown.

Although the importance of pad mucus has been discussed elsewhere [22, 26], here it is shown to have a strong impact on attachment time as seen in Equations 7.4 and 7.10 where increased viscosity results in reduced leakage rates across the fleshy lip. As a corollary, because temperature can affect viscosity, warmer waters (30°C) could reduce attachment times by 20 percent due to reduced viscosity. As a potential countermeasure to viscosity reduction or as a means to increase attachment time in general, the remora could alter the composition or quantity of its secreted mucus as is observed in distressed fish [34].

Other than shark attachment considered in this investigation, remora have been reported to attach to dolphins for extended periods (~half an hour) at swift swimming speeds (~5 m/s) [139, 140]. Dolphin skin is much smoother than shark skin due to the lack of denticles; though it does possess features which may render it permeable and affect friction [141]. The reduced roughness would result in improved sealing effectiveness according to the flow rate model employed and therefore increased attachment times [26]. This in addition to the other factors discussed such as increased

mucus viscosity, increased seal widths, stiffened lamellae, or increased pad volumes could easily produce attachment times on the order of 10s of minutes corresponding to the observed behavior.

Concerning remora attachment in general, the work presented here should be viewed as one mode of adhesive failure among many. As mentioned previously, other modes of failure may occur before the pad fills with fluid and suction pressure is lost including breaching the fleshy lip, application of large shearing forces greater than spinule friction, or cavitation inside the dorsal pad. Additionally, other forces that act on the remora may become significant such as buoyancy or inertial forces which could increase or decrease attachment time depending on the details of a particular situation. Thus, when taken together, the failure modes provide a profile of the operational limits of remora attachment, which can be used to assess or predict adhesive performance in a particular environment or situation.

As a final note, although the analysis presented is focused specifically on the remora, the first-principles, bottom-up approach presented here could be applied to similar attachment strategies in other organisms. For example in many other species including lumpsuckers (family Cyclopteridae) [39, 40], river loaches (family Balitoridae) [41] and clingfish (family Gobiesocidae) [37, 51] prolonged suction based attachment is favorable, and similar difficulties must be overcome including sealing against challenging surfaces and resisting drag forces by friction or other means. In such cases, the challenge becomes acquiring the requisite topological, material, and geometric properties of the tissues, structures, and fluids necessary to perform the analyses. Thus,

many of the mechanisms available to the remora explored here may also be important to suction based attachment strategies in other species as well.

7.4 Conclusion

In this chapter, the suction-based attachment strategy of the remora fish was explored. Because prolonged attachment is favorable to the remora, an attachment analysis focused on gradual failure mechanisms to which remoras are regularly exposed was employed rather than one based on randomly encountered, large, disruptive forces. Failure was assumed to occur due to slow leakage of fluid into the remora's pad that resulted in reduced suction pressures, and an inability to resist drag forces by means of friction. The sequence ultimately ends with the remora slipping or being sheared from its host. The analysis implemented required a nuanced approach involving many aspects of remora and host structures including the sealing effectiveness of the fleshy lip against a rough host topology, the lamellar response to pressure changes, the friction enhancement due to spinules, and the hydrodynamic drag on the remora's streamlined body. The attachment times predicted by the analysis compared favorably to observed attachment times of live remora in similar conditions. Thus, critical aspects of remora morphology and physiology were identified and their roles in attachment were quantified. Several concepts shown to benefit prolonged attachment times included: a stiff lamellar response with respect to fluid volume and pressure changes, a large seal width to perimeter ratio, increased mucus viscosity, a lower drag profile, increased spinule friction, and improved sealing effectiveness. Additionally, because the methods employed were based on a first principles, bottom up approach, not only could the methodology be applied to predict

remora attachment under different circumstances, but potentially to similar suction based attachment strategies in other organisms.

CHAPTER 8

Concluding Remarks

The primary research question stated in CHAPTER 1 was how do functional structures of the remora suction disk work in concert with active remora behavior to achieve strong, reversible attachment to a variety of host substrates and what are the limits of remora attachment?

In CHAPTER 2, the fluid drag on an attached remora, which is the primary force that must be overcome, was quantified. A remora model was built from μCT scans, optical images, and direct measurement. The model was subjected to virtual fluid flows using finite element methods, and scaling relationships between different remora features such as the head-to-tail length, volume, wetted surface area, etc. were developed. It was found that drag forces on a remora can be reasonably estimated as those of streamlined body with an equivalent fineness ratio, and that the streamlined shape of the remora is optimized for host attachment rather than free swimming. Furthermore, subjecting the remora model to different boundary layer thicknesses that occur at different attachment locations on a host showed that there is minimal hydrodynamic benefit (reduced drag) to the remora with respect to skin friction, which indicates there are likely alternate reasons for attachment site discrimination that has been observed in remora. Additionally, by comparing the drag to frictional forces developed on the remora along with the scaling estimates, it was found that not only is it unlikely for any remora to be dislodged by elevated host swimming speeds (which is observed in the wild), but larger remora are more likely to remain attached to a host than a smaller remora under the same conditions.

CHAPTER 3 presented a quantitative exploration of the mineralized tissue structures within the dorsal pad. Specifically, high resolution μCT scans of euthanized remora specimens were obtained and segmented using image analysis to isolate the lamellar structures. Algorithms were developed to objectively analyze the three-dimensional virtual images which included identification and count of all spinule tip locations and three-dimensional paths (of which there were thousands); statistical nearest neighbor analysis and comparison between spinule tip and shark denticle location data; and demonstration of geometric similarities among remora pads through normalization of structural descriptors. The similarities between the length scales of spinule tip separation and dermal denticle separation suggested an interaction between the two features, which inspired the exploration of spinule friction in the subsequent chapter of which the analysis of spinule location data played a crucial role.

CHAPTER 4 was an investigation of spinules and their ability to enhance friction on rough surfaces. As alluded to in previous chapters, friction is important to the remora for resisting drag forces and spinules are curiously separated by similar distances as features (denticles) on surfaces with which they regularly interact (shark skin). By observing μCT images, it was found that even though the spinules within a lamella may be of different lengths, they tend to terminate in roughly the same plane. Using the plane as a frame of reference, the spinules were treated as thousands of individual styli, which trace the host surface in a manner similar to that described by the established "ratcheting" friction mechanism. A simplified, periodic host surface (shark skin) was created from its measured frequency and amplitude components, and the expected value of the frictional force required to overcome static friction was estimated. The analysis demonstrated the

importance of roughness length scales on the host surface, namely that friction enhancement occurs when spinules can enter the surface valleys between features rather than aliasing the peaks and, in a sense, interlock with the host surface. The results show that spinule tip shape can strongly influence friction (sharper tips equal enhanced friction) especially at lower spatial wavelengths. Furthermore, because the spinules themselves are not well described by a single geometric parameter, the friction characteristics of the individual spinules were used to show that friction enhancement (and therefore tip shape) is independent of location within a lamella. The ratcheting friction model and methods used were validated using artificial glass spinules on glass surfaces with differing roughness profiles.

CHAPTER 5 outlined a two-dimensional treatment of the remora lamellar compartments. Remora morphology was captured using high and low resolution μCT scans, and image segmentation was performed to segregate mineralized and soft tissues. The high resolution scans of an individual lamella were overlaid with lower resolution scans of the entire pad to obtain an accurate representation of the tissue locations within a lamella and the lamella orientation within the pad. To facilitate a finite element description of the geometry, algorithms were developed to fit smooth Bezier curves to the segmented data. The key results of the chapter included: development of a structural finite element model based on observed lamellar geometry and measured material properties, quantification of the fluid-volume reduction capabilities of the remora pad, and estimation of the restorative force and complex stiffness generated by the lamellar compartments in the remora during attachment. The change in pad fluid volume with

respect to loading conditions was especially important to later chapters for estimating the time scale of remora attachment.

In CHAPTER 6 a model of the leakage rate across the fleshly lip and its interfacial permeability with respect to sub-ambient pressures within the dorsal pad was presented. The theoretical model was developed using principles from asymptotic/homogenization analysis, and the fluid/structure interaction problem of remora skin in contact with a rough surface (shark skin) was solved for specific cases. Although formulated with the remora in mind, the methodology is general enough to be applicable to other sealing structures as was demonstrated by validation of the model using an experimental suction apparatus. The key results included characterization of remora fleshy lip tissue with dynamic mechanical analysis, characterization of a shark denticle surface using confocal microscopy, and solution of the flow rate model over many different surface roughness values. Because the model was developed using a bottom-up, first-principles approach, the important geometric, mechanical, and rheological parameters relevant to sealing effectiveness were identified. It was found that cutaneous mucus layers secreted by the mucus can play a significant role improving sealing effectiveness, but are not likely to compensate for large increases in surface roughness. Nevertheless, it was found that very low flow rates (10^{-3} mL/min) are developed across the fleshy lip seal on rough surfaces that remora are likely to encounter such as shark skin. Such low flow rates were attributed to the fleshy lip's low stiffness, and its ability to conform to the host contact surface.

Finally, CHAPTER 7 brought together the results of all the previous chapters to assess the attachment performance and limits of a remora fish. Although there are

potentially many ways to characterize the limits of remora attachment, one metric that is readily observable and demonstrates how all the presented functional features work in concert to create adhesion is the time of attachment, or equivalently the time to attachment failure. The failure analysis presented in CHAPTER 7 assumed that gradual failure of adhesion takes place. A remora can tolerate only so much fluid (CHAPTER 3 and CHAPTER 5) leakage across its fleshy lip into its pad (CHAPTER 6) before a critical pressure is reached such that friction (CHAPTER 4) is no longer sufficient to resist the drag forces (CHAPTER 2) imposed by host locomotion. The computed attachment times (on the order of minutes to tens of minutes) were found to be in good agreement with those observed in live remora, which not only strengthens the arguments and biological implications discussed in the final chapter, but all proceeding chapters as well. Additionally, with respect to remora ecology, the model quantified how active stiffening of the remora's lamella translated into increased attachment times, and helps explain the remora's ability to better resist posterior vs. anterior directed forces. Furthermore, the attachment times computed illustrate that active maintenance of the remora's seal must be periodically carried out in order to explain their prolonged association with hosts (weeks).

Beyond remoras, there are many other examples of suction based attachment in the animal kingdom, which may be more or less nuanced. Though ultimately, any suction based attachment strategy will encounter similar challenges to those presented to remoras whether it is a similar species or a suction cup in a shower. The ability to create, regulate, and maintain a robust seal is essential to sustaining suction pressures and attachment forces. Understanding the role of friction, which is the response to suction forces, at the

interface between two functional surfaces (e.g. remora and host) is imperative to resist dislodging forces whether they be from fluid drag, impact, inertia or otherwise. As such, many of the tools and techniques developed in this thesis were created with the intent to be applicable to other biological and engineering systems, especially in the translation of biological principles to engineering design. Therefore, to those who have made it this far, it is the sincere hope of the author that the lessons learned from the remora not only serve to inspire you to create new knowledge and new devices, but that the tools developed herein aid you along the way.

REFERENCES

1. D. Fertl and A. Landry, *Remoras*, in *Encyclopedia of Marine Mammals*. 2002.

2. Fertl, D. and A.M. Landry, *Sharksucker (Echeneis naucrates) on a Bottlenose Dolphin (Tursiops truncatus) and a Review of other Cetacean-Remora Associations.* Marine Mammal Science, 1999. **15**(3): p. 859-863.

3. Chen, P.Y., J. McKittrick, and M.A. Meyers, *Biological materials: Functional adaptations and bioinspired designs.* Progress in Materials Science, 2012. **57**(8): p. 1492-1704.

4. Gudger, E.W., *On the use of the sucking-fish for catching fish and turtles studies in Echeneis or Remora, II.* American Naturalist, 1919. **53**: p. 289-311.

5. Sola, C.R.d., *Observations on the Use of the Sucking-Fish or Remora, Echeneis naucrates, for Catching Turtles in Cuban and Colombian Waters.* Copeia, 1932. **1932**(2): p. 45-52.

6. O'Toole, B., *Phylogeny of the species of the superfamily Echeneoidea (Perciformes: Carangoidei: Echeneidae, Rachycentridae, and Coryphaenidae), with an interpretation of echeneid hitchhiking behaviour.* Canadian Journal of Zoology, 2002. **80**(4): p. 596.

7. Cressey, R.F. and E.A. Lachner, *The Parasitic Copepod Diet and Life History of Diskfishes (Echeneidae).* Copeia, 1970. **1970**(2): p. 310-318.

8. Ritter, E.K., *Analysis of sharksucker, Echeneis naucrates, induced behavior patterns in the blacktip shark, Carcharhinus limbatus.* Environmental Biology of Fishes, 2002. **65**(1): p. 111-115.

9. Ritter, E.K. and J.M. Brunnschweiler, *Do Sharksuckers, Echeneis naucrates, Induce Jump Behaviour in Blacktip Sharks, Carcharhinus limbatus?* Marine and Freshwater Behaviour and Physiology, 2003. **36**(2): p. 111-113.

10. Williams Jr, E.H., et al., *Echeneid–sirenian associations, with information on sharksucker diet.* Journal of Fish Biology, 2003. **63**(5): p. 1176-1183.

11. Sazima, I. and A. Grossman, *Turtle riders: remoras on marine turtles in Southwest Atlantic.* Neotropical Ichthyology, 2006. **4**(1): p. 123-126.

12. Weihs, D., F.E. Fish, and A.J. Nicastro, *Mechanics of remora removal by dolphin spinning.* Marine Mammal Science, 2007. **23**(3): p. 707-714.

13. Strasburg, D.W., *Some Aspects of the Feeding Behavior of Remora remora.* Pacific Science, 1962. **16**(2): p. 202-206.

14. Strasburg, D.W., *Notes on the Diet and Correlating Structures of Some Central Pacific Echeneid Fishes.* Copeia, 1959. **1959**(3): p. 244-248.

15. Silva-Jr, J.M. and I. Sazima, *Whalesuckers on spinner dolphins: an underwater view*. Marine Biodiversity Records, 2008. **1**: p. 1-5.

16. Brunnschweiler, J.M., *Sharksucker-shark interaction in two carcharhinid species.* Marine Ecology-an Evolutionary Perspective, 2006. **27**(1): p. 89-94.

17. Aughtry, R.H., *A Note on Mass Mortality of the Myctophid Fish Tarletonbeania crenularis.* Copeia, 1953. **1953**(3): p. 190-192.

18. Schwartz, F.J., *Effects of the sharksucker, Echeneis naucrates, disk on scaled and scaleless fish and sea turtles.* ASB Bull., 1977. **24**(84).

19. Schwartz, F.J., *Effects of the Sharksucker, Echeneis Naucrates, Family Echeneididae, on Captive Sheepshead, Archosargus probatocephalus.* Journal of the Elisha Mitchell Scientific Society, 1992. **108**(1): p. 55-56.

20. Britz, R. and G.D. Johnson, *Ontogeny and Homology of the Skeletal Elements that form the Sucking Disc of Remoras (Teleostei, Echeneoidei, Echeneidae).* Journal of Morphology, 2012. **273**(12).

21. Nadler, J.H., et al. *Structures and Function of Remora Adhesion*. in *MRS Spring Meeting 2013*. 2013. San Fransisco, CA.

22. Sewell, R.B.S., *The Adhesive Apparatus of the " Sucking-fish "*. Nature, 1925. **115**: p. 48-49.

23. Fulcher, B.A. and P.J. Motta, *Suction disk performance of echeneid fishes.* Canadian Journal of Zoology-Revue Canadienne De Zoologie, 2006. **84**(1): p. 42-50.

24. Hester, F.J., J.R. Hunter, and R.R. Whitney, *Jumping and Spinning Behavior in the Spinner Porpoise.* Journal of Mammalogy, 1963. **44**(4): p. 586-588.

25. Fish, F.E., A.J. Nicastro, and D. Weihs, *Dynamics of the aerial maneuvers of spinner dolphins.* Journal of Experimental Biology, 2006. **209**(4): p. 590-598.

26. Culler, M., K.A. Ledford, and J.H. Nadler. *The Role of Topology and Tissue Mechanics in Remora Attachment*. in *MRS Fall Meeting 2013*. 2013. Boston, MA.

27. Culler, M. and J.H. Nadler. *Composite Structural Mechanics of Dorsal Lamella in Remora Fish*. in *MRS Fall Meeting 2013*. 2013. Boston, MA.

28. Barnes, W.J.P., *Functional Morphology and Design Constraints of Smooth Adhesive Pads.* MRS Bulletin, 2007. **32**(06): p. 479-485.

29. Autumn, K., et al., *Evidence for van der Waals adhesion in gecko setae.* Proceedings of the National Academy of Sciences, 2002. **99**(19): p. 12252-12256.

30. Huber, G., et al., *Evidence for capillarity contributions to gecko adhesion from single spatula nanomechanical measurements.* Proceedings of the National Academy of Sciences of the United States of America, 2005. **102**(45): p. 16293-16296.

31. Lin, A.Y.M., et al., *Underwater adhesion of abalone: The role of van der Waals and capillary forces.* Acta Materialia, 2009. **57**(14): p. 4178-4185.

32. Kim, T.W. and B. Bhushan, *The adhesion model considering capillarity for gecko attachment system.* Journal of The Royal Society Interface, 2008. **5**(20): p. 319-327.

33. Byern, J.v. and I. Grunwald, *Biological Adhesive Systems*. 2010, New York: Springer Science.

34. Shephard, K.L., *Functions for Fish Mucus.* Reviews in Fish Biology and Fisheries, 1994. **4**(4): p. 401-429.

35. Federle, W., et al., *Wet but not slippery: boundary friction in tree frog adhesive toe pads.* Journal of The Royal Society Interface, 2006. **3**(10): p. 689-697.

36. Barnes, W.J.P., et al., *Elastic modulus of tree frog adhesive toe pads.* Journal of Comparative Physiology a-Neuroethology Sensory Neural and Behavioral Physiology, 2011. **197**(10): p. 969-978.

37. Wainwright, D.K., et al., *Stick tight: suction adhesion on irregular surfaces in the northern clingfish.* Biology Letters, 2013. **9**(3).

38. Davenport, J., *Synopsis of Biological Data on the Lumpsucker*. 1985, Rome: Food and Agriculture Organization of the United Nations.

39. Davenport, J. and V. Thorsteinsson, *Sucker Action in the Lumpsucker Cyclopterus-Lumpus L.* Sarsia, 1990. **75**(1): p. 33-42.

40. Gibson, R.N., *Powers of adhesion in Liparis montagui (Donovan) and other shore fish.* Journal of Experimental Marine Biology and Ecology, 1969. **3**(2): p. 179-190.

41. De Meyer, J. and T. Geerinckx, *Using the Whole Body as a Sucker: Combining Respiration and Feeding with an Attached Lifestyle in Hill Stream Loaches (Balitoridae, Cypriniformes).* Journal of Morphology, 2014. **275**(9): p. 1066-1079.

42. Kier, W.M. and A.M. Smith, *The structure and adhesive mechanism of octopus suckers.* Integrative and Comparative Biology, 2002. **42**(6): p. 1146-1153.

43. Smith, A.M., *Negative-Pressure Generated by Octopus Suckers - A Study of the Tensile-Strength of Water in Nature.* Journal of Experimental Biology, 1991. **157**: p. 257-271.

44. Berglin, M. and P. Gatenholm, *The barnacle adhesive plaque: morphological and chemical differences as a response to substrate properties.* Colloids and Surfaces B: Biointerfaces, 2003. **28**(2–3): p. 107-117.

45. Kamino, K., *Underwater Adhesive of Marine Organisms as the Vital Link Between Biological Science and Material Science.* Marine Biotechnology, 2008. **10**(2): p. 111-121.

46. Waite, J.H., *Nature's underwater adhesive specialist.* International Journal of Adhesion and Adhesives, 1987. **7**(1): p. 9-14.

47. Lee, B.P., et al., *Mussel-Inspired Adhesives and Coatings*, in *Annual Review of Materials Research, Vol 41*, D.R. Clarke and P. Fratzl, Editors. 2011, Annual Reviews: Palo Alto. p. 99-132.

48. Flammang, P., et al., *A study of the temporary adhesion of the podia in the sea star Asterias rubens (Echinodermata, Asteroidea) through their footprints.* Journal of Experimental Biology, 1998. **201**(16): p. 2383-2395.

49. Huber, G., et al., *Resolving the nanoscale adhesion of individual gecko spatulae by atomic force microscopy.* Biology Letters, 2005. **1**(1): p. 2-4.

50. Spolenak, R., et al., *Effects of contact shape on the scaling of biological attachments.* Proceedings of the Royal Society A: Mathematical, Physical and Engineering Science, 2005. **461**(2054): p. 305-319.

51. Ditsche, P., D.K. Wainwright, and A.P. Summers, *Attachment to challenging substrates – fouling, roughness and limits of adhesion in the northern clingfish (Gobiesox maeandricus).* The Journal of Experimental Biology, 2014. **217**(14): p. 2548-2554.

52. Green, D.M. and D.L. Barber, *The ventral adhesive disc of the clingfish Gobiesox maeandricus: integumental structure and adhesive mechanisms.* Canadian Journal of Zoology, 1988. **66**(7): p. 1610-1619.

53. Smith, A.M., *Cephalopod sucker design and the physical limits to negative pressure.* Journal of Experimental Biology, 1996. **199**(4): p. 949-958.

54. Tramacere, F., et al. *Artificial adhesion mechanisms inspired by octopus suckers*. in *Robotics and Automation (ICRA), 2012 IEEE International Conference on*. 2012.

55. Hora, S.L., *The Adhesive Apparatus of the "Sucking-fish."*. Nature, 1923. **111**: p. 668-668.

56. Fung, Y.C., et al., *Introduction to Bioengineering*, ed. T.C. Fung. Vol. 1. 2001, Hackensack, NJ: World Scientific.

57. Fung, Y.C., *Biomechanics Mechanical Properties of Living Tissues*. 1993: Springer-Verlag New York Inc.

58. Vincent, J., *Structural Biomaterials*. 2012, Prinston, NJ: Prinston University Press.

59. Cowin, S.C. and S.B. Doty, *Tissue Mechanics*. 2007: Springer Science.

60. Lakes, R.S., *Viscoelastic Solids*. 1999, Boca Raton, FL: CRC Press.

61. Krouskop, T.A., et al., *Elastic moduli of breast and prostate tissues under compression.* Ultrasonic Imaging, 1998. **20**(4): p. 260-274.

62. Fung, Y.C., *Structure and Stress-Strain Relationship of Soft-Tissues.* American Zoologist, 1984. **24**(1): p. 13-22.

63. DeWall, R.J., et al., *Characterizing the compression-dependent viscoelastic properties of human hepatic pathologies using dynamic compression testing.* Physics in Medicine and Biology, 2012. **57**(8): p. 2273-2286.

64. Liu, Z. and L. Bilston, *On the viscoelastic character of liver tissue: experiments and modelling of the linear behaviour.* Biorheology, 2000. **37**(3): p. 191-201.

65. Kiss, M.Z., T. Varghese, and T.J. Hall, *Viscoelastic characterization of in vitro canine tissue.* Physics in Medicine and Biology, 2004. **49**(18): p. 4207-4218.

66. Gibson, L. and M. Ashby, *Cellular Solids*. 1997, United Kingdom: Cambridge University Press.

67. Horton, J.M. and A.P. Summers, *The material properties of acellular bone in a teleost fish.* Journal of Experimental Biology, 2009. **212**(9): p. 1413-1420.

68. Cohen, L., et al., *Comparison of structural, architectural and mechanical aspects of cellular and acellular bone in two teleost fish.* Journal of Experimental Biology, 2012. **215**(11): p. 1983-1993.

69. Dean, M.N. and R. Shahar, *The structure-mechanics relationship and the response to load of the acellular bone of neoteleost fish: a review*. Journal of Applied Ichthyology, 2012. **28**(3): p. 320-329.

70. Daniel, T.L., *Fish Mucus - Insitu Measurements of Polymer Drag Reduction.* Biological Bulletin, 1981. **160**(3): p. 376-382.

71. Gona, O., *Mucous glycoproteins of teleostean fish: a comparative histochemical study.* The Histochemical Journal, 1979. **11**(6): p. 709-718.

72. Silva-Jr, J.M. and I. Sazima, *Whalesuckers and a Spinner Dolphin Bonded for Weeks: Does Host Fidelity Pay Off?* Biota Neotropica, 2003. **3**(2): p. 1-5.

73. Lang, T.G. and D.A. Daybell, *Porpoise performance tests in a seawater tank*. 1963, U.S. Naval Ordnance Test Station. p. 1-50.

74. Lang, T.G. and K. Pryor, *Hydrodynamic Performance of Porpoises (Stenella attenuata).* Science, 1966. **152**(3721): p. 531-533.

75. Purves, P.E., W.H.D.v. Heel, and A. Jonk, *Locomotion in Dolphins Part I: Hydrodynamic experiments on a model of the bottle-nosed dolphin, Tursiops truncatus.* Aquatic Mammals, 1975. **3**: p. 5-31.

76. Ogilvy, C.S. and A.B. Dubois, *The Hydrodynamic Drag of Swimming Bluefish (Pomatomus Saltatrix) in Different Intensities of Turbulence - Variation Changes of Buoyancy.* Journal of Experimental Biology, 1981. **92**(JUN): p. 67-85.

77. Webb, P.W., *Hydrodynmaics and Energetics of Fish Propulsion*, in *Bulletin of the Fisheries Research Board of Canada*. 1975.

78. Miller, P.J.O., et al., *Swimming gaits, passive drag and buoyancy of diving sperm whales Physeter macrocephalus.* Journal of Experimental Biology, 2004. **207**(11): p. 1953-1967.

79. Fish, F.E., *Power Output and Propulsive Efficiency of Swimming Bottle-Nosed Dolphins (Tursiops-Truncatus).* Journal of Experimental Biology, 1993. **185**: p. 179-193.

80. Anderson, E.J., W.R. McGillis, and M.A. Grosenbaugh, *The boundary layer of swimming fish.* Journal of Experimental Biology, 2001. **204**(1): p. 81-102.

81. Munson, B., D.F. Young, and T.H. Okiishi, *Fundementals of Fluid Mechanics*. 5th ed. 2006, Hoboken, NJ: John Wiley & Sons Inc.

82. Rosset, A., L. Spadola, and O. Ratib, *OsiriX: An Open-Source Software for Navigating in Multidimensional DICOM Images.* Journal of Digital Imaging, 2004. **17**: p. 205-216.

83. Hoerner, S.F., *Fluid-Dynamic Drag*. 1965: published by the author.

84. Peter Klimley, A., et al., *Movements and Swimming Behavior of Three Species of Sharks in La Jolla Canyon, California.* Environmental Biology of Fishes, 2002. **63**(2): p. 117-135.

85. Weng, K.C., et al., *Migration and habitat of white sharks (Carcharodon carcharias) in the eastern Pacific Ocean.* Marine Biology, 2007. **152**(4): p. 877-894.

86. Hueter, R.E., J.P. Tyminski, and R. de la Parra, *Horizontal Movements, Migration Patterns, and Population Structure of Whale Sharks in the Gulf of Mexico and Northwestern Caribbean Sea.* Plos One, 2013. **8**(8).

87. Carlson, J.K., et al., *Habitat use and movement patterns of bull sharks Carcharhinus leucas determined using pop-up satellite archival tags.* Journal of Fish Biology, 2010. **77**(3): p. 661-675.

88. Brunnschweiler, J.M., *Water-escape velocities in jumping blacktip sharks.* Journal of the Royal Society Interface, 2005. **2**(4): p. 389-391.

89. Webb, P.W. and R.S. Keyes, *Swimming Kinematics of Sharks.* Fishery Bulletin, 1982. **80**(4): p. 803-812.

90. Blevins, R.D., *Applied Fluid Dynamics Handbook*. 1984, New York, NY: Van Nostrand Reinhold Company Inc.

91. Pohlhausen, K., *The approxiamte integration of the differential equation of laminar boundary layer.* Journal of Applied Mathematics and Mechanics, 1921. **1**: p. 252-268.

92. von Karman, T., *On laminar and turbulent friction.* Journal of Applied Mathematics and Mechanics, 1921. **1**: p. 233-252.

93. Pabst, D.A., *Intramuscular Morphology and Tendon Geometry of the Epaxial Swimming Muscles of Dolphins.* Journal of Zoology, 1993. **230**: p. 159-176.

94. Pabst, D.A., *Axial muscles and connective tissues of the bottlenose dolphin*, in *The bottlenose dolphin*, S. Leatherwood and R.R. Reeves, Editors. 1990, Academic Press: San Diego & London. p. 51-67.

95. Fish, F.E., et al., *Measurement of hydrodynamic force generation by swimming dolphins using bubble DPIV*. Journal of Experimental Biology, 2014. **217**(2): p. 252-260.

96. Rosa, R., et al., *Bioenergetics of small pelagic fishes in upwelling systems: relationship between fish condition, coastal ecosystem dynamics and fisheries.* Marine Ecology Progress Series, 2010. **410**: p. 205-218.

97. Sazima, I., *Species records, mistaken identifications, and their further use: the case of the diskfish Echeneis naucrates on a spinner dolphin.* Neotropical Ichthyology, 2006. **4**: p. 457-460.

98. Vogel, S., *Life in Moving Fluids*. 2nd ed. 1994, Princeton, NJ: Princeton University Press.

99. Storms, R., *The adhesive disk of Echeneis*, in *The Annals and Magazine of Natural History*. 1888. p. 67-76.

100. Grudger, E., *A Study of the Smallest Shark-suckers (Echeneididae) on Record: With Special Reference to Metamorphosis*. 1926, The American Musem of Natural History New York City: New York, NY.

101. Fraser, G.J., R.F. Bloomquist, and J.T. Streelman, *A periodic pattern generator for dental diversity.* Bmc Biology, 2008. **6**.

102. Richman, J.M. and G.R. Handrigan, *Reptilian Tooth Development.* Genesis, 2011. **49**(4): p. 247-260.

103. Schindelin, J., et al., *Fiji: an open-source platform for biological-image analysis.* Nature Methods, 2012. **9**(7): p. 676-682.

104. McLachlan, G. and D. Peel, *General Introduction Finite Mixture Models*. 2005: John Wiley & Sons, Inc.

105. Fulcher, B.A. and P.J. Motta, *Suction disk performance of echeneid fishes.* Canadian Journal of Zoology, 2006. **84**(1): p. 42-50.

106. Maie, T., H.L. Schoenfuss, and R.W. Blob, *Performance and scaling of a novel locomotor structure: adhesive capacity of climbing gobiid fishes.* Journal of Experimental Biology, 2012. **215**(22): p. 3925-3936.

107. Muir, B.S. and R.M. Buckley, *Gill Ventilation in Remora Remora.* Copeia, 1967. **1967**(3): p. 581-586.

108. Stote, A., C.P. Kenaley, and B.E. Flammang, *A morphological analysis of the suction-disc performance and interspecific host association in the remoras (Percomorpha: Carangiformes: Echeneidae).* Integrative and Comparative Biology, 2014. **54**: p. E355-E355.

109. Persson, B.N.J., et al., *On the nature of surface roughness with application to contact mechanics, sealing, rubber friction and adhesion.* Journal of Physics-Condensed Matter, 2005. **17**(1): p. R1-R62.

110. Vorburger, T.V., *Methods for Characterizing Surface Topology*. Tutorials in Optics: Osa Annual Meeting, Rochester NY, ed. D.T. Moore. 1992, Washington DC: Optical Society of America.

111. Bowden, F.P. and D. Tabor, *The Friction and Lubrication of Solids Part I*. 1950, London: Oxford University Press.

112. Bhushan, B., *Introduction to Tribology*. 2002, New York: John Wiley & Sons.

113. Bhushan, B. and J.A. Ruan, *Atomic-Scale Friction Measurements Using Friction Force Microscopy: Part II - Application to Magnetic Media.* Journal of Tribology-Transactions of the Asme, 1994. **116**(2): p. 389-396.

114. Makinson, K.R., *On the cause of the frictional difference of the wool fibre.* Transactions of the Faraday Society, 1948. **44**(0): p. 279-282.

115. ASTM, *Standard Test Method for Static and Kinetic Coefficients of Friction of Plastic Film and Sheeting*. 2014, ASTM International: West Conshohocken, PA.

116. Motta, P., et al., *Scale morphology and flexibility in the shortfin mako Isurus oxyrinchus and the blacktip shark Carcharhinus limbatus.* Journal of Morphology, 2012. **273**(10): p. 1096-1110.

117. Huang, L.K. and M.J.J. Wang, *Image Thresholding by Minimizing the Measures of Fuzziness.* Pattern Recognition, 1995. **28**(1): p. 41-51.

118. Czernik, D.E., *Internal Combustion Engine Gaskets*, in *Gaskets and Gasketed Joints*, J.H. Bickford, Editor. 1997, Marcel Dekker, Inc.: New York, NY.

119. Fisher, E.W., *Packing and Seals*, in *Marks' Standard Handbook for Mechanical Engineers*, E.A. Avallone and T.B. III, Editors. 1987, McGraw-Hill Inc.: New York, NY.

120. Persson, B.N.J. and C. Yang, *Theory of the leak-rate of seals.* Journal of Physics-Condensed Matter, 2008. **20**(31).

121. Persson, B.N.J., et al., *Contact area between a viscoelastic solid and a hard, randomly rough, substrate.* The Journal of Chemical Physics, 2004. **120**(18): p. 8779-8793.

122. Guarnieri, F.A. and A. Cardona, *3D Solid Incompressible Viscoelastic Finite Element in Large Strains for the Cornea.* Mechanica Computacional, 1997. **18**: p. 799-808.

123. Haghpanahi, M. and H.A. Naeeni. *Investigation of Viscoelastic Properties of Human Liver Tissue Using MR Elastography and FE Modeling*. in *Proceedings of the 17th Iranian Conference of Biomedical Engineering*. 2010.

124. Chatelin, S., et al., *In vivo liver tissue mechanical properties by transient elastography: Comparison with dynamic mechanical analysis.* Biorheology, 2011. **48**(2): p. 75-88.

125. Biot, M.A., *General theory of three-dimensional consolidation.* Journal of Applied Physics, 1941. **12**(2): p. 155-164.

126. Mei, C.C. and B. Vernescu, *Homogenization Methods for Multiscale Mechanics*. 2010, 27 Warren St, Suite 401-402, Hackensack, NJ 07601: World Scientific Publishing Co.Pte.Ltd.

127. Dullen, F.A.L., *Porous Media Fluid Transport and Pore Structure*. 2nd ed. 1992, Sandiago, CA: Academic Press Inc.

128. Hallquist, J.O., G.L. Goudreau, and D.J. Benson, *Sliding interfaces with contact-impact in large-scale Lagrangian computations.* Computer Methods in Applied Mechanics and Engineering, 1985. **51**(1–3): p. 107-137.

129. Belytschko, T., W.K. Liu, and B. Moran, *Nonlinear Finite Elements for Continua and Structures*. 2000: Wiley.

130. Hyun, S., et al., *Finite-element analysis of contact between elastic self-affine surfaces.* Physical Review E, 2004. **70**(2).

131. ASTM, *Standard Practice for Stress Relaxation Testing of Raw Rubber, Unvulcanized Rubber Compounds, and Thermoplastic Elastomers*. 2012, ASTM International: West Conshohocken, PA.

132. Moss, M.L., S.J. Jones, and K.A. Piez, *Calcified Ectodermal Collagens of Shark Tooth Enamel and Teleost Scale.* Science, 1964. **145**(3635): p. 940-942.

133. Chen, P.Y., et al., *Structure and mechanical properties of selected biological materials.* Journal of the Mechanical Behavior of Biomedical Materials, 2008. **1**(3): p. 208-226.

134. Enax, J., et al., *Structure, composition, and mechanical properties of shark teeth.* Journal of Structural Biology, 2012. **178**(3): p. 290-299.

135. Mix, A.W. and A.J. Giacomin, *Standardized Polymer Durometry.* Journal of Testing and Evaluation, 2011. **39**(4): p. 696-705.

136. Roberts, S.D. and M.D. Powell, *The viscosity and glycoprotein biochemistry of salmonid mucus varies with species, salinity and the presence of amoebic gill disease (vol 175, pg 1, 2004).* Journal of Comparative Physiology B-Biochemical Systemic and Environmental Physiology, 2005. **175**(3): p. 219-219.

137. Bonnell, B., *Structure and Action of the Sucker of Echeneis.* Nature, 1961. **191**(4786): p. 403-403.

138. Bonnell, B., *Adhesive Disk of Echeneis naucrates.* Nature, 1964. **203**(494): p. 206-&.

139. Shane, S., *Suckerfish Attached to a Bottlenose Dolphin in Texas.* Journal of Mammalogy, 1978. **59**(2): p. 439-440.

140. Mahnken, T. and R.M. Gilmore, *Suckerfish on Porpoise.* Journal of Mammalogy, 1960. **41**(1): p. 134.

141. Pavlov, V.V., *Dolphin skin as a natural anisotropic compliant wall.* Bioinspiration & Biomimetics, 2006. **1**(2): p. 31-40.